Initial Orbit Determination with Angles-Only Observations of Space Debris

Inauguraldissertation
der Philosophisch-naturwissenschaftlichen Fakultät
der Universität Bern

vorgelegt von

Harleen Kaur Mann

aus Indien

Leiter der Arbeit:
Prof. Dr. T. Schildknecht
Astronomisches Institut der Universität Bern

Ko-Leiter der Arbeit:
Dr. A. Vananti
Astronomisches Institut der Universität Bern

Initial Orbit Determination with Angles-Only Observations of Space Debris

Inauguraldissertation
der Philosophisch-naturwissenschaftlichen Fakultät
der Universität Bern

vorgelegt von

Harleen Kaur Mann

aus Indien

Leiter der Arbeit:
Prof. Dr. T. Schildknecht
Astronomisches Institut der Universität Bern

Ko-Leiter der Arbeit:
Dr. A. Vananti
Astronomisches Institut der Universität Bern

Von der Philosophisch-naturwissenschaftlichen Fakültat angenomen.

Bern, 18 June 2025   Der Dekan:

Prof. Dr. Jean-Louis Reymond

Abstract

The initial orbit determination of a space object is one of the most fascinating problems to solve for a space debris scientist which is essential for catalogue build-up. Typically, more than one series of observations is used, as a single series of observations is not sufficient to achieve the required precision. The challenge is to find which tracklets belong to the same object and hence, together form a large pool of observations. It also becomes more demanding when relying solely on optical measurements to solve this problem, which is the case for space objects in higher altitudes due to a lack of measurements from any other source.

The existing methods for tracklet correlation and initial orbit determination don't include the effect of perturbations on the orbit. The main contribution of this work is a perturbed initial orbit determination method which facilitates the association of two series of optical observations. Since the proposed algorithm is mainly for the geostationary orbital region, the perturbations only due to geopotential terms, third body forces of the Sun, Moon, and solar radiation pressure are considered. The algorithm takes inspiration from the existing optimized boundary value initial orbit determination method (OBVIOD) which uses Mahalanobis distance as the loss function. An initial hypothesis is made using the optical measurements from two series of observations and a pair of ranges. A shooting technique is used where the initial orbital state is computed by propagating from the epoch of the first tracklet to the epoch of the second. The proposed mechanism uses a numerical propagator to add the effect of perturbations. Furthermore, the robustness and accuracy of two different root-finding techniques is analysed for use in the Shooting method.

The proposed algorithm is tested using simulated observations which belong to objects of varying area-to-mass ratios and are separated by multiple revolutions. The proposed technqiue is able to successfully correlate various pairs of tracklets even if they belong to objects in highly perturbed orbits and performs much better than its unperturbed counterpart.

Acknowledgements

This work was only possible due to the input and support of many people.

I would like to thank Prof. Dr. Thomas Schildknecht for his supervision and support. His vast experience in the field of Space Surveillance and Space Debris was very valuable.

I would like to thank Dr. Alessandro Vananti for the fruitful discussions and guidance throughout this work. His inputs were always very helpful in order for me to analyse my work and improve it.

I would also like to acknowledge my colleagues at the Astronomical Institute whose questions and feedback helped me in moving forward. The regular seminars organized by the institute were very interesting.

I would like to thank my family for their unwavering support throughout this work. This was a dream to begin with and my parents helped me live it. My brother was my cheerleader and friend. My partner's belief in me and my abilities helped me traverse through the difficult times.

Table of Contents

List of Figures

List of Tables

Nomenclature

Abbreviations

AIUB Astronomical Institute of University of Bern

AMR Area to Mass Ratio

AR Admissible Region

ASAT Anti-Satellite Weapon

ASPOS OKP Roscosmos Automated Warning System on Hazardous Situations in Outer Space

BFGS Broyden Fletcher Goldfarb Shanno

CCD Charge-coupled device

CMOS Complementary metal-oxide semiconductor

DSST Draper Semi-analytical Satellite Theory

ESA European Space Agency

EUMETSAT European Organisation for the Exploitation of Meteorological Satellites

FoV Field-of-View

GEO Geostationary Orbit

GNSS Global Navigation Satellite System

GPS Global Positioning System

GTO Geostationary Transfer Orbit

HAMR High Area to Mass Ratio

HEO High Earth Orbit

IADC Inter-Agency Space Debris Coordination Committee

IOD Initial Orbit Determination

ISON International Scientific Optical Network

KIAM Keldysh Institute of Applied Mathematic

LAMR Low Area to Mass Ratio

LEO   Low Earth Orbit

MCMC Markov Chain Monte Carlo

MD   Mahalanobis Distance

MEO   Medium Earth Orbit

MHT   Multiple Hypothesis Tracking

OBVIOD Optimized Boundary Value Initial Orbit Determination

pdf   probability density function

SLR   Satellite Laser Ranging

SNR   Signal-to-Noise Ratio

SRP   Solar Radiation Pressure

SSN   Space Surveillance Network

TSA   Too-short-arc

USSTRATCOM US Strategic Command

VA   Virtual Asteroids

VD   Virtual Debris

VP   Virtual Particle

ZIMLAT Zimmerwald 1 m Laser and Astrometric Telescope

ZimMAIN Zimmerwald Multiple Applications Instrument

ZimSMART Small Aperture Robotic Telescope

ZimTWIN Zimmerwald Twin Wide-field Instrument

Other Symbols

α Right Ascension

$\ddot{r}$ Second derivative of r

δ Declination

$\dot{\alpha}$ First derivative of α

$\dot{\delta}$ First derivative of δ

$\dot{\vec{u}}$ First derivative of $\vec{u}$

$\dot{\rho}$ First derivative of ρ

$\dot{r}$ First derivative of r

$\dot{\vec{r}}$ Geocentric velocity vector

μ or $\mu_{\oplus}$ Geocentric gravitational constant

$\mu_{\odot}$ Heliocentric gravitational constant

ρ Topocentric range

ρ_{2diff} Difference in computed and OBVIOD ρ_2 values

θ Transfer angle

a Semimajor axis

a_{max} Maximum semimajor axis

a_{min} Minimum semimajor axis

e Eccentricity

$E_{\odot}$ Heliocentric energy

$E_{\oplus}$ Geocentric energy

R_{SI} Radius of sphere of influence of earth

$\vec{r}$ Geocentric position vector

$\vec{r}_s$ Station position vector

$\vec{u}$ Line of sight vector from station to the observed object

$\vec{v}_s$ Station velocity vector

r   Geocentric distance

1 Introduction

Humankind's exploration of space started in 1957 with the launch of the first satellite Sputnik-1. The satellite launches following this event have helped improve life on our planet in several ways like weather forecasting, disaster management, GPS navigation to name a few. However, one side-effect of the increase in satellite population has been 'space debris' or 'orbital debris'(Musci et al., 2005; Vallado, 2007).

'Orbital debris is defined as any man-made object which is non-functional with no reasonable expectation of assuming or resuming its intended function, or any other function for which it is or can be expected to be authorized, including fragments and parts thereof.' (Schildknecht, 2007).

The space debris population is continuously increasing. Several mission-related objects like payload shrouds, instrument covers, solid rocket motors have led to its increase. After the end of life of a mission, the disintegration of thermal blankets have contributed to the rise in debris numbers. In almost 60 years of space activities, more than 5,200 launches have resulted in around 42,000 tracked objects in orbit, of which only about 1,200 are intact and operational (ESA, 2020). This growing population of space debris increases the threat to operational spacecraft and manned missions.

To mitigate this threat, the monitoring of the space environment and cataloguing of the debris is very important. This is done using optical surveys and radar observations. In the scope of this thesis we focus on optical surveys and challenges presented by the optical observations. Optical surveys result in angles-only observations of objects on very short arcs. These observations are sparse and cover a very small part of the orbit, hence the initial orbit determination becomes challenging. The orbits of the uncontrolled space objects evolve over time due to factors like their area-to-mass ratio, perturbations acting on them. The area-to-mass ratio (AMR) is a parameter to categorise space debris objects. Compact, satellite-like objects have AMR values of 1 m^2/kg and less (low area-to-mass ratio objects, LAMR); large and/or very light, foil-like objects have AMR values of more than 1 m^2/kg (high area-to-mass ratio objects, HAMR). The introduction extends to briefly describe the problem of space debris, the survey techniques used to observe the space objects, the observations resulting from surveys, and finally the overview of the methods used for the initial orbit determination from such observations.

In the three-year period between 2015 and 2018, 873 small satellites were launched. The estimates are that the next decade will see nearly 10,000 small satellites launched. Moreover, the satellite constellations will increase the space traffic in the next few years and operations will become harder. One example is Starlink constellation from SpaceX, with a 4425-elements constellation dominates in terms of number of satellites in constellations between the period 2019-2024 (Curzi et al., 2020). The number of space objects is expected to increase soon, to huge numbers especially if the current launch trends remain unchanged. The goal of this thesis is, therefore:

To identify an algorithm capable of addressing the problem of initial orbit determination of space debris in the GEO region with the addition of perturbations, in order to catalog objects in highly-perturbed orbits.

1.1 Space Debris

The orbits around Earth can be classified into different types based on their altitudes, usually called the Low Earth Orbit (LEO), the Medium Earth Orbit (MEO), and the Geostationary Orbit (GEO). The LEO regime ranges from about 160 km to 2,000 km. LEO's proximity to Earth makes it useful for several reasons. It is most commonly used for satellite imaging, as being near the surface allows it to take images of higher resolution. However, these orbits are not very suitable for telecommunication due to their high orbiting velocities. A geostationary orbit is a circular orbit in the equatorial plane at an altitude of 35,786 km, and an orbital period equal to 23 hours 56 minutes and 4 seconds. The orbital period matches with the rotation of the earth and the satellite appears stationary over one place on the Earth's equator. This is the reason due to which these satellites are mainly used for:

1. Telecommunications: TV broadcasting, voice and internet

2. Earth observation purposes (remote sensing)

3. Meteorology

4. Science

The Medium Earth Orbit is between the LEO and GEO altitudes. These orbits are mainly used for navigation purposes. Many of these satellites are launched into different orbits to cover large parts of the world. In addition, there are other categories of orbits such as Highly Eccentric Earth Orbit (HEO) with apogee heights higher than those of GEO. Some of the orbits are defined as MEO-GEO crossing orbits, LEO-MEO crossing orbits, GEO Transfer orbits, Navigation Satellite orbits. The orbit categories are shown more in detail in Table 1.1 (ESA, 2020).

The number of debris objects, their combined mass, and the total area they take up has been steadily increasing. This is further fuelled by a large number of in-orbit break-ups of spacecraft and rocket stages. The total area that space debris takes up is important, as it is directly related to how many collisions we expect in the future. The change in object area since the beginning of the launches is shown in Fig. 1.1. According to the present trends, collisions between debris and working satellites are predicted to overtake explosions as the dominant source of debris (ESA, 2020). The effect whereby the generation of space debris via collisions and explosions in orbit could lead to an exponential increase in the amount of artificial objects in space, in a chain reaction which would render spaceflight too hazardous to conduct, was first postulated by Donald Kessler in 1978 (Kessler and Cour-Palais, 1978). Space debris first of all is a risk for the space missions. The debris pieces are mainly a threat due to their high relative velocity with respect to the other objects in orbit. In LEO objects move with velocities of 7-8 km/s (about 27,000 km/h) with respect to an Earth fixed frame. Consequently, the released energy during a collision is remarkably high. On average, objects in LEO have relative velocities of about 10 km/s, and in case of a head-on collision the relative velocities may even reach 16 km/s. Impacts of even small particles may cause

Orbit	Description	Definition		
GEO	Geostationary Orbit	$i \in [0, 25]$	$h_p \in [35586, 35986]$	$h_a \in [35586, 35986]$
IGO	Inclined Geosynchronous Orbit	$a \in [37948, 46380]$	$e \in [0.00, 0.25]$	$i \in [25, 180]$
EGO	Extended Geostationary Orbit	$a \in [37948, 46380]$	$e \in [0.00, 0.25]$	$i \in [0, 25]$
NSO	Navigation Satellites Orbit	$i \in [50, 70]$	$h_p \in [18100, 24300]$	$h_a \in [18100, 24300]$
GTO	GEO Transfer Orbit	$i \in [0, 90]$	$h_p \in [0, 2000]$	$h_a \in [31570, 40002]$
MEO	Medium Earth Orbit	$h_p \in [2000, 31570]$	$h_a \in [2000, 31570]$	
GHO	GEO-superGEO Crossing Orbits	$h_p \in [31570, 40002]$	$h_a > 40002$	
LEO	Low Earth Orbit	$h_p \in [0, 2000]$	$h_a \in [0, 2000]$	
HAO	High Altitude Earth Orbit	$h_p > 40002$	$h_a > 40002$	
MGO	MEO-GEO Crossing Orbits	$h_p \in [2000, 31570]$	$h_a \in [31570, 40002]$	
HEO	Highly Eccentric Earth Orbit	$h_p \in [0, 31570]$	$h_a > 40002$	
LMO	LEO-MEO Crossing Orbits	$h_p \in [0, 2000]$	$h_a \in [2000, 31570]$	
UFO	Undefined Orbit			
ESO	Escape Orbits			

Table 1.1 – Ranges defining each orbital class with semimajor axis, eccentricity, inclination, perigee height and apogee height. The units are km and degrees (ESA, 2020).

large damage with potentially catastrophic consequences. The fact that such impacts really take place is confirmed by the detailed inspections of the shuttle after each mission. On average, one window has to be replaced after each flight due to impacts of small particles (Schildknecht, 2007).

Two major fragmentation events in GEO and HEO were observed in 2018. Based on measurements of the International Scientific Optical Network (ISON) and the Roscosmos Automated Warning System on Hazardous Situations in Outer Space (ASPOS OKP) fragmentation of the Titan 3C Transtage 1969-013B, SSN 3692 on February 28, 2018, was identified. More than 100 objects detected by optical instruments operated by ASPOS OKP, the Astronomical Scientific Center ISON, ISTP RAS, and other Russian scientific and research organizations could be identified as fragmentation debris related to this event. Another massive fragmentation event in HEO related to the Atlas Centaur upper stage 2014-055B, SSN 40209, which occurred on August 30, was identified based on the same data sources. Many of the fragments of this event are crossing the operational GEO region. In March and April 2019 two additional breakup events of Atlas Centaur upper stages took place (Schildknecht et al., 2019).

Out of the thousands of objects tracked in orbit using radars and other methods, anyone could damage or destroy a functioning satellite if a collision were to occur. In 2018, ESA-operated satellites had to conduct 27 debris avoidance manoeuvres, a number that is growing year by year. The particles with size larger than a few centimeters are usually generated by in-orbit explosions, which can be triggered by several mechanisms such as 1) failures of batteries, 2) ignition of residual fuel, 3) burst of a pressurized vessel, or by 4) intentional ignition of a self-destruction mechanism. Collisions of objects with one another could also lead to an increase in the space debris population. Objects in the space environment can be categorized as identified and unidentified objects. The identified objects are the ones that can be traced back to the launch event such as upper stages, payload mission-related objects
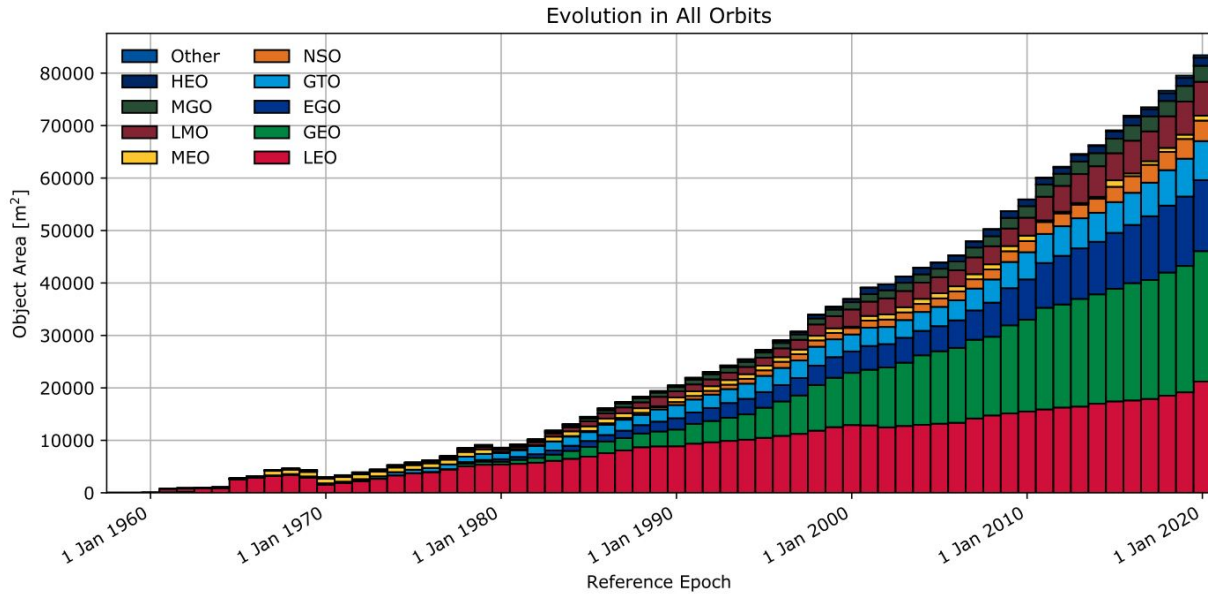
Fig. 1.1 – The evolution of the object area in geocentric orbits by orbit class (ESOC, 2020).

including optical instruments, rocket fragmentation debris. The unidentified objects are the ones for which this tracing is impossible. The evolution of the number of space objects since the beginning of the space age is shown in Fig. 1.2 (ESA, 2020), the graph represents the data corresponding to the object types.

When observing the temporal evolution of a debris cloud, e.g. shortly after an explosion, one can discover that the fragments are dispersed quickly over a large volume in space. Fig. 1.3 shows a simulation of an explosion in LEO. The simulation ejected the fragments according to the expected velocity and mass distributions uniformly into all directions. The laws of celestial mechanics tell, however, that the cloud is not immediately expanding into a spherical shell, but that the fragments in a first stage are distributed along the orbit of the parent body. Fig. 1.3 shows the cigar-shaped distribution of the fragments immediately after the explosion on the left side. After several hours the debris cloud has expanded into a toric region along the parent orbit (Fig. 1.3 middle). The figure on the right shows the situation 3 years after the event. The fragments are now dispersed in an almost closed shell around the globe. The dispersion is caused by the perturbing forces of the gravity field (mainly due to the equatorial bulge), which force the orbital planes to precess, but with a slightly different rate for the original slightly different orbits of the fragments. This mechanism is responsible for the fact that each debris cloud in LEO is sooner or later causing a global 'pollution' roughly at the height of the original orbit.

The testing or use of destructive anti-satellite (ASAT) weapons that physically collide with satellites at high speed is also a source of debris. In 2007, the intentional collision of an anti-satellite (ASAT) weapon with the Chinese Fengyun 1C spacecraft showed that collisions between resident space objects can be very damaging to the environment. The Fengyun breakup produced more than 2,500 trackable debris fragments and increased the size of the U.S. Space Surveillance Network (SSN) catalog by over 25% (Stansbery and Johnson, 2007). The following year, the U.S. did an ASAT test to destroy one of its spy satellites called USA 193 creating 174 pieces of trackable debris, plus non-trackable shards.
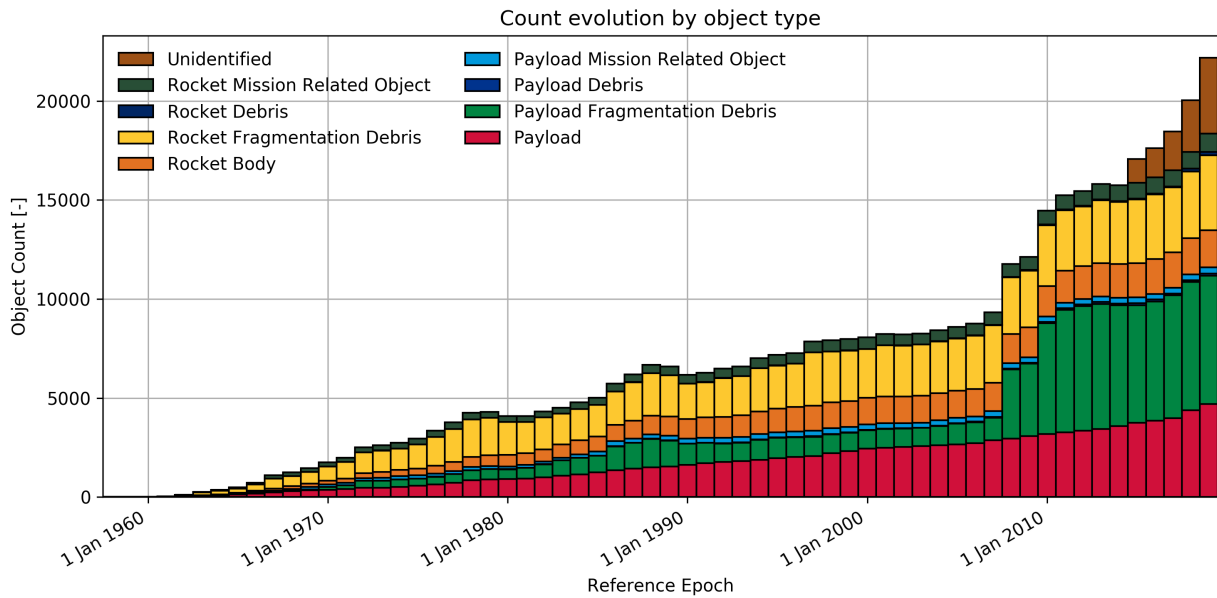
Fig. 1.2 – The evolution of the number of objects in all orbits (ESOC, 2020).

Fig. 1.3 – Simulated explosion in LEO; immediately after the explosion (left), after some hours (middle), and after 3 years (right) Schildknecht, 2007.

The bulk of that debris re-entered the atmosphere within days, though in certain cases it took months (Porras, 2018).

The time for which the debris pieces remain in the orbit depends on their orbit altitudes. In low altitude orbits, there is a natural 'sink' for space debris: the atmosphere. All objects in orbits below about 1000 km of altitude constantly collide with residual air molecules and atoms. As a consequence of this so-called air drag the object is decelerated and loses kinetic energy, which eventually leads to the decay of the orbit. During the re-entry into the atmosphere the drag from the denser air layers heats the object by friction and it eventually, with the exception of very massive objects, burns up. The deceleration rate depends on the density of the air and thus strongly on the altitude. An additional important factor is the area-to-mass ratio of the object: 'lightweight' pieces with a comparable large area are subject to a stronger deceleration than 'massive', compact objects.

At altitudes up to 600 km, objects without an active propulsion system will re-enter the atmosphere within a few months up to several years. For objects starting at altitudes of 600–800 km, it takes several decades before they burn up in the atmosphere. Objects in orbits at altitudes above 800 km remain in orbit for several hundred years. Above altitudes of a few 1,000 km, in particular in GEO, orbits have an 'indefinite' lifetime and objects will stay there 'forever'.

The Inter-Agency Space Debris Coordination Committee recommends a minimum altitude increase (in km) which is given as:

$$\Delta H = 235 + 1000 \cdot C_R \cdot A/m \tag{1.1}$$

where C_R is the solar radiation pressure coefficient (usually with a value between 1 and 2), A is the average cross-sectional area in square metres and, m is the mass of the satellite in kg. Given these guidelines and recommendations one would expect that the geostationary ring is a well protected and unlittered space (Jehn et al., 2007). However, not many operators complied with these guidelines at the beginning of the last decade. These trends have changed in the current decade. Between 85% and 100% of all payloads reaching end-of-life during the current decade in the GEO protected region attempt to comply with the space debris mitigation measures, see Fig. 1.4. Between 60% and 90% do so successfully. The compliance trend is asymptotically increasing (ESOC, 2020).

1.2 Optical observations of space debris

Objects in lower altitudes such as in the Low Earth Orbit (LEO) are monitored by radar telescopes which are less dependent on weather and time conditions. Optical telescopes are used to observe space debris objects in higher altitudes. The US Strategic Command (USSTRATCOM), a military entity of the USA, maintains a catalog of thousands of known 'large' objects. Sensors of the so-called 'space surveillance network' (SSN) continuously collect measurements, which are then combined with earlier data to produce orbits. The SSN consists of a global network of radar stations and a series of optical telescopes.

Space debris can be detected with optical telescopes when the objects are illuminated by the Sun while the sky background is dark. For the LEO region this is only the case during 1–2 hours after sunset and before sunrise. Most optical telescopes have a narrow field of view of the order of 1°or less. Their big advantage over radars, however, resides in their
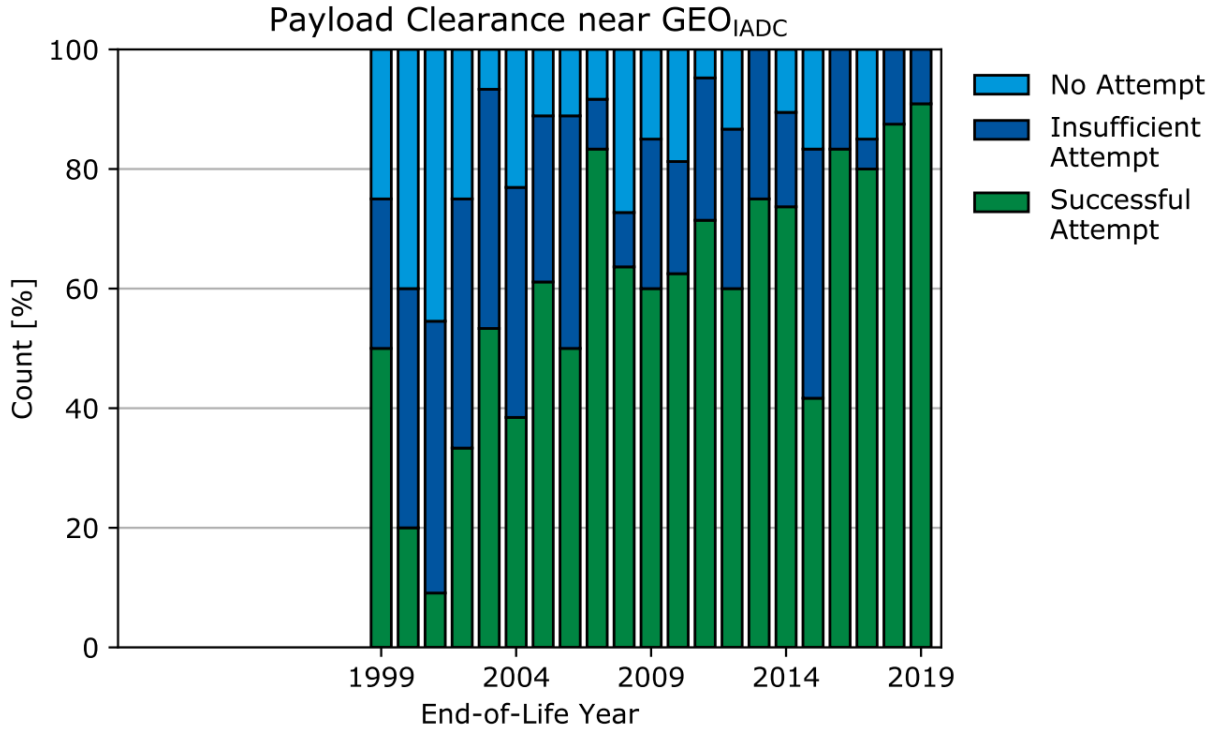
Fig. 1.4 – Trend of adherence to disposal guideline in GEO by IADC (ESOC, 2020).

higher sensitivity in terms of object size at large distances: while the radar sensitivity falls off proportional to the distance to the fourth, the sensitivity of optical instruments is only reduced proportional to the distance squared. This is the main reason why optical telescopes are primarily used to investigate the debris environment at high altitudes (Schildknecht, 2007).

1.2.1 The telescope set-up

The principle setup of an optical sensor system consists of a telescope and an attached detector. The detection is either performed by an integrated photon counting array (e.g. a charge-coupled device sensor) or an active-pixel sensor (e.g. using complementary metal-oxide-semiconductors) (Schildknecht, 2007). The aperture and focal length of the telescope define the field of view and the angular resolution which can be achieved by the detector pixels. Additionally, the pixel size, focal ratio, and the other parameters have a direct impact on the telescope performance, namely the signal-to-noise ratio and accuracy, and are all connected to each other. The overall design of a sensor is thus a multivariate optimization process and returns different results depending on the planned observation scenario and strategy. Efficient optical surveys require dedicated telescopes with the following features:

- large aperture,

- large field of view (FOV), and

- sensitive detector.

An optimized space debris observation system would need a very fast optical system with a large FOV in order to allow for reasonably sized CCD sensors (mosaics) in the focal plane. The difficulties in manufacturing fast optics could be reduced by allowing for some degradation in the imaging quality. The next section will address some important technical aspects of the surveys.

The Zimmerwald Observatory is affiliated with the Astronomical Institute of the University of Bern. It performs the optical observations for Space Debris, Asteroids and Comets. It is located 10 km South of Bern, Switzerland. Currently optical observations are performed with the 1 m Laser and Astrometric Telescope, ZIMLAT (Fig. 1.5 and Fig. 1.6), the 0.2 m Small Aperture Robotic Telescope, ZimSMART (Fig. 1.7), the Zimmerwald Multiple Applications Instrument, ZimMAIN, and Zimmerwald Twin Wide-field Instrument, ZimTWIN. In the following subsections, a brief introduction to ZIMLAT and ZimSMART is given. If the reader wants to know about the ZimMAIN and ZimTWIN please refer to (Cordelli et al., 2019).

Both ZIMLAT and ZimSMART are equipped with state-of-the-art CCD cameras with low readout-noise and high quantum efficiency. While ZIMLAT is used for follow-up observations of small-size space debris objects to keep their orbital information updated and also to determine their physical characteristics, the main objective of ZimSMART is to perform systematic surveys of high-altitude orbit regions, in particular of the geostationary ring (GEO). The goal of these observations is to build-up and maintain orbit catalogues of objects in high-altitude orbits, including a catalogue of small-size debris with high area-to-mass ratios. Orbits from these catalogues are used to routinely track and characterize space debris with ZIMLAT.

ZIMLAT

ZIMLAT (installed in 1997) has field of view (FoV) as 26 x 26 arcmin, which is used either for laser ranging to satellites (SLR) or for optical observation of positions and magnitudes of near-Earth objects. These objects were either discovered by the ESA space debris telescope in Tenerife, Spain or by observatories of our international partners, in particular the International Scientific Optical Network (ISON) led by the Keldysh Institute of Applied Mathematics (KIAM). The resulting positions and orbital elements are shared among the partners. ZIMLAT observations play a key role in the maintenance of orbits of objects with high area-to-mass ratios (Herzog et al., 2013). This telescope is operated on a 24/7 basis and different research projects make use of it. It hosts both the satellite laser ranging (SLR) system and the astrometric equipment. The equipment of the SLR system is in the Coudé focus of the telescope; while the astrometric equipment, as can be seen in Fig. 1.6, is hosted in the Nasmyth platform that contains both CMOS and CCD cameras. These different camera types are employed in different projects, for more information consult (Cordelli et al., 2019). The specifications of ZIMLAT are as follows:

- 4 focal stations: f = 1.2m, 2 x 4m, 8m,

- 2k x 2k CCD

- 3k x 3k CCD

- Coudé path for Laser

- Fast mount: 30°/s, 20°/s2

Fig. 1.5 – ZIMLAT (Herzog et al., 2013).
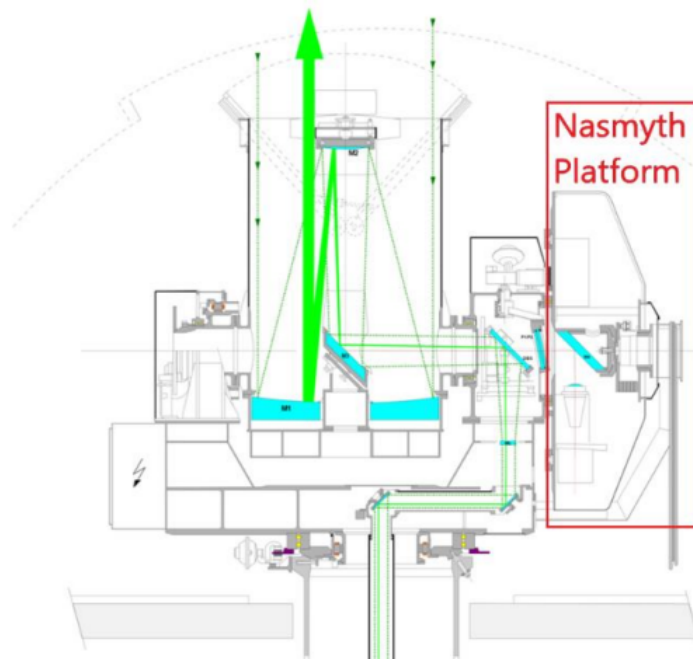
Fig. 1.6 – The sketch of ZIMLAT telescope (Cordelli et al., 2019).

ZimSMART

The second oldest telescope is the Zimmerwald Small Aperture Robotic Telescope (ZimS-MART, visible in Fig. 1.7). It has 20 cm aperture with a resulting 3.6 x 3.6 degree FoV. Due to the wide FoV, the main purpose of this telescope is the discovery of space debris in the GEO region. One of its main achievements is the buildup and the maintenance of the

GEO space debris AIUB internal catalog. The cut off at 16 magnitude (1 meter-size object at GEO altitude) is due to the aperture size of the telescope and the standard exposure time used for the actual survey campaign, which is only 8 seconds. As for ZIMLAT, also ZimS-MART is acquiring regularly GNSS satellites which are used to estimate the telescope time bias and monitor the astrometric accuracy of the extracted series of observations. During the acquisition the telescope is looking in a direction fixed with respect to the Earth. The survey fields are chosen for a fixed right ascension and declination stripes separated by 3.5°. For each field there are 5 images taken with an exposure time of 8 seconds. The images are analysed with an automated procedure to find any moving object. Astrometric positions and apparent magnitudes are determined for each detection of a moving object.

ZimSMART was used to acquire first observations of an ejected cooler cover. It belonged to the EUMETSAT's weather satellite MSG 2 which was launched on December 22, 2005. Just prior to reaching operational altitude the cooler cover was ejected in a special manoeuvre, several hundred kilometres away from the geostationary orbital plane, ensuring that it cannot come into contact with other operational satellites. On January 4, 2006, AIUB successfully acquired first observations of the cooler cover using ZimSMART. The cooler cover appears as dot as it is nearly stationary with respect to the Earth rotation. The stars appear as streaks (Fig. 1.8).

Fig. 1.7 – ZimSMART (Herzog et al., 2013).
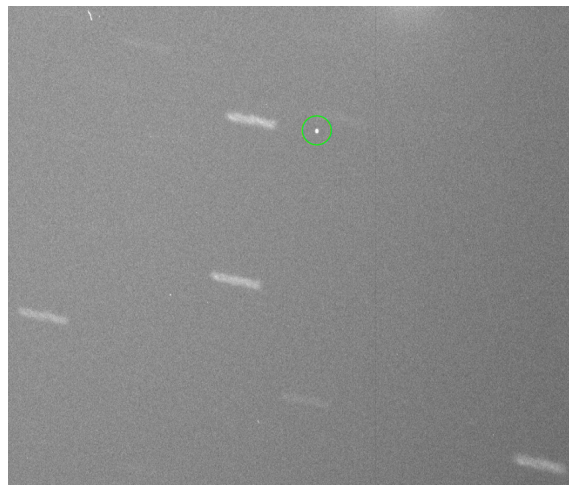
Fig. 1.8 – Image of the cooler cover, marked by the green circle (Herzog et al., 2013).

1.2.2 Optical surveys for space debris in GEO

Most uncontrolled debris in GEO is expected at orbital inclinations less than or equal to 15 degrees. This is due to the fact that the orbital planes of uncontrolled GEO objects precess around a stable plane, the so-called Laplacian plane, which has an inclination of about 7.5 degrees with respect to the equatorial plane. This precession is due to the combined effect of the Earth's oblateness, and perturbations exerted by the Moon and the Sun. The precession period is about 50 years. The inclination of uncontrolled objects starting in the equatorial plane will gradually increase to 15 degrees during the first 25 years and then decrease back to 0 degrees during the next 25 years. As a result of this systematic orientation of the orbital planes there is a strong correlation between the right ascension of the ascending node and the inclination. Consequently the daily motions of the objects projected to the celestial sphere exhibit a characteristic pattern. All objects with the same inclination have their culmination points all close to the same right ascension. Due to this systematic orientation of the orbital planes the number density of the catalogued objects projected to the celestial sphere looks as shown in Fig. 1.9 (Schildknecht et al., 1999). The retrograde motion of the ascending node for increasing inclination generates a sort of caustic pattern. This region of higher density is due to the intersection of orbits with different inclinations. We find it close to the ascending node at negative declination and close to the descending nodes and at positive declination. Fields in the caustic corresponding to different orbital inclinations may be selected in order to increase the detection rate (Schildknecht et al., 2001).

Debris released from objects in GEO, e.g. mission related objects or material released due to aging processes, is expected to stay in orbits similar to the orbits of their parent bodies. Even pieces stemming from explosions in GEO will generally remain in the GEO region. The energy increment or decrement they get during the explosion is usually not sufficient to considerably alter their orbital plane or their semimajor axis. The debris will not only start with orbits similar to their parent objects, but their orbits will also undergo similar perturbations and thus evolve in a similar way (the latter may not be true for objects with a very large area to mass ratio which react differently to radiation pressure forces). It is therefore reasonable to assume the simple hypothesis that the catalogued GEO objects trace the debris population. It is obvious that the detailed orbital characteristics of these two populations will certainly differ from each other (debris from distinct explosion events) but in general they are expected to occupy the same region in the orbital element space (Schildknecht et al., 2004).

Sky surveys are used to look for the space objects. The survey fields could be wide, covering a big portion of the sky, or deep surveys which are focused on smaller areas and specialized to focus on certain objects or types of measurements. When defining the search fields for a survey there is a series of observational constraints to be taken into account. First of all the objects should be observed under good illumination conditions (the so-called phase angle should be small), which means that the best locations are near the Earth shadow cone (but still outside the shadow region!). Dense stellar background regions, in particular the Milky Way, must be avoided. The fields should be at high elevations for a good part of the night; the angular distance from the moon should be maximized. Last but not least the field should cover the region of the catalogue population where one expects – according to the mentioned hypothesis – the most debris pieces.

A typical survey series is processed in three steps:
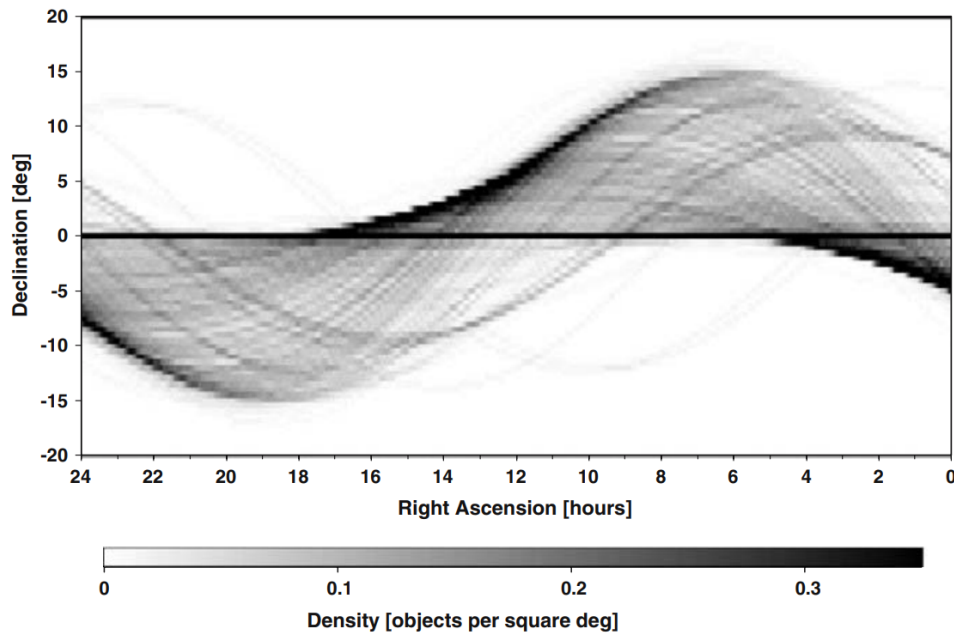
Fig. 1.9 – Apparent density of the cataloged GEO objects in the right ascension–declination-space as seen from the geocenter. The density is given in objects per square degree (status 2001) (Schildknecht, 2007).

1. Search for moving objects.

2. Determination of celestial coordinates for all moving objects (astrometry).

3. Orbit determination and correlation of found objects with catalog; display of results.

If an object with a reasonable apparent motion is found on a series of frames (step 1) its position in a celestial reference frame is determined on each exposure by means of reference stars (step 2). Here 'reasonable' means 'within the range of expected apparent motion for a near GEO object'.

Survey strategy

An 'optimum' survey may aim at the detection of as many different objects with as few search frames as possible. On the other hand, one could also search for as many objects as possible with a given combination of orbital elements. The aim of an object survey is thus not simply a homogeneous coverage of the celestial sphere but a homogeneous coverage of the space of orbital elements or part of it. For an optimum coverage of the element space one may take advantage of the fact that a given field at the sky is crossed by objects on many different orbits. Observing at the same right ascension and declination for a long time span is therefore equivalent to observing an extended section in the element space. Observing the same field for 24 hours leads to the observation of all objects occupying this element space section. Observations of the same field for several hours can be statistically extrapolated to the entire population in the element space section, because uncontrolled objects may be assumed to be equi-distributed in longitude. For objects on near-circular

geostationary orbits the elements of interest are inclination i, right ascension of ascending node Ω, semimajor axis a (resp. drift rate Δn), and longitude l at a given epoch. The last two elements (location of object along orbit) can be covered by observing the same right ascension and declination for a long time. The first two elements (location of orbital plane) are covered by selecting different search fields at the sky (Schildknecht et al., 1999).

Scanning of declination stripes

The detection technique is based on an algorithm comparing several consecutive frames of the same field in the sky. Fixed background stars are identified on a series of frames and the remaining part of the frames scanned for any additional objects. In order to optimize the signal-to-noise-ratio (SNR) for the objects of interest they are tracked during the exposures, which, in the case of GEO objects, means that the telescope is stopped. For GTO objects the tracking is of the order of 5–10 arcsec/s in hour angle (Schildknecht et al., 2004). As a consequence the stellar background is drifting across the field of view during the exposure, or in other words the stars leave trailed images on the frames. After each exposure the telescope is moved in a way that the same area of the sky is passing the field of view at the next exposure (see Fig. 1.10). With this method the telescope slowly scans the GEO ring from east to west at a fixed declination, while it is following the stars.
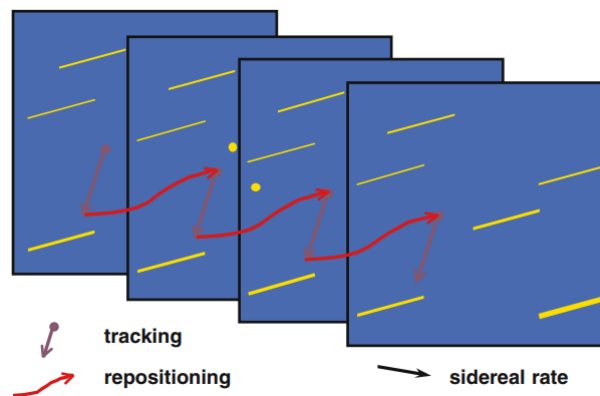
Fig. 1.10 – Tracking scenario for surveys. The telescope is tracking the object with its expected motion during the exposure and is repositioned between the exposures in order to always observe the same field in the sky (Schildknecht, 2007).

Masking Technique

There are many different approaches to detect 'moving' objects with respect to the stars. All methods must be optimized in terms of speed, given a large amount of data per frame. One of these methods is the masking technique described e.g. in (Schildknecht et al., 1995). A reference frame is used to generate a mask covering every object found on the frame. For each object, the digital mask is made slightly larger than the original object image itself. The subsequent search frames are then scanned using this mask. Consequently, only the portion of the frame that contains no stars must be searched for unknown objects. The same reference mask can be applied for a long time interval if siderostatic tracking is used. In the earth-fixed horizon system, this corresponds to a scanning strip in the sky (e.g. for the search of geostationary objects). The time necessary to generate the mask is negligible

in this case. If the search is performed with a fixed telescope, the mask has to be extended continuously to the east.

Signal-to-noise ratio

In order to get a good signal-to-noise ratio (SNR), the objects should be tracked. If the object's light is integrated onto the same pixels and the readout noise of the chip is negligible, the SNR increases with the square root of the exposure time. If, on the other hand, the object is moving with respect to the pixels, the maximum achievable SNR is limited by the background noise. The optimum exposure time, in this case, is a few pixel crossing times. The optimum exposure time is a trade-off between 1) the length of the star trails (i.e. the decrease of the unmasked part of the frame) and 2) the SNR of faint objects (i.e. the detection limit for orbiting objects). It depends on the star density in the selected field (Schildknecht et al., 1999). Extending the integration time would in case 1 increase the probability that the image of the moving object is hidden by a trailed image of a star and in case 2 reduce the SNR (Schildknecht et al., 1997). For GEO and GTO surveys the optimum exposure times are of the order of a few seconds (Schildknecht et al., 1995).

The signal-to-noise ratio of faint objects may be increased by tracking with the expected motion of the objects of interest. In order to increase the detection probability, the search should be performed at the point of slowest motion, e.g. at the culmination point for the geostationary objects with non-zero orbital inclination or at the apogee for GTO objects. If the orbital plane is known e.g. when looking for debris of an exploded upper stage or satellite a few days after disintegration, the search can be carried out along-track while tracking with the expected motion (Schildknecht et al., 1995). Maximum SNR may be achieved by tracking with the expected apparent motion of the objects of interest during exposure, maximizing the detection probability for objects with a specific orbit type (Schildknecht et al., 1997).

Orbit determination and correlation with the catalog

An important goal of space debris surveys is to detect uncatalogued objects and determine the orbits of detected objects. This is done in order to study the populations of debris as a function of the orbital elements and to update the catalogue (step 3 in processing of survey series). In order to get orbit information for a debris, several precise astrometric positions have to be measured which involves the determination of the CCD coordinates of the object image and their transformation to celestial coordinates. The centroid of a relatively faint object image can be determined with a precision of a tenth of a pixel. If at least one reference star is present on a frame containing a space object, the CCD coordinates of the object image can be transformed to celestial coordinates with an accuracy of a few tenths of an arcsecond provided the scale of the mapping, the orientation of the camera, and possible optical distortions are known (calibrated off-line). From the detection frame and from a second frame (used for confirmation) two initial positions may be extracted for an object (Schildknecht et al., 1997).

The determination of an orbit for the newly detected objects is a critical and non-trivial task. To first order the task consists essentially in finding a particular solution of the one-body version of the equations of motion:

$$\ddot{\boldsymbol{r}} = -\mu \frac{\boldsymbol{r}}{r^3}, \tag{1.2}$$

where μ is the product of the constant of gravitation and the mass of the central body, $\boldsymbol{r}$ the geocentric position vector of the object (and r its length) and $\ddot{\boldsymbol{r}}$ its second time derivative. If the length of the orbit arc is short (a small fraction of the revolution period), the orbit model may be sufficient to represent the observations within the arc with sufficient accuracy. If the arc length is growing, the equations of motion become more elaborate. Symbolically, we write them as follows:

$$\ddot{\boldsymbol{r}} = -\mu\frac{\boldsymbol{r}}{r^3} + \delta\boldsymbol{f}(t; \boldsymbol{r}, \dot{\boldsymbol{r}}, p_1, p_2, \ldots, p_m),\tag{1.3}$$

where $f(\ldots)$ is the perturbing acceleration and p_i, $i = 1, 2, \ldots, m$ are additional unknown parameters, so-called dynamical parameters of the orbit; one may think of them as parameters characterizing radiation pressure or atmospheric drag. Usually, one may assume that the absolute value of $\delta\boldsymbol{f}(\ldots)$ is much smaller (typically by a factor of the order of 10^3) than the absolute value u/r^2 of the main term (Schildknecht, 2007). Factors like area-to-mass ratio of the object and the altitude of the orbit also play a role in determining the magnitude of perturbing accelerations. In the present algorithms used at AIUB, the classical Keplerian orbital elements are used as the unknowns to characterize the initial values of the parameter estimation process. They are however interpreted as the osculating elements referring to a particular epoch t_0 (initial epoch in this case). These osculating elements are derived from the position and velocity vectors $\boldsymbol{r}(t_0)$ and $\dot{\boldsymbol{r}}(t_0)$ using the formulae of the two-body problem. The orbit to be determined may then be written as the solution of an initial value problem (as long as the orbit model is assumed to be purely deterministic):

$$\begin{aligned}\ddot{\boldsymbol{r}} &= -\mu\frac{\boldsymbol{r}}{r^3} + \delta\boldsymbol{f}(t; \boldsymbol{r}, \dot{\boldsymbol{r}}, p_1, p_2, \ldots, p_m)\\ \boldsymbol{r}(t_0) &= \boldsymbol{r}(a(t_0), e(t_0), \ldots, T_0(t_0))\\ \dot{\boldsymbol{r}}(t_0) &= \dot{\boldsymbol{r}}(a(t_0), e(t_0), \ldots, T_0(t_0))\end{aligned}\tag{1.4}$$

When determining a first orbit the non-linear orbit determination problem is not reduced to a linear one, but instead the attempt is made to directly solve the non-linear problem. A modified Gauss method is used to solve a boundary value problem:

$$\begin{aligned}\ddot{\boldsymbol{r}} &= -\mu\frac{\boldsymbol{r}}{r^3} + \delta\boldsymbol{f}(t; \boldsymbol{r}, \dot{\boldsymbol{r}})\\ \boldsymbol{r}(t_a) &= \boldsymbol{o}(t_a) + \rho_a\boldsymbol{e}_a\\ \boldsymbol{r}(t_b) &= \boldsymbol{o}(t_b) + \rho_b\boldsymbol{e}_b,\end{aligned}\tag{1.5}$$

where the boundary epochs t_a and t_b must be selected as two observation epochs (not necessarily the first and the last one). The indices a and b thus characterize two observation numbers. $\boldsymbol{o}(t)$ is the barycentric position vector of the observer at epoch t, $\boldsymbol{e}_a$, $\boldsymbol{e}_b$ are the observed unit vectors and ρ_a, ρ_b are the (originally unknown) distances. The osculating elements as unknowns are replaced by the following six parameters (as auxiliary unknowns to be determined first):

$$p_1, p_2, \ldots, p_6 = \rho_a, \rho_a, \alpha_a, \alpha_b, \delta_a, \delta_b,\tag{1.6}$$

where α_a, α_b, and δ_a, δ_b are the right ascension and the declination of the observed astrometric places. The details of the particular method used to solve the problem Eq. (1.5) are given in (Beutler, 2004).

The series of discovery observations from space debris surveys, however, is usually very short and consists of a few position measurements spread over a time interval of a few minutes. Given the orbital periods of the objects, which are of the order of 1 day, it is obvious that these extremely short arcs prevent determining full six-parameter orbits. There are in principle two possibilities to eventually obtain a full orbit in these cases, (a) acquire follow-up observations in near real time or (b) to plan the surveys in a way that most objects of interest will appear incidentally on several observation series during the same or during consecutive nights. In the first case we may determine a circular orbit from the discovery observations and compute ephemerides to perform follow-up observations. Depending on the type of orbit (GEO, GTO, etc.) and the field of view of the sensor used for the follow-up these observations must be acquired within a time interval of 15 min up to several hours after the discovery (for details see (Musci et al., 2005)). Additional observations will then be required during the following night to finally derive an orbit allowing recovering the object after many revolutions.

In the second case all observations from different epochs, e.g., from different nights, have to be cross-correlated in order to find detections which belong to the same object. The latter is eventually best tested by trying to fit an orbit through all observations, which are supposed to stem from the same object. However, this process is computationally intensive and we need a method to pre-select candidate observations. Algorithms used to select these candidates should take into account the position and the apparent motion from the single detections and must confine the orbital element space to a region as small as possible but still appropriate for the objects of interest.

The correlation with an existing catalog of orbits is finally done by comparing either the observed positions or the determined orbital elements, or a combination thereof, with the corresponding quantities derived from the catalog. This correlation should be based on the known accuracy of the catalog orbits, i.e., should make full use of possible covariance information.

1.2.3 Optical measurements

In this work only optical measurements are considered. The optical measurements are treated after the astrometry has been performed. With an optical system a pair of angles $(\alpha, \delta)_t$ at an epoch t can be observed, where the angles are defined as in the schematic given in Fig. 1.11. This topocentric reference frame is centered on the optical sensor, and oriented in the same way as the geocentric equatorial coordinate system (i axis parallel to the vernal equinox direction and ij plane parallel to the equatorial plane) (Vallado, 2007).
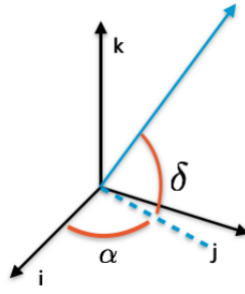
Fig. 1.11 – Definition of measured angles right ascension α and declination δ (Zittersteijn, 2017).

The position of the object is computed with respect to the reference stars, as mentioned in the previous sections. For the optical data obtained at the Zimmerwald observatory the uncertainty of the extracted position is around 0.7 arcsec $\leq \sigma \leq 1$ arcsec. Note that in this sidereal tracking mode the rotation of the Earth is not corrected for, therefore the stars appear as streaks and a GEO object is a point. Other tracking modes are possible. This thesis does not concern itself with the extraction of the astrometric position. The interested reader is referred to (Früh and Schildknecht, 2012); (Schildknecht, 2007); (Schildknecht et al., 1997); (Schildknecht, 1994).

Space debris is typically observed multiple times in rapid succession. Such a series of observations is also called a tracklet or very short arc and consists of four to seven observations made at 15 s to 30 s intervals (in the case of the Zimmerwald observatory). A schematic representation of such a series is given in Fig. 1.12.
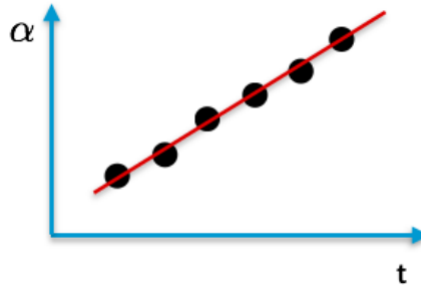
Fig. 1.12 – A schematic representation of a tracklet, which is a series of closely spaced optical observations (Zittersteijn, 2017).

A series of observations are made to be sure that an object has been observed and to obtain a larger number of observations which is beneficial when e.g. a least-squares estimator is applied to them. The tracklet formation process consists of associating the individual observations to one another to form the correct series of observations. In surveys of wide-field telescopes possibly many non-resolved object images are present on the single frames of the series. Hence, reliable methods have been found to associate the object images stemming from the same object with each other, also called object image linking. Such a method has been proposed by (Früh and Schildknecht, 2012).

The tracklets of object images allow extracting exact positions which are essential for the orbit determination process. To make the most of the information received from the images, this work exclusively considers that space debris is observed in this manner. A tracklet

describes such a short portion of the object's orbit (e.g. for a GEO orbit about 2-5 min of a 24 hr period) that a straight line can approximate the object's motion during that period. By fitting a straight line to the observations in a tracklet both the average position and the angular rate of the object are found. This is a so-called attributable as given in Eq. (1.7). The epoch of the attributable is the average epoch of the observations in the series.

$$\theta_t = (\alpha, \delta, \dot{\alpha}, \dot{\delta})_t \tag{1.7}$$

An important aspect of the observations and tracklets is the quantification of their uncertainty. In general, it is assumed that the noise on a single measurement is Gaussian. Therefore a single measurement is described with a mean value and a standard deviation σ_0. The σ_0 can be characterized and depends on the telescope, CCD hardware, and image processing software used. However, it is arduous to do so and is in itself not perfectly accurate. Another option is to use the uncertainties that are provided by the least-squares straight line fit. In this work, all measurement errors are assumed to be Gaussian with no bias.

1.3 Existing methods of initial orbit determination

Some methods contributing to initial orbit determination using optical observations originated from the asteroid community. Milani et al. (2004) developed the principle of admissible regions, they did it over the range and range-rate space. They restricted the space of orbital solutions to the physically meaningful ones. An asteroid orbit, for instance, should have a stable elliptic orbit around the Sun. They did so with a few astrometric observations over a short time span, (in other words *very short arc* observations).

A considerable amount of literature has been published since then on the issue of optical measurement correlation for objects on Earth-bound orbits. Tommei et al. (2007) applied the admissible region theory to orbits of space debris. Maruskin et al. (2009) and Fujimoto et al. (2014) developed a methodology based on the same principle. Schumacher et al. (2013) used the boundary-value representation to initiate candidate solutions. The individual approaches originate from using different sensors, observation strategies, and assumptions, and consequently each come with advantages and disadvantages. The different methods are categorized and discussed in Chapter 2.

1.4 Outline of the thesis

The thesis is structured as follows. In the upcoming chapter, information about the different existing methods for tracklet correlation and initial orbit determination are presented. Chapter 3 shows the working of the Optimized Boundary Value Initial Orbit Determination (OBVIOD) method, which is used as a baseline for the methods presented in this thesis. This chapter also describes how the Lambert's orbital boundary value problem is solved inside the OBVIOD method. In Chapter 4, a proposed technique called the Shooting method is described and its development is shown along with the challenges faced. Furthermore, an extension of this scheme is shown where improvement attempts were made using different strategies. It also describes the algorithm finally chosen to work along with Shooting method and its advantages over the previous versions of the latter. This chapter ends with a description of the challenges it poses and possible ways to solve them. In Chapter 5, the

results for the different methods are shown. Finally in Chapter 6, conclusions are drawn about the performance and the possible future work is outlined.

2 Initial Orbit Determination

In this chapter, the methods that are applied for tracklet-to-tracklet correlation are discussed. All the algorithms are discussed in their general form.

The discussion for correlation methods starts from the admissible region, which was widely used for various methods, after which, the different tracklet association algorithms are presented. The motivation for using them is described along with the possible improvements.

Admissible region is defined as the set of all physically acceptable orbits that are consistent with the observation of an object. Additional constraints on the object's orbital semimajor axis and eccentricity can be used to further constrain the admissible region.

2.1 Admissible Region

2.1.1 Origin of the concept

The admissible region approach has been previously used in the asteroid tracking community for identification of asteroids based on very short arc observations. The admissible region consists of all the points in space where the true particle can possibly be found. For this reason sometimes it is also referred to as the uncertainty surface. Specifically, Milani et al. (2004) referred to it as a region in the plane of possible range and range-rate values, for which a given line-of-sight observation produces an orbit solution that satisfies certain criteria. This concept has been extended in the SSA community in order to track space objects in Earth bound orbits. In the context of Earth orbiting objects admissible region is determined by restricting all possible orbit solutions to the stable ones around the Earth.

In Milani et al. (2004) the admissible region is mentioned in the context of asteroid discovery. There are various conditions that should be met by the object discovered. These conditions originate from the orbit of the object, its close transfer in the region around the Earth, and its position in the solar system. The conditions are investigated and an admissible region following all the physical constraints is chosen. This is followed by the sampling of the admissible region with a finite, and not too large, subset of points. In order to sample, the authors defined an algorithm to triangulate the admissible region. Among all possible triangulations of a domain, there is a well-known construction, called the Delaunay triangulation, see Bern and Eppstein (1992).

A Delaunay triangulation has a number of optimal properties, e.g. it is the triangulation with the largest minimum angle (among all the triangles). There is an efficient algorithm to compute a Delaunay triangulation, starting from a finite sampling of the boundary. Thanks to the explicit analytic description of the admissible region one can sample the boundary with approximately uniform distances and compute a Delaunay triangulation with the given nodes on the boundary. The nodes of the triangulation give a sample, the edges joining them and the triangles an additional structure. Several points on the boundary are selected which produce an initial triangulation using these boundary points as nodes. Then the nodes

inside the admissible region are added and the edges are changed to achieve the triangulation (Milani and Knezevic, 2005).

In the first example of how to use the admissible region and its triangulation, Milani et al. (2004) discuss the generation of ephemerides. If the orbit of an object has been determined according to the least squares principle, the ephemerides at some time t_1 different than the ones at time t are predicted values of the angles α, δ with a confidence region on the celestial sphere. When the available observational data are not enough to compute a full least squares orbit (e.g., if there are only two observations, or if the observed arc is very short), the ephemerides are considered as the set of values for the angles α, δ at time t_1 which is compatible with the data. If one can assume the object satisfies the conditions defining the admissible region, that is, if one can exclude interstellar orbits, satellites of the Earth, and shooting stars, then there is a set of admissible values for α, δ at time t_1 which is, a compact subset of the celestial sphere. The set of admissible values for α, δ is sampled by triangulation. Given a triangulation of the admissible region, computed from the attributable representing the observations available, one can compute the predicted observation at time t_1 for each node of the triangulation. Each node corresponds to a choice of the values of $(\rho, \dot{\rho})$ at the time t, and together with the four components of the attributable (defined in subsection 1.2.3) this provides a set of six initial conditions, that could be used to compute the set of orbital elements at the epoch t.

Further development of the Admissible Region

Spoto et al. (2018) developed an initial orbit computation method (in the domain of asteroids), based on systematic ranging, which is an orbit determination technique that systematically explores a raster in the topocentric range and range-rate space region inside the admissible region (AR). They use two different grids depending on the boundary of the AR. The first grid is larger and less dense, the second one is based on a refinement using the value of the target function at each point in the first grid. Given an attributable, they define the AR as the set of all the possible couples $(\rho, \dot{\rho})$ satisfying the following conditions:

1. The object belongs to the solar system, and it is not a too long period comet. They only consider the objects for which the value of the heliocentric energy is less than $-k^2$ $/(2a_{max})$, where $a_{max} = 100$ au and k = 0.01720209895 is the Gauss' constant.

2. The corresponding object is not a satellite of the Earth, i.e., the orbit of the object has a non-negative geocentric energy when inside the sphere of influence of the Earth, whose radius is

$$R_{SI} = a_{\oplus} \sqrt[3]{\frac{\mu_{\oplus}}{3\mu_{\odot}}} \simeq 0.010044 au. \qquad (2.1)$$

Here $a_{\oplus}$ is semimajor axis of Earth's orbit around Sun, $\mu_{\oplus}$ is gravitational constant of Earth and $\mu_{\odot}$ is gravitational constant of Sun. The AR is a compact set and can have at most two connected components (disjoint regions) in the $(\rho, \dot{\rho})$ space. The AR usually has one component, and the case with two components indicates the possibility for the object to be distant (perihelion $q > 28$ au). The number of components depends on the number of the roots of a polynomial resulting from condition 1 (for more mathematical details see Milani et al. (2004) and Milani and Gronchi (2009)).

$$E_\odot(\rho, \dot{\rho}) = \frac{1}{2}||\dot{\boldsymbol{r}}(\rho, \dot{\rho})||^2 - k^2 \frac{1}{r(\rho)} \qquad (2.2)$$

This polynomial cannot have more than three distinct real positive roots. The AR has two components if there are three roots and one component if there is only one root. It is worth noting that the region defined by condition 2 could contain points with arbitrarily small values of ρ. The boundary of the region given by condition 2 turns out to have two different shapes: it can be formed just by the line of geocentric energy equal to 0 (if it is entirely contained in the region $0 < \rho < R_{SI}$), or by a segment of the straight vertical line $\rho = R_{SI}$ and two arcs of the zero curve of the geocentric energy (for $0 < \rho < R_{SI}$). Given all these conditions, the AR is sampled with a finite number of points.

The AR is sampled in two different ways, depending on the number of connected components and the values of the roots (r_1, r_2 and r_3 in ascending order). The conditions and grids used in the (ρ, $\dot{\rho}$) space are described in Spoto et al. (2018). In particular, they compute a rectangular grid in the range/range-rate space, with range-rate controlled by the AR equations (Milani et al., 2004). Nevertheless, since the AR has a shape dictated by a polynomial equation and it is not a rectangle, the values of the heliocentric energy are checked for each grid point and the ones not satisfying condition 1 are discarded. Orbits not satisfying condition 2 are discarded as well, except while computing the probability for the asteroid to be a satellite of the Earth.

For scanning the AR, the authors first propose creation of manifold of variations (MOV). Given a subset K of the AR, the MOV $\mathcal{M}$ is defined as the set of the points $(\mathcal{A}^*(\boldsymbol{\rho_0}), \boldsymbol{\rho_0})$ such that $\boldsymbol{\rho_0} \in K$ and $\mathcal{A}^*(\boldsymbol{\rho_0})$ is the local minimum of the target function $Q|_{(\rho=\rho_0)}$. In addition, the value of the minimum RMS of the residuals is less than a given threshold. The symbol $\mathcal{A}$ is used for attributable and $\boldsymbol{\rho_0}$ signifies the (ρ, $\dot{\rho}$) space. The target function is defined by:

$$Q(x) = \frac{1}{m}\xi(x)^T W \xi(x), \qquad (2.3)$$

where $x = (\mathcal{A}, \rho)$ are the fit parameters, m is the number of observations used in the least squares fit, ξ is the vector of the observed-computed debiased astrometric residuals, and W is the weight matrix (refer to Spoto et al. (2018) for more details).

At start of systematic ranging, assuming K is the AR, it is scanned with a regular semi-logarithmic or uniform grid. For each sample point $\rho_0 = (\rho, \dot{\rho})$, $\rho = \rho_0$ and $\dot{\rho} = \dot{\rho}_0$ are fixed in the target function, and then $\mathcal{A}^*(\boldsymbol{\rho_0})$ is searched by means of an iterative procedure. If a nominal solution does not exist, a two-step procedure is followed further. The first step is to compute a grid following the conditions in Table 2.1. After a preliminary grid, it is densified further using the minimum and maximum value of ρ and $\dot{\rho}$ among all the values of the points for which the 4-dimension differential correction converges. A score with respect to the first grid is computed. It is defined as the probability of an object to belong to different classes (Near-Earth Object, Distant Object, Main object). The score is used to select the grid for the second step.

If a nominal orbit was obtained by unconstrained differential corrections, starting from a preliminary orbit as first guess, for instance, using the Gauss' method, (Milani and Gronchi, 2009), then the nominal solution can be used as the center of the subset of the MOV one is interested in, and a different procedure can be adopted to scan the AR. In some cases a spider web sampling can be computed in a neighborhood of the nominal solution (Tommei

Roots	AR components	Grid	Sampling in ρ
$r_1 < \sqrt{10}$ au	1	50×50	Unif. in $\log_{10}(\rho)$
$r_1 \geq \sqrt{10}$ au	1	50×50	Unif. in ρ
$r_1 > 0, r_2 > 0, r_3 > 0$	2	100×100	Unif. in ρ

Table 2.1 – Conditions to create a preliminary grid for systematic ranging (Spoto et al., 2018).

et al., 2007). This is obtained by following the level curves of the quadratic approximation of the target function used to minimize the RMS of the observational residuals.

The advantage of the use of the cobweb is that, firstly, it is faster than the systematic ranging, and secondly it is more accurate in the cases for which one has a reliable nominal solution already (Spoto et al., 2018). Fig. 2.1 shows an example of the spider web sampling on the $(\rho, \dot{\rho})$ plane, where ρ^* and $\dot{\rho}^*$ are the range and range-rate values of the nominal solution, v_1 being the eigenvector corresponding to the greatest eigenvalue λ_1.
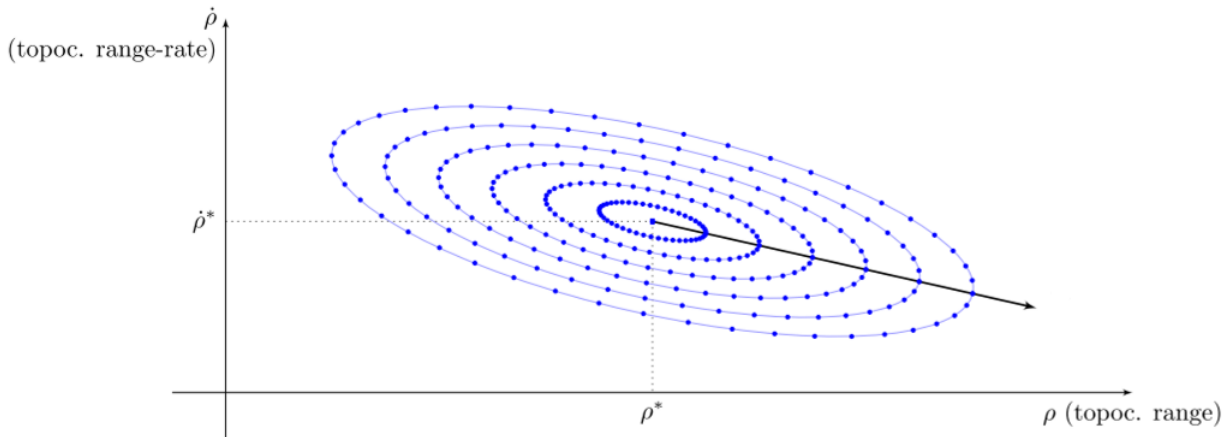
Fig. 2.1 – Example of spider web around the nominal solution $\boldsymbol{\rho^*} = (\rho^*, \dot{\rho}^*)$. The points follow concentric ellipses corresponding to different values of the parameter R for each fixed direction (Spoto et al., 2018).

Orbit determination for asteroids

The first complete mathematical method to convert astrometry into orbits had been established by Gauss (1963). He devised an algorithm to compute a preliminary orbit satisfying three given observations on different nights. When additional observations became available, Gauss proposed to correct the preliminary orbit by solving a least squares problem. This method is now called differential corrections, and this sequence, preliminary orbit followed by least squares, is now the algorithm almost universally used and considered classic. Milani and Knezevic (2005) use the concept of attributable and admissible region to propose a method for orbit determination of asteroids. First, the attributables are computed by fitting the observations of the available very short arcs. The AR is sampled in such a way that there are a finite number of points in the initial conditions space. Those points act as the Virtual Asteroids (VAs), sharing the reality of the object, in the sense that the orbit

through one of them is a good approximation of the orbit of the real object, but one does not know which one. To efficiently sample the admissible region defined above (subsection 2.1.1), Delaunay triangulation is used with the given nodes on the boundary. Then the nodes are selected as points $(\rho_i, \dot{\rho}_i), i = 1, N$ sampling the admissible region, with the sides and the triangles providing an additional geometric structure. The properties defining the Delaunay triangulation are metric ones, thus the nodes selected depend upon the choice of a metric. Different metrics can be used to enhance the resolution in some portions of the admissible region, e.g., when the main goal is to search for either NEO or main-belt asteroids. The set of VAs selected is then

$$X_i = (\alpha, \delta, \dot{\alpha}, \dot{\delta}, \rho_i, \dot{\rho}_i), i = 1, N. \tag{2.4}$$

The set of six coordinates forming the vector $X_i = (\alpha, \delta, \dot{\alpha}, \dot{\delta}, \rho_i, \dot{\rho}_i)$ can be considered as a set of orbital elements. They can be converted into Cartesian position and velocity (topocentric, then heliocentric since the observer's position is well known), as well as into other types of elements, e.g. Keplerian. If these elements are propagated (nonlinearly) to some later epoch t_1, the covariance matrix can be propagated (linearly) to it as well. It is possible to compute the predicted attributable (for observation time t_1) with uncertainty for each node. If another very short arc of observations is available at the second epoch, its attributable with uncertainty can be compared with the predictions for each VA (Milani and Knezevic, 2005).

An algorithm has been defined (Milani et al., 2001) to decide whether two arcs of observations are to be identified to fit together. It is only for the case when an orbit is available (for at least one of the two) with its uncertainty, represented by a covariance matrix. This case of identification is called attribution. Given an attributable, the attribution penalty is defined as a measure of the likelihood that another attributable, computed from an independently detected too short-arc (TSA), actually belongs to the same object. TSA is a small part of the overall orbit such as a couple of minutes arc from a 24-hour orbit. If the attribution penalty is low for some VA, then the two attributables may belong to the same object (Milani and Knezevic, 2005). If this is the case, a preliminary orbit is needed to be used as a first guess to start the differential correction procedure. It was concluded by the authors that the value of attribution penalty threshold to be used in large scale production of TSA linkages can only be dictated by the analysis of the results of large scale tests.

Statistical orbital inversion

Muinonen et al. (2012) also proposed a method different from those based on admissible regions. They first determine, out of tracklets, provisional orbits using a method called Statistical Orbital Ranging (or Inversion). In the latter the orbital element probability density is examined using a Monte Carlo selection of orbits, assuming topocentric ranges for two observations within a tracklet and fitting the remaining ones. Initially, in the paper of 2006 (Muinonen et al., 2006), the authors use the orbits from tracklets at different epochs, calculated with the Ranging method, to compute clouds of geocentric ephemerides at common epochs. To search for the overlapping of these clouds, they use a so-called Phase-space Address Comparison, where every orbit is transformed to a single value, and the procedure is sped up. After this first step, to eliminate the most unlikely linkages, the associations are confirmed using again Orbital Inversion with all observations of the associated track-

lets. Here, to improve the performance, a so-called Stepwise Ranging is used, which adds observations step by step in the inversion procedure, reducing the number of combinations.

Muinonen et al. (2012) proposed a new way based on the Markov Chain Monte Carlo method to solve the orbital inversion problem. The advantage of the statistical orbital inversion method is the better adaptation to the topology of the problem through the Monte Carlo clouds, as well as the applicability to situations where the observations give rise to constrained nonlinear orbital elements probability density functions. Probability density function (pdf) is a function over the sample space, of a continuous random variable from which the probability that the variable is within a certain interval can be obtained. In the case of extensive observational data, the method reduces to sampling a multivariate Gaussian pdf. The downside is also in this case the substantial amount of computing power necessary for the Monte Carlo method.

2.1.2 Application to space debris

Extension of the method used for asteroids to space debris

Tommei et al. (2007) applied the concept of the admissible region in the context of space debris. They show how to apply the methods developed for preliminary orbit determination of heliocentric objects to geocentric objects. They focus on the definition of an admissible region for space debris, both in the case of optical observations and radar observations; then they outline a strategy to perform a full orbit determination.

The data from one TSA cannot allow for the determination of an orbit: e.g. if only two angular observations are available, as in the case of a trail, there are four equations in six unknown orbital elements. Thus it is not possible to solve the orbit determination problem without solving first the identification problem, finding two or more TSA belonging to the same physical object and an orbit fitting all the observations (linkage between two or more TSAs). The above discussion applies to optical observations, but it is possible to formulate a similar problem for radar data.

This problem is computationally complex. The complexity increases sharply with the size of observable population (at least like the square of the number of TSAs). This acts like a limiting factor for the identification problem. If the latter is not solved, the data do not provide orbits for any object. If the identification problem is solved incompletely then a significant fraction of the observational data remain locked in the TSA and have no practical use, apart from an approximate estimate of the population size (Tommei et al., 2007).

The solution proposed by Milani et al. (2004) and Milani and Knezevic (2005) uses the concept of attributable, a four-dimensional quantity defined by two or more observations and synthesizing the useful information from a TSA. The simulations have shown that the problem can be solved for several TSAs of the order of 1 million collected in each night of the survey. The same technique was used for space debris. The definition of the admissible region is modified, taking into account the orbits of the Earth's satellites.

The admissible region for a space debris object observed by a ground-based optical sensor is analytically defined. The admissible region replaces the conventional confidence region as defined in the classical orbit determination procedure. The main requirement is that the geocentric energy of the object is negative, that is the object is a satellite of the Earth.

Let P be the geocentric position of an orbiting space debris D observed at a time t. Then

$$P = P_O + P_D, \qquad (2.5)$$

where P_O is the geocentric position of the observer O and $P_D = \rho \hat{R}$ is the vector in the observation direction (Fig. 2.2).

Let

$$(\rho, \alpha, \delta) \in \mathbb{R}^+ \times [-\pi, \pi) \times (-\pi/2, \pi/2) \qquad (2.6)$$

be the spherical polar coordinates defining the vector P_D.
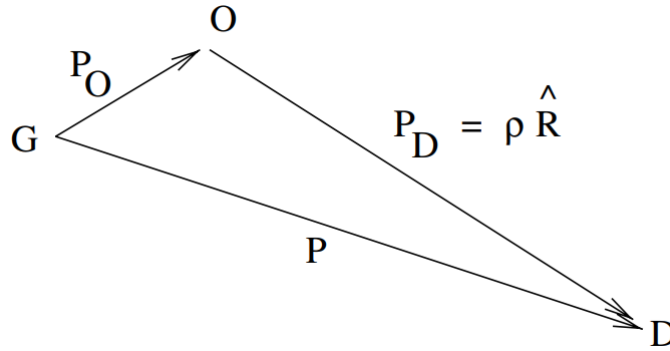
Fig. 2.2 – The space debris D is observed by the point O on the surface of the Earth. The geocenter is denoted by G (Tommei et al., 2007).

As reference system for the polar coordinates, an equatorial one (e.g., J2000) is used, that is α is the right ascension and δ the declination. Since the range ρ and the range rate $\dot{\rho}$ are left undetermined by the attributable, following Milani et al. (2004), Tommei et al. (2007) derive conditions on $(\rho, \dot{\rho})$ under the hypothesis that the object D is a satellite of the Earth. The quantities used are the following:

- Geocentric two-body energy per unit mass of the object

$$E_\oplus(\rho, \dot{\rho}) = \frac{1}{2}\|\dot{P}\|^2 - \frac{\mu_\oplus}{\|P\|}, \qquad (2.7)$$

  where $\mu_\oplus = Gm_\oplus$, $m_\oplus$ is the Earth's mass

- Lower bound for the space debris distance from the position of the observer on the Earth, that is the minimum value of range ($\rho_{\min}$) will be

$$\rho_{\min} = 2r_\oplus \simeq 12756 km, \qquad (2.8)$$

  where $r_\oplus$ is the value of the Earth's radius. We use this bound because we are interested in space debris in high orbits; the objects in lower orbits are usually observed by radar and the admissible region changes.

- Upper bound for the space debris distance from the position of the observer on the Earth, that is the maximum value of range ($\rho_{\max}$) will be

$$\rho_{\max} = 20r_\oplus \simeq 127560 km, \qquad (2.9)$$

(a) **(b)**
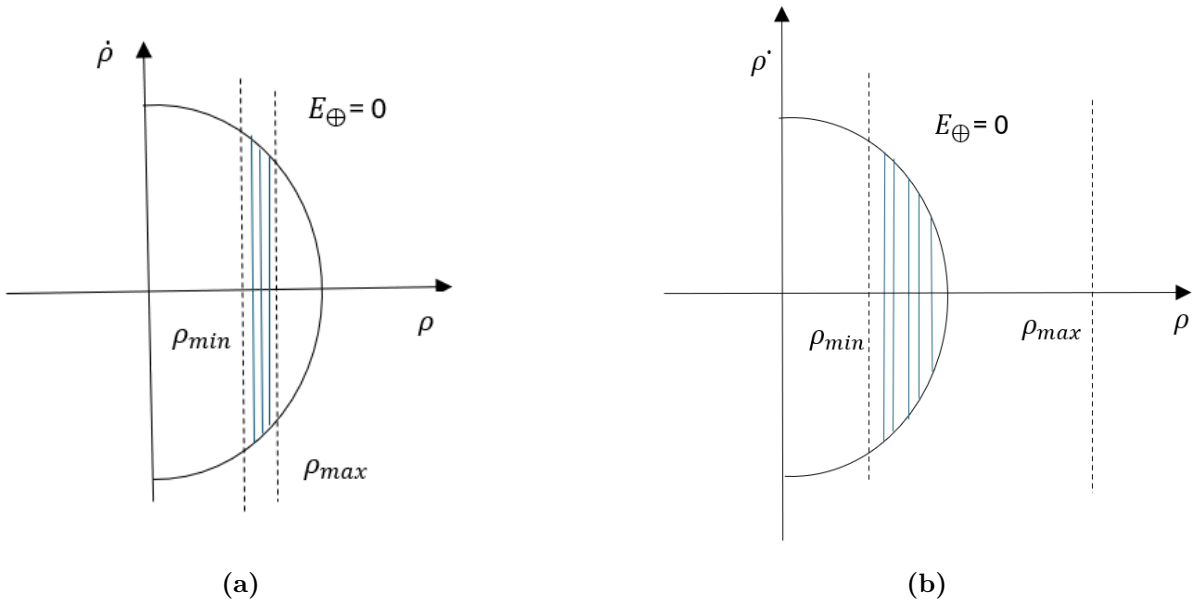
Fig. 2.3 – Admissible region for a space debris D from optical data (one connected component): $E_{\oplus} = 0$ is the curve of zero geocentric energy, $\rho_{\min}$ and $\rho_{\max}$ are the lower and the upper limit for the ranges.

Writing the conditions on $(\rho, \dot{\rho})$ explicitly:

(A) $\mathcal{C}_1 = (\rho, \dot{\rho}) : E_{\oplus} < 0$ ($\mathcal{D}$ is a satellite of the Earth);

(B) $\mathcal{C}_2 = (\rho, \dot{\rho}) : \rho_{\min} < \rho < \rho_{\max}$ (the distance of the object from the observer is in the interval $(\rho_{\min}, \rho_{\max})$).

Given an attributable A_{opt}, the admissible region for a space debris D is defined as the set

$$\mathcal{C} = \mathcal{C}_1 \cap \mathcal{C}_2 \tag{2.10}$$

The condition (B) bounds only the ρ therefore the region $\mathcal{C}_2$ might appear as an infinite stripe in $(\rho, \dot{\rho})$. In order to look for the analytical and geometric description of condition (A) the geocentric position of object $\mathcal{D}$ is used to derive the relation for its geocentric velocity

$$\dot{P} = \dot{P}_O + \dot{\rho}\hat{R} + \rho\dot{\alpha}\hat{R}_\alpha + \rho\dot{\delta}\hat{R}_\delta \tag{2.11}$$

The relation for geocentric position and velocity in terms of polar coordinates is used to expand the geocentric energy equation. The resulting equation is studied by Tommei et al. (2007), Milani et al. (2004) and it was concluded that the region $\mathcal{C}_1$, defined by condition (A), can admit more than one connected component, but it has at most two. The qualitative structure of the confidence region is shown in the figures. Fig. 2.3 shows the case with one connected component: at the left $\rho_{\max}$ is less than the range of the curve $E_{\oplus} = 0$ corresponding to $\dot{\rho} = 0$, while at the right it is greater. Fig. 2.4 shows the case with two connected components: at the left $\rho_{\max}$ is less than the minimum range corresponding to the second connected component of the curve $E_{\oplus} = 0$, while at the right it is greater.

In order to exclude orbits of "just-launched" objects, a third condition was added, on the pericenter $q = a(1 - e)$ (here a is the semimajor axis and e the eccentricity), that is $q > r_{\oplus} + h$, where h could be the height of the atmosphere. But to compute analytically the
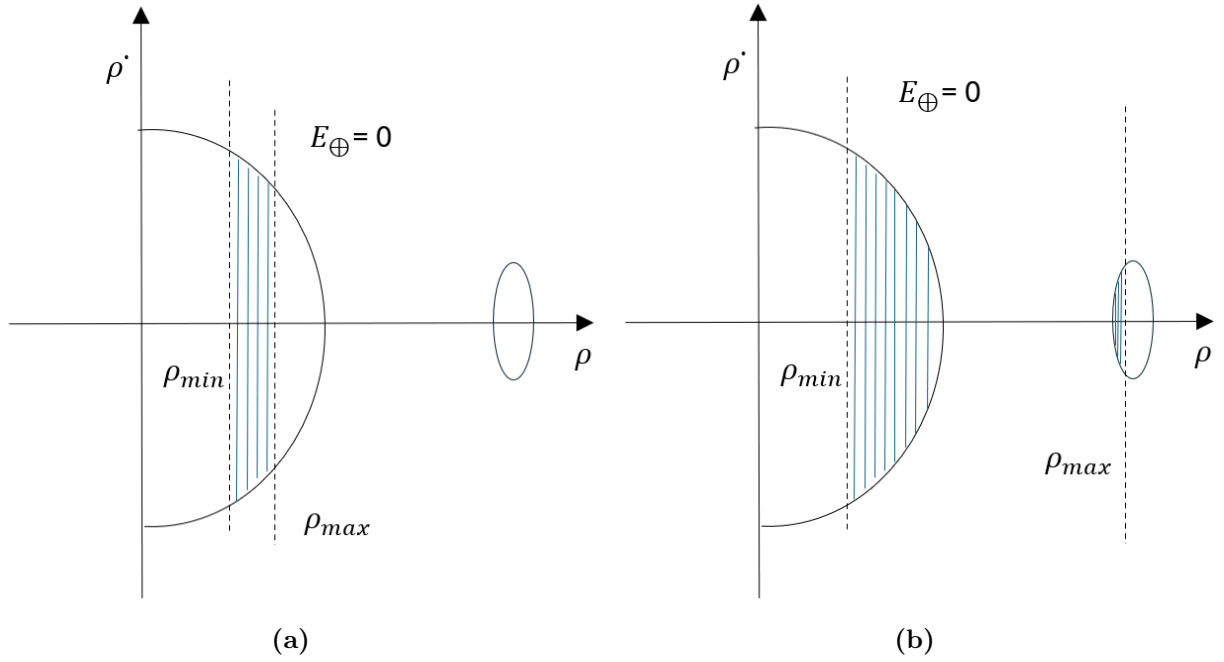
Fig. 2.4 – Admissible region for space debris D from optical data (two connected components): $E_\oplus = 0$ is the curve of zero geocentric energy, $\rho_{\min}$ and $\rho_{\max}$ are the lower and the upper limit for the distance of D from the observer.

corresponding curve in the $(\rho, \dot{\rho})$ plane was deemed to be extremely complicated. However, a restriction on the semimajor axis was made that corresponds to fixing a lower bound for the energy, by replacing condition (A) with

(A') $\mathcal{C}_1 = (\rho, \dot{\rho}) : E_{\oplus min} < E_\oplus < 0$ ($\mathcal{D}$ is a satellite of the Earth and its semimajor axis is greater than a fixed quantity).

Fig. 2.5 shows the resulting admissible region (only the case with one connected component). Milani and Gronchi (2009) however, substitute the condition $q \geq r_\oplus + h$ into the two-body formulae and obtain

$$\sqrt{1 + \frac{2E_\oplus \|\boldsymbol{c}\|^2}{G^2 m_\oplus{}^2}} \leq 1 + \frac{2E_\oplus(r_\oplus + h)}{Gm_\oplus} \tag{2.12}$$

Since the left-hand side is ≥ 0, they impose the condition

$$1 + \frac{2E_\oplus(r_\oplus + h)}{Gm_\oplus} \geq 0 \tag{2.13}$$

on the right-hand side; this is again $a \geq r_\oplus + h$. By squaring Eq. 2.11 one obtains

$$\|\boldsymbol{c}\|^2 \geq 2(r_\oplus + h)(Gm_\oplus + E_\oplus(r_\oplus + h)). \tag{2.14}$$

where c is the angular momentum vector per unit mass expressed in terms of ρ and $\dot{\rho}$ (see Milani and Gronchi (2009)) and $E_\oplus$ can be expressed in the same variables. The Eq. 2.13 is an algebraic inequality in the variables $(\rho, \dot{\rho})$; by another squaring, it is possible to convert it into a polynomial equation of degree 10 in ρ and degree 4 in $\dot{\rho}$. Fig. 2.6 also shows this inner boundary, as well as an alternative outer boundary constraining the apocenter Q at some

large value. The main limitation of this approach is that the authors do not have a rigorous proof that the region defined by $q \geq r_{\oplus} + h$ and $E_{\oplus}(\rho, \dot{\rho}) \leq 0$ has at most two connected components.
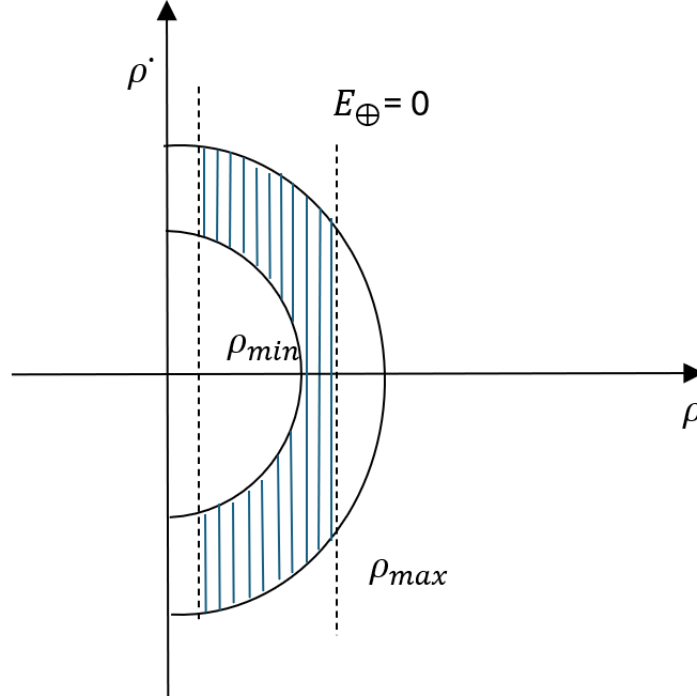
Fig. 2.5 – Admissible region for a space debris D taking into account the condition (A') instead of (A)
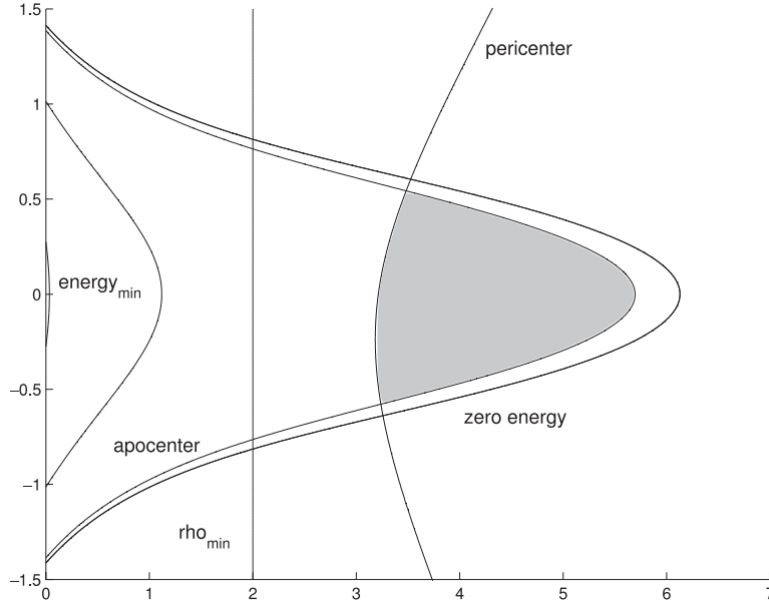
Fig. 2.6 – The admissible region for an Earth satellite must be a subset of the region with negative geocentric energy. Additional constraints may be added by using the physical boundary $\bar{r} = r_{\oplus} + h$ defined by the atmosphere and the dynamical boundary defined by the sphere of influence $r \leq r_{SI} : a \geq \bar{r}, q \geq \bar{r}$ and $Q \leq r_{SI}$ can be used.

The admissible region for space debris is used in the same way as in the asteroid case, to be sampled by a swarm of virtual debris, which is analogous to the virtual asteroids. In this way the linkage problem is transformed into a multiple hypothesis attribution problem (see Milani and Gronchi (2009)). If the Delaunay triangulation method is used, the starting point is a sampling of the boundary of the admissible region. For the outer boundary this is the same as in the asteroid case, for the inner one, either a minimum ρ or a minimum perigee q can be used. The first choice is simpler and leads more easily to a reliable algorithm, because with the second condition one cannot be sure of the number of connected components. A reasonable approach would be to triangulate a region with the simplest inner boundary, then discard the nodes which turn out to have a ballistic orbit with $q < r_\oplus + h$ (Milani and Gronchi, 2009).

Virtual debris particles

The uncertainty surface commonly known as admissible region can be discretized by virtual debris (VD) particles just like the virtual asteriods mentioned in the section above. Each VD particle is an approximation to a possible orbit for the observed particle of space debris. Viewed as a whole, the set of VD particles forms a virtual debris field, or VD field, which approximates the macroscopic uncertainty distribution associated with a given attributable vector.

Maruskin et al. (2009) and Maruskin et al. (2007) did a preliminary numerical analysis of a randomly chosen attributable vector and its corresponding VD field. It showed that before several hours had passed, about half of the VDs will have crashed into the Earth. Motivated by these observations, they presented a tighter restriction on the uncertainty region of the $(\rho, \dot{\rho})$ plane. In addition to demanding the distance between the debris particle and observer lies between 2 and 20 Earth radii at the moment of observation, additional restrictions were placed on the periapsis and apoapsis of the orbit. In particular, the orbit's periapsis is required to be greater than 1 Earth radius plus 200 km, and the apoapsis to be less than 25 Earth radii. This places additional constraints on the admissible region and reduces its size considerably. The admissible region is mapped into the Delaunay space and later used to construct an algorithm for computing an orbit correlation, the procedure is briefly described in section 2.2.

Bayesian admissible region

Fujimoto and Scheeres (2012) propose a technique of correlating multiple optical observations by means of probability distributions defined by the admissible region expressed in Poincaré orbit element space. They propose a transformation of the VD particles from topocentric spherical coordinates into Poincaré variables. The latter are the non-singular canonical counterpart to the equinoctial orbit elements. The exact transformation is performed in several steps. First, from topocentric spherical coordinates to geocentric Cartesian coordinates and then to orbital elements. Finally, the orbital elements are transformed to Poincaré variables. The map of the admissible region is a two-dimensional bounded submanifold, or a disk, in six-dimensional Poincaré space. If two such distributions are propagated to a common epoch, their intersection would mean that the two optical observations for which the AR was defined, belong to the same object.

Multiple hypothesis search

DeMars and Jah (2013) consider the space of range and range-rate to define the admissible region. The angular positions and rates are considered to be available following the concept of attributable defined above. The position of the object with respect to the planet center is given as the sum of the position of the ground station and the position of the object with respect to the station, and likewise for the velocities. The position and the velocity of object with respect to the station is given in the spherical coordinates of range ρ, right ascension α, declination δ, and their time rates of change, such that

$$\boldsymbol{r}^i_{\text{obj}} = \rho \boldsymbol{u}_\rho,$$
$$\boldsymbol{v}^i_{\text{obj}} = \dot{\rho} \boldsymbol{u}_\rho + \rho \dot{\alpha} \boldsymbol{u}_\alpha + \rho \dot{\delta} \boldsymbol{u}_\delta \tag{2.15}$$

where the unit vectors of $\boldsymbol{u}_\rho$, $\boldsymbol{u}_\alpha$, and $\boldsymbol{u}_\delta$ are given in terms of the angles α and δ.

The parameters in Eq.2.14 are inserted in the two-body energy equation, along with the ground station's position r_{sta} and velocity v_{sta} allowing it to be expressed as:

$$2E = \dot{\rho}^2 + 2 v_{sta} \boldsymbol{u}_\rho \dot{\rho} + f(\rho) \tag{2.16}$$

where $f(\rho)$ is expressed in terms of $\alpha, \dot{\alpha}, \delta, \dot{\delta}, r_{sta}, v_{sta}, \rho$ and μ. The above equation is a quadratic in $\dot{\rho}$, given the angular positions and rates. It can be solved for the range-rate for values of range starting at zero and increasing. Setting the energy equal to zero, yields a region of range and range-rate values which are admissible, that is the zero-energy curve that is produced describes a bound on the set of all elliptic Earth-bound orbits. This region then fully describes the possible combinations of range and range-rate which permit the object to be in an elliptic orbit about the Earth. Carrying out the calculations yields the region as shown in Fig. 2.7. Constraint is added on range to further reduce the combinations of range/range-rate pairs that lead to possible orbit solutions. This type of constraint manifests as a line of constant range spanning the values of range-rate. In Fig. 2.8 minimum and maximum range conditions (ρ_{min} and ρ_{max}, respectively) were added on top of the unconstrained admissible region from Fig. 2.7. Thus, the possible range/range-rate pairs must not only lie within the admissible region, but must also lie between the minimum and maximum range values. One additional constraint related to semimajor axis, or equivalently energy was added. By allowing for a minimum and maximum semimajor axis, minimum and maximum energy values could be determined.

These energy values were then used to generate two additional curves (in addition to the zero-energy curve previously discussed) relating to range and range-rate. These curves are illustrated in Fig. 2.8 and labeled with a_{min} and a_{max}. Therefore, the possible range/range-rate pairs must lie between the curves specified by the semimajor axis (energy) constraints and between the bounds on the range, specified by ρ_{min} and ρ_{max}. The admissible region is interpreted probabilistically, and an equivalent Gaussian mixture representation is developed in order to apply a Gaussian mixture estimation algorithm to the problem of IOD. The general methodology for developing the Gaussian mixture representation is based on the observation that, given the admissible region and no additional information, no single combination of range and range rate can be said to be more probable than any other combination. In probabilistic terms, this means that the admissible region can be described by a two-dimensional (2-D) uniform distribution. The authors developed a method by which
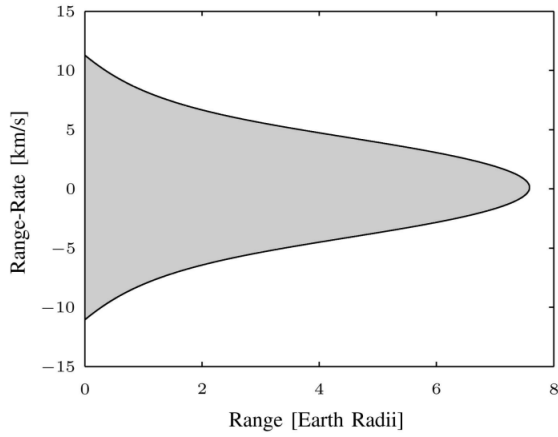
Fig. 2.7 – Region of admissible combinations of range and range-rate which permit Earth orbiting object. (DeMars and Jah, 2013)
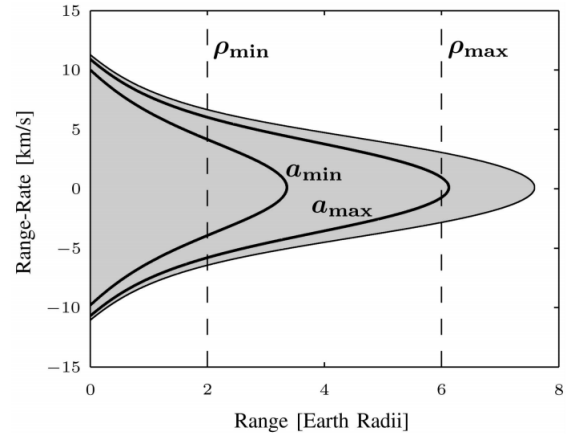
Fig. 2.8 – Region of admissible combinations of range and range-rate subject to semimajor axis and range constraints. (DeMars and Jah, 2013)

a univariate uniform distribution can be approximated by a Gaussian mixture probability density function (PDF) and applied it to the admissible region in order to formulate a probabilistic IOD solution.

Extension of Bayesian admissible region approach

Fujimoto et al. (2014) define the AR as a probability density function (pdf) constrained in the range ρ and range-rate $\dot{\rho}$ directions via a few physical criteria such as that the orbit is elliptic, the object's range is within the sensing capabilities, and so on. Probability density function is a function that provides the likelihood that the value of a random variable will fall between a certain range of values. The angle and angle-rate, nominally in right ascension α and declination δ, at the epoch of a tracklet are estimated via a least-squares fit of the tracklet data to a polynomial model in time. These variables plus necessary parameters, such as the latitude ϕ and longitude Θ of the observation point, are referred to collectively as the attributable vector (Maruskin et al., 2009). Thus, each point on the AR combined with the attributable vector corresponds one-to-one with a state that the observed object may have taken. Furthermore, the covariance from the least-squares fit may be incorporated in the AR to represent observational errors. The admissible region is a uniform probability density function (pdf) whose support is a compact set. Multiple ARs may be propagated to a common epoch and an a posteriori pdf computed based on Bayes' rule.

Suppose that, given some set of criteria $\mathcal{C}$, A is a compact set in state space $\mathcal{X}$ that meets $\mathcal{C}$. Then, the AR $F_C[\boldsymbol{X}(t^0); Y^0]$ is a pdf over $\mathcal{X}$ assigned to an attributable vector $\mathcal{A}$ such that the probability p that the observed object exists in region $B \subset A$ at time t^0 is

$$p[\boldsymbol{X}(t^0)] = \int_B (F_{\mathcal{C}}[\boldsymbol{X}(t^0); \mathcal{A}^0] \, dX^0{}_1 dX^0{}_2 ... dX^0{}_n) \tag{2.17}$$

where $\boldsymbol{X}(t^0) \in \mathcal{X}$ and

$$\boldsymbol{X}(t^i) \equiv \boldsymbol{X}^i = (X^i{}_1 X^i{}_2 ... X^i{}_n). \tag{2.18}$$

Note that Fujimoto et al. (2014) impose $\int_A F_{\mathcal{C}}[\boldsymbol{X}(t^0); \mathcal{A}^0] dX^0 = 1$. Fig. 2.9 is an example of an AR, refer to their paper to see the criteria $\mathcal{C}$. These criteria ensure that the AR encompasses most trackable object relevant to SSA while simultaneously filtering out highly eccentric orbits. Note that changing $\mathcal{C}$ allows one to be explicit about the types of orbits that are included in the analysis. For example, if the observer is only interested in identifying objects in and near the GEO belt, $\mathcal{C}$ may be modified accordingly.

It is important to add the observational errors for this methodology otherwise two potential difficulties are anticipated with the assumption that these errors are small enough to be ignored. The first is that the zero-error assumption causes missed associations especially when the state space discretization is refined. The second is the ambiguity in the number of revolutions the observed object potentially made between two tracklet pairs leads to a large number of associations. The addition of observational errors would make the AR, in principle, 6-dimensional. Fujimoto and Scheeres (2012) showed that the uncertainty in the attributable vector has a small effect on the discretized admissible region map and that the 2-D assumption is justified for several days but only if the discretization of the state space is coarse ($\sim$100 km resolution in semimajor axis, $\sim$ 5 in mean anomaly). Fujimoto et al. (2014) investigate how appropriate the 2-D assumption is for finer state space discretizations. Gaussian observation errors of $\sigma = 2$ arcsec in both α and δ are considered up to 3σ. It was found that ignoring these errors may not be justified for fine discretizations of the state space. The Bayesian and least-squares estimator hybrid approach for association is explained in the next section.
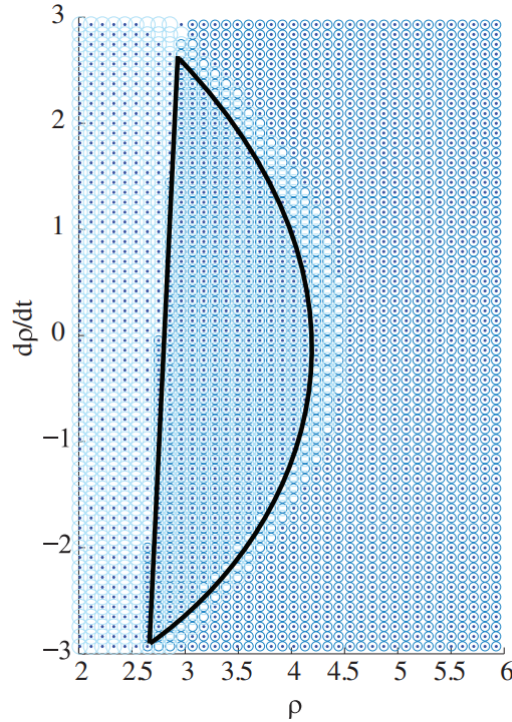
Fig. 2.9 – An admissible region for attributable vector $\mathcal{Y} = (\alpha, \delta, \dot{\alpha}, \dot{\delta}, \phi, \Theta)$

2.2 Tracklet Correlation

As mentioned earlier, the tracklets contain incomplete state information and cannot be used alone to calculate an orbital solution. Hence, they are correlated against other tracklets, i.e. tested if they belong to a common object. After a successful association, the tracklet pairs provide enough information to determine the full orbital state. In the past years, different methodologies to perform this association and initial orbit determination have been developed. Due to the incomplete state information from a tracklet, many research studies make a hypothesis over unknown variables and carry out a search in their predefined admissible region of interest. The previous section described how some of the researchers defined the admissible regions. The next step is the association of tracklets and initial orbit determination. The following section will briefly summarize the different types of tracklet association techniques in the context of earth-orbiting space objects.

2.2.1 Approximation using an initial circular orbit

The AIUB has been conducting several search campaigns for space debris in the GEO region for ESA. During these surveys a substantial population of unknown, small-sized objects was found (Schildknecht et al., 2001). Musci et al. ('Orbit improvement for GEO objects using follow-up observations') propose determination of circular orbits for all the objects using the discovery observations. The period between the first and the last observation of an object (from now on called 'observation arc') lies between 30 s and 3 min. If only two observations are available, only four of the six Keplerian elements can be determined. For objects in GEO a circular orbit was considered to be a good approximation of the true orbit (see section 1.2.2). Thus the eccentricity is e = 0 and the argument of perigee ω may be selected arbitrarily. The orbit parameters are determined with the method of least squares for three and more observations. After the initial orbit determination of a circular orbit a general orbit improvement process is involved using all observations if follow-up observations are available. They showed that two follow-up observation sequences during the same night are necessary and sufficient for a successful recovery of newly detected GEO objects after a few nights. The resulting improved elliptical orbits represent the "true" orbits with sufficient accuracy. The arc covered by all observations should, however, be long enough (a few hours). The actual length depends somewhat on the eccentricity. A "secure" orbit can be determined based on an observation arc of a few days. Such orbits may be used to build up a catalogue.

2.2.2 Mapping object's state into Delaunay elements

Maruskin et al. (2009) extract the maximum amount of usable information from a single tracklet of a space object and also bound the possible domain of the unmeasured state components. They use this information to correlate one observation tracklet with another from a previous observation to detect whether the two objects are the same. The idea is to use the multiple angular measurements to develop an improved estimate of the angular location of the object and the angular rate of the object, and then use these measurements to constrain the unmeasured states of the object. This approach was also proposed in (Tommei et al., 2007); (Milani and Knezevic, 2005) and it is further extended in the research of Maruskin et al. (2009). There is not enough information in a tracklet to provide an accurate orbit. To capture this additional information, Maruskin et al. (2009) estimate the space

object's angular location, angular rate, and angular acceleration at a fixed epoch, chosen within the tracking pass. This approach recognizes that there is little information in one tracklet related to the object range and range rate, and concentrates on fixing the angles, angle rates, and angle accelerations to a higher level of precision. The concept for admissible region used is briefly described in section 2.1.2.

Given two extended attributable vectors $\mathcal{A}_1$ and $\mathcal{A}_2$ one determines the corresponding admissible regions $\mathcal{C}_1$ and $\mathcal{C}_2$, respectively. These admissible regions cannot be compared directly, as they are subsets of two different sets of topocentric spherical coordinates, affixed to the Earth at different locations and different times. The admissible region is pushed forward to Delaunay Space and both the uncertainty distributions are dynamically evolved or regressed in time to a common epoch t so that $F_{\mathcal{A}}^t \mathcal{C}_1$ and $F_{\mathcal{A}}^t \mathcal{C}_2$ are both two dimensional sub manifolds of six dimensional Delaunay space, dynamically mapped to a common epoch. If $\mathcal{A}_1$ and $\mathcal{A}_2$ correspond to the same object, then $F_{\mathcal{A}}^t \mathcal{C}_1$ and $F_{\mathcal{A}}^t \mathcal{C}_2$ must necessarily intersect. Because $\mathcal{A}_1$ and $\mathcal{A}_2$ each contain four pieces of information (two angles and two angle rates), the system is overdetermined. Unless there is some redundancy in the information, if both tracks correspond to the same physical object, it is likely that the uncertainty manifolds $F_{\mathcal{A}}^t \mathcal{C}_1$ and $F_{\mathcal{A}}^t \mathcal{C}_2$ will intersect at a single point.

To obtain the unique intersection point, they use an algorithm called Intersection Theory Analysis (ITA) (Maruskin et al., 2009). They test this algorithm on different types of observations.

2.2.3 Correlation using probability distributions

The direct Bayesian admissible region approach proposed by Fujimoto and Scheeres (2012) is an a priori state free measurement association and IOD technique. The technique consists of correlating multiple optical observations by means of probability distributions defined by the admissible region expressed in Poincaré orbit element space. If the correlation process results in a positive result, an initial estimate for the orbit is immediately obtained. First, the admissible region, as well as other necessary concepts, are introduced and defined mathematically (see section 2.1.2). One of the goals of this work was to know the probability of an optically observed object, characterized through the attributable vector A, being in the vicinity of some coordinate X in a standard comparison space such as the Poincaré orbit element space. This probability could be calculated for various values of X across the comparison space, so it is thought of as an element of a probability density function (pdf). However the attributable vector contains only four variables $(\alpha, \delta, \dot{\alpha}, \dot{\delta})$ regarding object's position and velocity. Therefore, it is necessary to combine multiple observations of the object. It is also important to know whether some incoming data, such as new observation, are related with the aforementioned pdf, and if so how it affects the pdf.

They use data sets S_1 and S_2 regarding Earth-orbiting objects and their observations. Set S_1 contains past observation data and debris distribution models. S_1 is used as a background pdf that filters out unrealistic solutions. Set $S_2(A)$ contains the distribution of Virtual Particles (analogous to Virtual Debris in section 2.1.2) over the standard comparison space. S_2 is used to represent the information from each observation. Very large number of Virtual Particles (VPs) are mapped nonlinearly to completely represent the admissible region in 6-D space.

Although VPs are, by definition, uniformly distributed in the admissible region (i.e.,

range/range-rate space) for common choices of the comparison space, such as orbit element and Poincaré spaces, the distribution of VPs in such spaces is non-uniform, due to the nonlinearity of the mapping of the AR. As a consequence, certain values of X become more likely than others. The data in this category are continuous and are a function of A. Computationally, however, a large and discrete sample set ($\tilde{S}_2$) is used instead.

The standard comparison space is discretized into six-dimensional hypercubes (or "bins"), indexed with vector $\boldsymbol{i}$. By doing so, TLE objects, modeled debris, and VPs with similar orbital characteristics are grouped together. In the discretized comparison space, objects in a particular bin are spatially indistinguishable, i.e. their coordinates are treated as being the same as those that define the position of the bin. The discretization makes up for deficiencies in S_1 data, undersampling of $\tilde{S}_2$, and any additional uncertainty due to observation and modeling error, and it speeds up computational turnaround. The precision of the method is limited by these deficiencies and uncertainties as well as multi-revolution solutions (Fujimoto and Scheeres, 2012).

With discretization the data in S_1 and S_2 are considered discrete pdfs spanning the comparison space. These pdfs are referred to as $s_1(\boldsymbol{i})$ and $s_2(\boldsymbol{i}, A)$, respectively (both are mapped to bin $\boldsymbol{i}$). Suppose that there exists some prior discrete pdf $g_O(\boldsymbol{i}, \tau)$ that describes the probability that a particular object of interest O is consistent with bin $\boldsymbol{i}$ at epoch τ. That is, if P is a probability measure and $E_O(\boldsymbol{i}, \tau)$ is an event where O is consistent with $\boldsymbol{i}$ at time τ, then

$$P[E_O(\boldsymbol{i}, \tau)] = g_O(\boldsymbol{i}, \tau). \tag{2.19}$$

g can originate from the TLE catalog or a debris distribution model (S_1), one observation or a set of observations that are believed to be correlated a priori with $O(S_2)$, or any combination of S_1 and S_2. Here, $\boldsymbol{i}$ is treated as a random variable that spans the bin index space. All elements have been propagated to τ.

Considering a new series of information $\{r\}$ from S_1 or S_2, such as uncorrelated observations, the aim is to calculate a posterior pdf $h_O(\boldsymbol{i}, \tau)$ on whether O is consistent with bin $\boldsymbol{i}$ and is related to $\{r\}$. If the new information does not regard O, $h_O(\boldsymbol{i}, \tau) = 0$. Let $f_{\{r\}}(\boldsymbol{i}, \tau)$ be the pdf that describes the probability that $\{r\}$ is consistent with bin $\boldsymbol{i}$ and event x_r^O be one where the series $\{r\}$ is related with O. The latter event is added as a condition to h, using Bayes's theorem the posterior pdf is,

$$P[E_{\{O\}}(\boldsymbol{i}, \tau)|x_r^O] = \frac{f_{\{r\}}(\boldsymbol{i}, \tau)g_O(\boldsymbol{i}, \tau)}{\sum f_{\{r\}}(\boldsymbol{j}, \tau)g_O(\boldsymbol{j}, \tau)} \tag{2.20}$$

where the sum in the denominator is over all bins. In a graphical sense, pdf h is a cutout of the region where f and g intersect; $h > 0$ for any bins where both $f > 0$ and $g > 0$, and the probability expressed by h is one that is evaluated over this overlap region. Based on map of admissible region into Poincaré space, one can look at whether $h > 0$ for some bin $\boldsymbol{i}$ to deduce with confidence whether or not the new information is related to the object of interest.

The method proposed here however, requires mapping a large number of VPs from $\rho/\dot{\rho}$ space to, say, Poincaré space to ensure accuracy. Attempting to exactly map these points can be computationally expensive. A way to linearize this problem was shown, in the linear method. A smaller sample of S_2 which is defined as $\tilde{S}_2$ is used and only these points are mapped exactly. Again, $\tilde{S}_2$, is uniform over $(\rho, \dot{\rho})$ space. Consider one element of $\tilde{S}_2$ located

at $(\rho^*, \dot{\rho}^*)$ in $(\rho, \dot{\rho})$ space and X^* in the comparison space. Then, to first-order accuracy, some point $(\rho, \dot{\rho})$ in the vicinity of $(\rho^*, \dot{\rho}^*)$ is mapped to comparison space as

$$X = X^* + \delta X \approx X^* + \Phi(\delta\rho, \delta\dot{\rho}) \tag{2.21}$$

In Eq. (2.21), δ denotes a small deviation and Φ is the linear map from $(\rho, \dot{\rho})$ to comparison space.
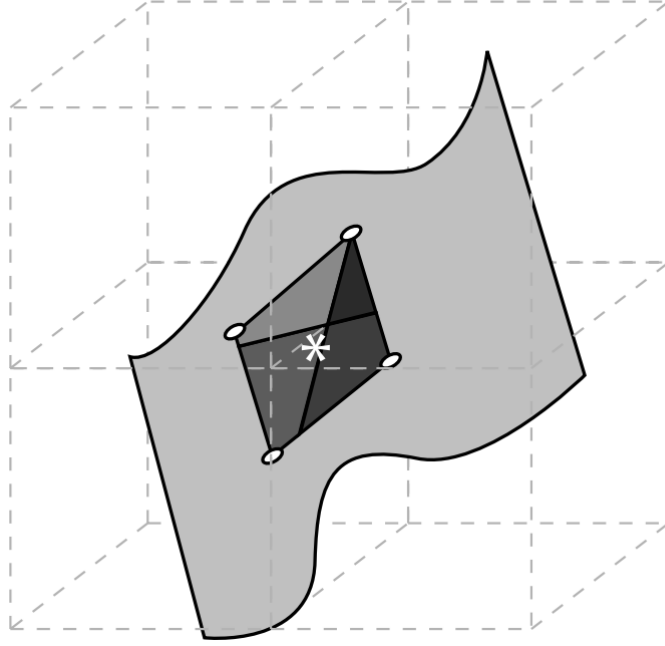
Fig. 2.10 – Three-dimensional representation of the linear mapping process. The dashed lines represent the boundaries of the bins. The curved surface is the admissible-region map, and the small sectioned plane is a portion of the admissible region mapped to comparison space about the asterisk. The plane cuts through four bins; sections belonging to different bins are distinguished by the shading.

The algorithm based on the concept described above, determines the bins that one linear map of a bounded region in the admissible region fills. Fig. 2.10 is a diagram of the direct map of the admissible region, the linear map of a segment of it, and the bin structure in 3-D space. The linear map will remain a two-dimensional plane in the full six-dimensional problem. The goal now is to find how much the linear map fills each bin that it cuts through: that is, to solve for the area that the linear map occupies in each bin. Taking equal area regions in the admissible regions, all linear maps contain the same number of VPs. Therefore, regardless of the total area of the linear map, the area of a segment of it is directly proportional to how many VPs are contained in the segment. The total VP density in a particular bin is the sum of the areas of all linear map segments that reside in it. The VP density distribution, or equivalently, the probability distribution function is found by normalizing these sums over all bins.

The true state is included in the region in state space where $h > 0$. Therefore, the state estimate is good. On the other hand, when two observations are of different objects, $h = 0$ for the entire state space, which allows one to conclude that the two observations are unrelated. An implementation of the method in MATLAB successfully correlated 996 optical

observations and provided good initial orbit estimates. Observation errors were deemed to have a small effect on the accuracy of the correlation procedure. However, two limiting cases were examined: one where orbit estimation accuracy is compromised if the time between observations is short and another where false correlations may occur if objects in a satellite constellation are observed.

2.2.4 Correlation using Bayesian and Least Squares hybrid approach

Fujimoto et al. (2014) propose a hybrid approach that takes the tracklet association and initial orbit determination results of the probability distribution method defined in the section above and passes them to a least squares estimator. The least squares step ensures good estimate precision without having to use a fine discretization of the state space, minimizing negative effects of measurement error on tracklet association using ARs. Suppose that for n pairs of samples $y_1, \ldots, y_n$ each associated respectively to independent variables $x_1, \ldots, x_n$, the samples are modeled with a simple linear regression model as

$$\hat{y}_i = \hat{\beta}_0 + \hat{\beta}_1 x_i, \tag{2.22}$$

for all integers $1 \leq i \leq n$, where the hat symbolizes that it is a model estimate. Then, for the hypothesis test regarding slope parameter β_1

$$\begin{cases} H_0 : \beta_1 = 0 \\ H_1 : \beta_1 \neq 0, \end{cases} \tag{2.23}$$

where H_0 is the null and H_1 the alternative hypothesis, the probability of falsely rejecting H_0 is set to be p_{min}. Through this step, a maximum bound is effectively set for β_1 itself, meaning the residuals must be unrelated to time in a linear sense for a tracklet pair to be associated with a state estimate.

First, the time history of right ascension and declination must be converted into an attributable vector at the tracklet epoch; i.e. a single set of angles and angle-rates. The measured angles are fit to a polynomial kinematic model in time, such as for the right ascension

$$\alpha(t) = \alpha^0 + \dot{\alpha}^0(t - t_0) + \frac{1}{2}\ddot{\alpha}^0(t - t^0)^2, \tag{2.24}$$

where superscript 0 denotes the state at the tracklet epoch. Next, admissible regions are computed for each attributable vector in the Poincaré orbit element space. As discussed in (Fujimoto and Scheeres, 2012), the admissible region is divided into subsets (units of discretization in the range-direction × units in the range-rate) and each subset linearly extrapolated. The Poincaré space, and consequently the ARs, are discretized. The admissible regions are propagated to a common epoch, which is chosen to be the tracklet epoch of the first tracklet, under two-body dynamics. The correlation takes place as described in the section above, the least square filters are run. The reference state of each filter is the centroid of the bin where $h > 0$. For the filter to converge, the RMS of the (observed - computed) residuals for both the right ascension and declination over all tracklets processed should be less than some maximum.

2.2.5 Admissible region bounds for track initiation

Schumacher et al. (2013) propose a type of admissible-region analysis for track initiation in multi-satellite problems when angles are the primary observable. For a specified rectangular partition in the space of orbital elements, they present explicit upper and lower bounds, and other constraints, for the values of range and range rate that will lead to initial orbit hypotheses (data association hypotheses) associated with that partition.

Given a pair of line-of-sight unit position vectors u_i and u_j, measured at time t_i at station position R_i and time t_j at station position R_j, respectively, the aim is to test the hypothesis that these two observations are associated with the same space object. The authors attach a set of hypothetical range values, $\{\rho_{i,m}, m = 1, 2, ...\}$ and $\{\rho_{j,n}, n = 1, 2, ...\}$, respectively to each of these measured unit vectors, then generate candidate orbits by solving Lambert's problem for each of the pair-wise combinations of hypothetical orbital position vectors $r_{i,m} = R_i + \rho_{i,m} u_i$ and $r_{j,n} = R_j + \rho_{j,n} u_j$. In principle one can consider all possible pairs of observations and solve the family of Lambert problems for each pair. Then each hypothetical orbit from the solution of Lambert's problem is a data association hypothesis that must be either confirmed or eliminated through comparisons with other observational data.

In order to limit the range hypotheses, the authors only seek to generate the hypotheses for the orbits that lie in a bounded region of semimajor axis element a, eccentricity e, inclination I and right ascension of ascending node Ω, namely, within a partition of the element space by the intervals $[a_{min}, a_{max}]$, $[e_{min}, e_{min}]$, $[I_{min}, I_{max}]$ $[\Omega_{min}, \Omega_{max}]$. By constructing upper and lower bounds on range for each measured line of sight for each partition of the element space, one limits the number of range hypotheses that have to be considered for each partition. This approach allows one to consider a manageable number of range hypotheses for each partition, simply by making the partitions small enough.

The authors also use the minimum eccentricity and minimum semimajor axis solutions of the Lambert's problem to restrict the ranges. The eccentricity of the orbit of least possible eccentricity that goes through a given pair of position vectors can be computed solely in terms of those position vectors (Prussing and Conway, 1993).

$$0 \leq e_0 = \frac{|(||r_1|| - ||r_2||)|}{||r_2 - r_1||} \leq 1 \tag{2.25}$$

Likewise, semimajor axis of the orbit of least possible semimajor axis that goes through the pair of positions can be computed solely in terms of the position vectors. If $a_0 > a_{max}$ or $e_0 > e_{max}$, then reject the range hypothesis pair without solving Lambert's problem.

$$4a_0 = ||r_1|| + ||r_2|| + ||r_2 - r_1|| \tag{2.26}$$

In case the observations include, or allow one to derive angle rates, one can deduce additional bounds on the possible values of the range. Most importantly, with an accurate angle rate, the track initiation job scales linearly with the number of observations rather than the square or cube of the number of observations. The problem also scales linearly in the number of range hypotheses as well as in the number of range rate hypotheses. One could hardly expect to do any better than this in solving a large track-initiation problem using optical data (Schumacher et al., 2013).

$$\frac{\mu}{a_{max}} \left(\frac{1 - e_{max}}{1 + e_{max}} \right) \leq ||\dot{r}||^2 \leq \frac{\mu}{a_{min}} \left(\frac{1 + e_{max}}{1 - e_{max}} \right) \tag{2.27}$$
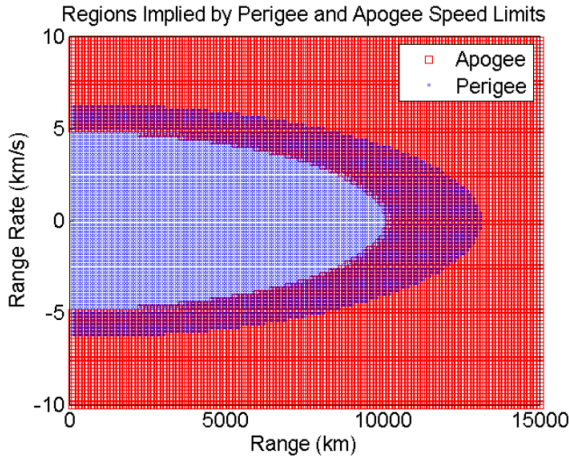
Fig. 2.11 – Overlapping range-range rate allowable regions.
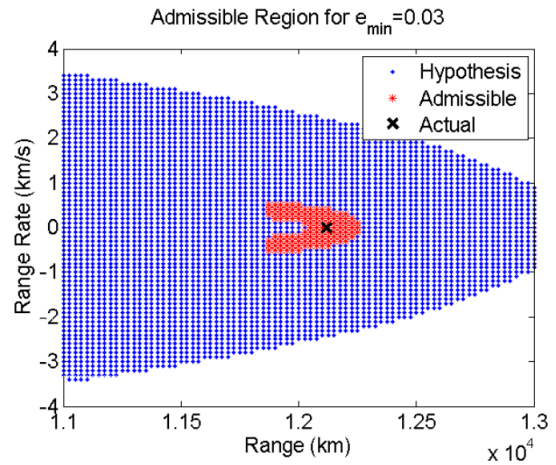
Fig. 2.12 – Admissible region with $e_{min} = 0.03$.

The maximum perigee velocity and minimum apogee velocity inequalities produce regions in the range-range rate plane which satisfy the selected partition of semimajor axis and eccentricity for the given angle and angle rate observation. The velocity magnitude is required to be between the maximum perigee speed and minimum apogee speed. The region in $(\rho, \dot{\rho})$ plane implied by these inequalities is shown in Fig. 2.11. It should be noted that the perigee condition is satisfied within an elliptical region whereas the apogee condition is satisfied outside a similar region. If a given observation was to form a pair of regions which had no overlap, then that observation would not lie within the selected element partition and could be eliminated from consideration. An example of admissible region is shown in Fig. 2.12, it explicitly reflects the e_{min} constraint.

Because the bounds are conservative to some extent and not exact, some values of range and range rate that lie within the bounds given here will lead to candidate orbits that lie outside the specified partition of the element space. This fact leads to some inefficiency in the parallelization of the initial orbit hypotheses over the whole element space. Essentially, nearly duplicated candidate orbits may be generated near the boundaries of the specified partitions and would therefore have to be identified and merged later in the tracking process. Although the detection and merging of duplicate tracks must always be done in any multiple-hypothesis tracking implementation, the inefficiency of the range and range rate bounds necessarily increases the size of that task. The actual cost of this inefficiency in particular problems will depend on the observation sets, the element partitions of interest and the range / range-rate sampling strategy, and may need to be studied if the scenario is computationally stressing. On the other hand, all the orbits within an element-space partition correspond to values of range and range rate that do lie within the bounds given here, so that no candidate orbits will be missed merely through this choice of bounds.

2.2.6 Statistical Ranging

A new orbit determination method, the statistical ranging was presented by Virtanen et al. (2001), which is applicable to poorly observed single-apparition asteroids having two or more observations. A Monte Carlo technique that makes use of Bayesian a priori and

a posteriori probabilities is used. First, they select two observations randomly from the full set of observations. Second, they introduce angular deviations in right ascension and declination and assume topocentric ranges. Then, they compute sample orbits from the two heliocentric rectangular coordinates available. Optionally, one can make use of preliminary orbits obtained from one of the conventional methods to constrain the volume of phase space to be searched.

Their analysis shows that the linear approximation in the differential correction can severely break down in the case of very short observational arcs or small numbers of observations. The new statistical ranging method allows one to examine the orbital element phase space for possible orbits even in the most indeterminate cases. Results for poorly observed main-belt asteroids imply that orbital classification based on a single initial orbit is by no means an unambiguous task. The preliminary results indicate that the Bayesian approach can be useful in orbit determination for newly discovered asteroids. In particular, incorporating a priori information allowed them to distinguish between realistic and unrealistic orbit solutions.

2.2.7 Statistical Correlation of Observations

Another approach followed by Schneider (2012) uses the Markov Chain Monte Carlo (MCMC) method to sample distributions of orbit parameters describing the correlation between the tracklets. Rather than combining the observed angular positions at closely spaced times into a single estimate of angle and rate, all the angular positions are used to constrain the parameters of the orbit model for the observed object. The tracklet linkage is based on the overlap between probability distributions of the orbit model parameters. The model defines a matrix N_{orb} x N_{trck} where N_{orb} and N_{trck} are the number of orbits and tracklets respectively. The MCMC method finds the most likely matrix (best tracklet combinations), i.e. the best global solution, instead of performing tracklet pairwise checking.

An upside of using this method is that it looks for the best global solution, instead of pairwise checking every tracklet with every tracklet. But a few downsides to this method can be pointed out as well. Already for a simple problem (3 tracklets) about 500,000 samples are needed. This involves a significant amount of computing power or time. Another point to be made is that the method is very complicated, certainly when compared to the admissible region approaches. A lot of parameters have to be tuned for this method to work, such as a priori distributions.

Besides this, a common problem with Markov chains is that they can display unexpected convergence behaviors and it is difficult to find a control break criterion. For example, in the example considered by Schneider (2012), the chains occasionally get "stuck" at a single parameter value for many consecutive steps.

2.2.8 Multiple Hypothesis Tracking

Another group of authors, including DeMars and Jah (2013), Singh et al. (2013), Gadaleta et al. (2012), pursued a slightly different way that brings towards a Multiple Hypothesis Tracking (MHT) paradigm. Instead of choosing a different space (e.g. Poincaré), DeMars and Jah (2013) and other authors (Hussein et al., 2014) solve the problem of discretization using a Gaussian Mixture Model to weigh the $\rho/\dot{\rho}$ hypotheses within the admissible region.

The comparison of the attributables to evaluate the tracklet association is a covariance-weighted difference. There are several functions that can be used for the computation of this difference. One of the well-known functions is the Mahalanobis distance. In Hussein et al. (2014), Singh et al. (2013), further possible functions are indicated and a general explanation of the MHT principles is given. The MHT method is the natural extension of a pairwise tracklet correlation (usually two tracklets at two different epochs) to a correlation with three or more tracklets. However, in practical applications for performance reasons, it is not possible to process the tracklets at all (more than two) epochs simultaneously. Instead, the correlation is solved sequentially, over a sliding window. As a consequence, the decision to correlate two tracklets can be postponed and taken later on the basis of additional measurements. The positive side of MHT is the capability to associate more than two tracklets to an object, thus postponing the definitive correlation. This helps to identify false alarms and will decrease the number of false associations between tracklets. Therefore, this method will lead to a significant increase in performance when applied to an environment with a high density of targets. The drawback of using MHT algorithms is the required computational cost. Note that the correlation of three or more tracklets leads to a so-called NP-hard problem, which can not be solved in polynomial time.

2.3 Benefits and drawbacks of different approaches

The benefits and drawbacks of the different methods are summarized according to the following criteria:

- Performance: The number of calls in the algorithm determines the time needed to find the correlation solutions. In general, it is possible to distinguish between methods doing a loop over all possible samples (regular grid testing) and others where the search in the sample space follows a certain rule (optimization), e.g. gradient descent search. Those methods which do not use attributables have in general more loops that consider also the single observations. If MCMC is used, an even higher number is needed for the Monte Carlo sampling. The methods that try to associate more than two tracklets simultaneously also need further developments to improve their correlation performance. These criteria lead us to assess the limitations of the algorithms such as Statistical Ranging, Statistical Correlation of Observations and Multiple Hypothesis Tracking.

- Multi-rev problem: The methods based on attributables cannot solve the ambiguity in the number of revolutions the observed object potentially made between the tracklets. The two-body boundary-value problem has potentially multiple solutions due to the ambiguity in the anomalies. With an increasing number of revolutions, more multi-revolution solutions become physically feasible. An extreme case is given if the object is observed two times at the same location. Then, there are multiple solutions with equal angular rates but different semimajor axis values. The ambiguity can be removed with a prefilter, which was applied in the boundary approach by (Siminski et al., 2014). A least-squares refinement can also be used to eliminate the ambiguity as is the case for the approaches proposed by Musci et al. ('Orbit improvement for GEO objects using follow-up observations') in subsection 2.2.1 and Fujimoto et al. (2014) in subsection 2.2.4.

- Perturbations: In general the perturbation forces can be included in the model used for the orbit propagation. In the boundary value approach, the traditional solutions to the Lambert problem typically only account for two-body dynamics. This difficulty can be circumvented by using numerical orbit models and modern shooting methods. For all methods, it is anyway possible to take into account perturbations in the least-squares refinement. However, none of the methods mentioned in this section include perturbations in the initial orbit determination step.

3 The optimized boundary value initial orbit determination method

Orbit determination of newly detected objects is critical for space debris cataloging. If the tracklet association algorithm is not robust enough many work hours will be required to determine the orbit manually. A least-squares estimator is a popular choice due to its ability to provide both a maximum likelihood state estimate and the uncertainties of each dimension of that state. In space debris tracking the least-squares method is used extensively. However, a minimum number of observations are required for the least-squares estimator to work robustly. In general, the minimum number of observations needed for a least-squares estimator to work is greater than the number of parameters that are being estimated (Zittersteijn, 2017). This is due to the typical observation strategies that are used in space debris tracking. An object is often observed in very short arcs of several observations. Since each short arc of observations only constrains a small portion of the object's orbit (typically about two to five minutes of a 24-hour orbit for a GEO object) the orbit is not well constrained, even if the total number of observations might suggest otherwise.

An Initial Orbit Determination (IOD) method is used to provide an initial orbit robustly with a small number of observations. This initial orbit can then be used as an initial value in the least-squares estimator to further improve the orbit estimate if necessary. Apart from being robust the IOD method should also provide a consistent indicator of the quality of the orbit. IOD is a topic that has been addressed extensively. Some of the IOD methods were described in the previous chapter. Although these methods are interesting, many do not exploit the observation strategies of space debris to achieve the goal.

3.1 Introduction to OBVIOD

In this work, a new IOD method is developed called the Shooting-Bisection Optimized Boundary Value Initial Orbit Determination (Shooting-Bisection OBVIOD) method. It relies heavily on previously developed work on the optimized boundary value problem (Siminski et al., 2014). The latter proposed an orbit determination method using available information of two tracklets. This approach works with a boundary-value formulation and uses an optimization scheme to find the best fitting orbits (OBVIOD). It solves the Lambert problem, a special case of the orbital boundary value problem, which consists of two-position vectors at separate epochs. The IOD in OBVIOD provides an unperturbed solution. To add perturbations in the IOD, a so-called Shooting method is proposed in this work. The following section will explain the OBVIOD method proposed by (Siminski et al., 2014).

An initial-value method was also proposed by the authors before choosing the boundary value approach due to the former's limitations. In the initial-value technique, while augmenting the tracklet information from the first observation epoch with the two free parameters $(\rho_1, \dot{\rho}_1)$, a full state is defined

---

$$\hat{\boldsymbol{y}}(t_1) = \begin{pmatrix} \boldsymbol{r}(\rho_1) \\ \dot{\boldsymbol{r}}(\rho_1, \dot{\rho}_1) \end{pmatrix}, \qquad (3.1)$$

which can be used as an initial value to numerically or analytically integrate the equation of motion to the second epoch. Consequently, the solution $\hat{\boldsymbol{y}}(t_2)$ can be computed. The hat over the state variable indicates that the orbital solution is a hypothesis and not necessarily the true one. The observation arc at the second epoch t_2 serves as a discriminator to decide whether a hypothesis is accepted or rejected.

A loss function is minimized which describes the difference between the actual second observation $\boldsymbol{a}_2$ and the modeled value $\hat{\boldsymbol{a}}_2$. As the measurements are affected by noise, the difference in the loss function is scaled with its uncertainty. The loss function is then given by

$$L(\boldsymbol{p}) = (\boldsymbol{a}_2 - \hat{\boldsymbol{a}}_2)^T (\boldsymbol{C}_{\hat{\boldsymbol{a}}_2} + \boldsymbol{C}_{\boldsymbol{a}_2})^{-1} (\boldsymbol{a}_2 - \hat{\boldsymbol{a}}_2), \qquad (3.2)$$

where the range and range-rate hypotheses are combined in $\boldsymbol{p} = (\rho_1, \dot{\rho}_1)$ for convenience and

$$\hat{\boldsymbol{a}}_2(\boldsymbol{a}_1, \boldsymbol{p}) = (\hat{\alpha}_2, \hat{\dot{\alpha}}_2, \hat{\delta}_2, \hat{\dot{\delta}}_2)^T, \qquad (3.3)$$

is the propagated modeled observation obtained from $\boldsymbol{y}(t_2)$. The covariance matrix $\boldsymbol{C}_{\boldsymbol{a}_2}$ describes the uncertainty of the second measurement and $\boldsymbol{C}_{\hat{\boldsymbol{a}}_2}$ is the propagated covariance of the initial measurement. The topography of the loss function for the parameters $\boldsymbol{p} = (\rho_1, \dot{\rho}_1)$ is illustrated in Fig. 3.1, where the same geostationary object is re-observed after 3.75 days. The semimajor axis and orbital period stay constant on the dashed lines. The numbers in brackets denote the range of revolutions k (in orbital periods) in the enclosed regions. The true solution is in the range $k \in [3.5, 4]$.
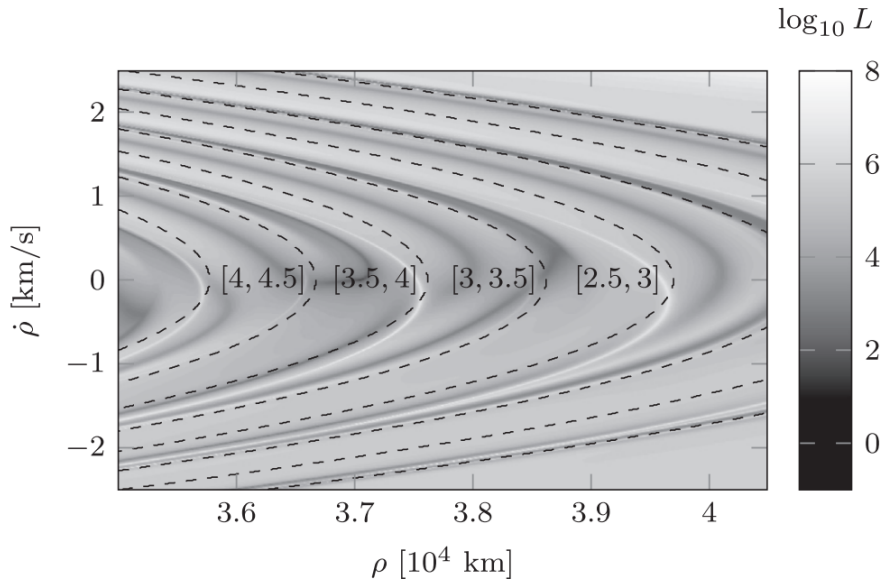
Fig. 3.1 – Loss function for initial-value method with range and range-rate as the free parameters. The same geostationary object at the longitude 10 degrees has been re-observed after 3.75 days.

The topography of the loss function has been analyzed in (Siminski et al., 2013b) to assess the suitability for computational optimization methods. Several hills and valleys can be observed and, consequently, several local minima inside the valleys can be found that are potential candidates for a common orbit solution of the two measurement arcs. This results in a multi-modal optimization problem and makes it difficult to find a global minimum within the admissible region. The individual valleys must be identified beforehand. They are roughly separated by allowing only a specific range of orbital revolutions k between the observation epochs. However, multiple valleys inside the bounds can still be observed and this separation can lead to very narrow regions as observed in Fig. 3.1, which is disadvantageous for iterative search algorithms as these might step outside the feasible area too easily. An appropriate alternative parameter system has been therefore proposed in Siminski et al. (2013a) to account for the difficult topography. The semimajor axis a_1 and a relative range $\tilde{\rho}_1$ at the first epoch are used as the free parameters. The derivation and description of the new parameters can be obtained from Siminski et al. (2013b).

The topography of the loss function for the new set of parameters is illustrated in the following Fig. 3.2. It shows a more suitable pattern for optimization algorithms. The representation allows one to split the loss function into rectangles with the same number of orbital revolutions. Even though most valleys have been successfully separated from each other, several hills and valleys inside an orbital revolutions range can still be seen. Larger time gaps lead to more ambiguous solutions. Consequently, the time gap between observations is shown to be important when sectioning the region. Future research must find ways to identify the different valleys inside such a range. If the location or extent of all valleys is known, each one can be individually minimized using a gradient-based optimizer.
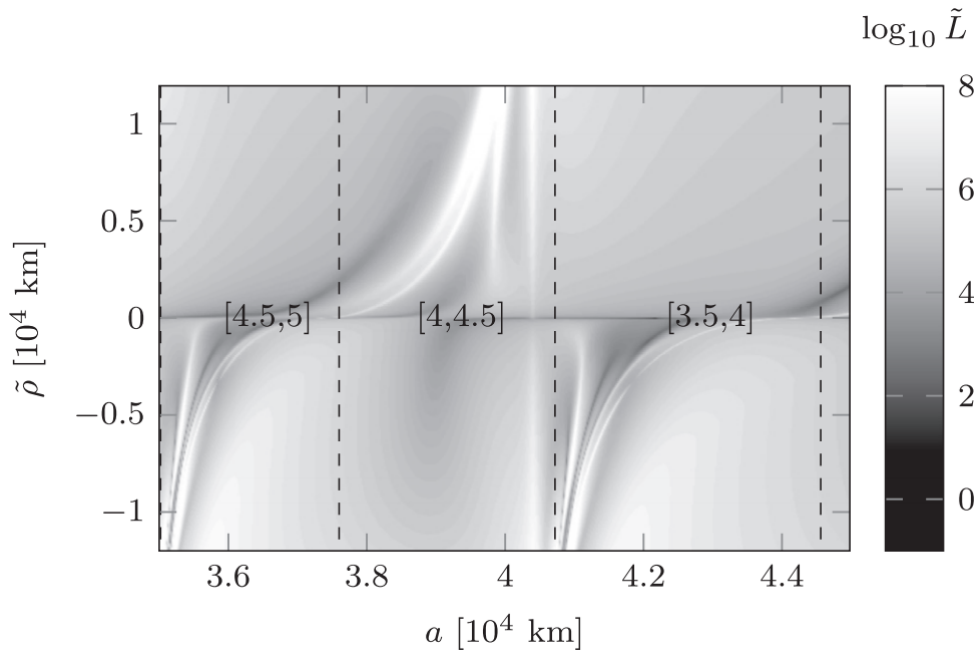
Fig. 3.2 – Loss function for initial-value method with semimajor axis and relative range as the free parameters. The same observations are used as in the previous Fig. 3.1.

3.2 Working in OBVIOD

Instead of parameterizing the problem at the initial epoch only, more symmetric approaches have been developed that use the boundary-value formulation to define a state hypothesis. The methods mentioned in subsection 2.2.5, subsection 2.2.7, statistical ranging from subsection 2.2.6 were examples of such approaches. The line-of-sight information at both observation epochs

$$\boldsymbol{z} = (\alpha_1, \delta_1, \alpha_2, \delta_2)^T \tag{3.4}$$

is used to constrain the state of the tested hypotheses. A complete orbital state is then defined by augmenting the line-of-sight information with unknown range values at both epochs (ρ_1, ρ_2). Siminski et al. (2014) introduced a method where an optimization scheme is used to identify tracklets of common objects. The angle measurements consist of series of α and δ values. Linear regression is performed over these series, resulting in average α, δ values and the corresponding $\dot{\alpha}$, $\dot{\delta}$ for a meantime. Using the attributable vectors over simple measurements provides an advantage as the angular rates information is now available. Moreover, the mean angular positions, rates obtained from the linear regression will have higher accuracy compared to the raw observations. The next step involves a range hypothesis, which is used with the line of sight vectors and station positions to compute position vectors. The Lambert's problem is solved, giving velocities at both epochs. The angular rates obtained from the previous step are compared with the ones from the attributable vector using a loss function. The latter is based on the difference between the measured and the modeled angular rates scaled by the uncertainty. In this case, the Mahalanobis distance (MD) is used as the loss function. For a distribution y, with mean $\overline{y}$ and covariance matrix C_y, the Mahalanobis distance for each point y_i is defined by:

$$D_M(y) = \sqrt{(y_i - \overline{y})^T C_y^{-1} (y_i - \overline{y})} \tag{3.5}$$

A minimization algorithm called Broyden Fletcher Goldfarb Shanno (BFGS) is used to search for the loss function minimum. Press et al. (1992) briefly explain the working of this algorithm. If the MD is below a certain threshold, the tracklets are said to be correlated. In other words, they belong to the same object. The range hypothesis corresponding to the minimum is accepted and the initial orbit is computed for these tracklets. Fig. 3.3 shows the schematic of OBVIOD.

The topography of the loss function for the free parameters $\boldsymbol{p} = (\rho_1, \rho_2)$ is illustrated in Fig. 3.4, 3.5 and 3.6 where the same geostationary object is re-observed after 3.75 days. The numbers in brackets denote the range of revolutions k (in orbital periods) in the enclosed regions. The true solution is in the range $k \in [3.5, 4]$. Three individual discrete cases of the loss function defined by the allowed k interval have been created. In contrast to the initial-value method, each discrete case of the loss function contains only one local and therefore also the global minimum. The global minimum for the overall problem is then obtained by identifying the value of k that yields the smallest loss-function minimum.
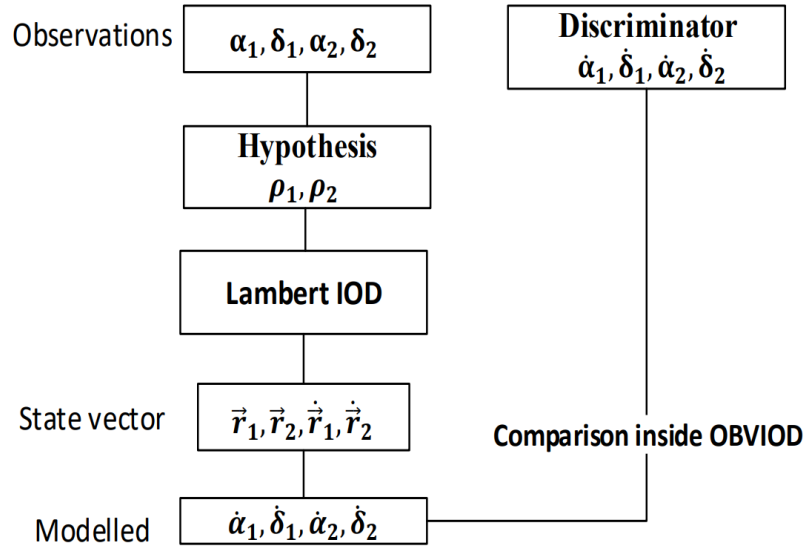
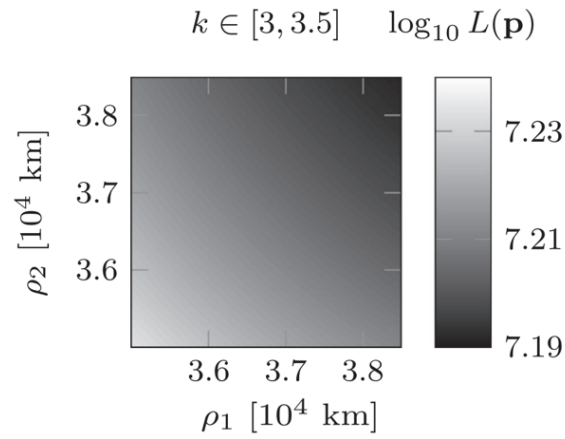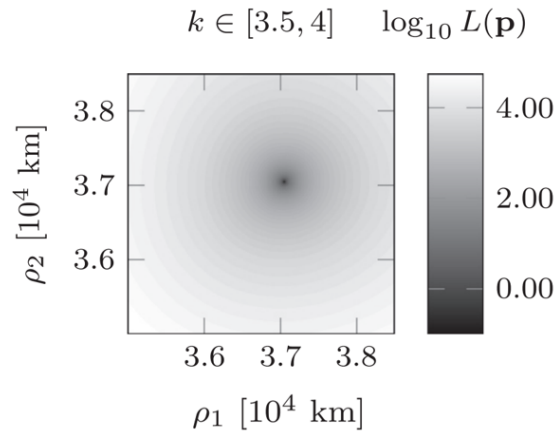**Fig. 3.3** – Process Flow in OBVIOD.

Fig. 3.4 – Loss function for boundary-value method. The loss function is evaluated for different ranges of allowed orbital periods k.

Fig. 3.5 – A local minimum can be seen for this value of revolutions.

$$k \in [4, 4.5] \qquad \log_{10} L(\mathbf{p})$$
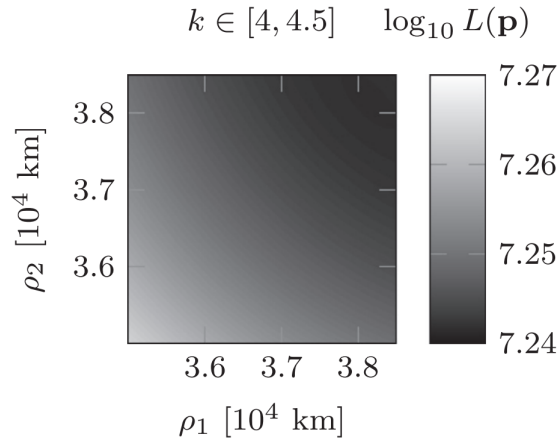
Fig. 3.6 – No loss function minimum is found for $k \in [4, 4.5]$.

3.3 Lambert's Problem

Lambert's problem deals with the determination of a Keplerian orbit connecting two points in space with a given time-of-flight and the direction of flight. The earliest formulations were made by Lagrange (1788) and Gauss (1963). Over the years, different algorithms have been proposed to solve Lambert's problem. The most notable ones which have adopted universal variables as a free parameter for computation are Lancaster (1969), Gooding (1990), Izzo (2014), Bate et al. (1971), Battin (1999) and Shen and Tsiotras (2003). Lagrange (1788), Thorne (2014) and Prussing (2000) chose semimajor axis while Herrick and Liu (1959), Bate et al. (1971) use semi-latus rectum. A comprehensive analysis along with a collection of references is provided in Torre Sangrà and Fantino (2015).

A Lambert's problem is stated as the following (Bate et al., 1971): given two points P_1 and P_2 in space, the time-of-flight t_f, and direction of flight, determine the Keplerian orbit that takes a body from P_1 to P_2 in the given t_f. Fig. 3.7 illustrates the geometry of a typical Lambert's problem. In the figure, P_1 and P_2 are two fixed points in the space, with radii of $\boldsymbol{r}_1$ and $\boldsymbol{r}_1$, F is the primary focus, F^* is the fictitious focus, d stands for the chord which is between P_1 and P_2, and θ is the transfer angle. The problem is to determine the Keplerian orbit such that a body is at P_1 initially and must arrive at P_2 at a specified time which is denoted by t_f. The triangle FP_1P_2 is often referred to as the space triangle.

According to Lambert's theory (Battin, 1999), the time-of-flight is a function only of the semimajor axis of the transfer orbit, the sum of the radii $r_1 + r_2$, and the chord length d, i.e.,

$$t_f = f(a, d, r_1 + r_2). \tag{3.6}$$

From this description, the input quantities are defined as r_1 and r_2, the force of the central point described by the central gravity coefficient μ, and the length of the orbit arc Δt. The angle θ is the angle between the vectors r_1 and r_2 and can be between 0 and 2π. If the Δt is large enough, more than one solution is possible. These additional solutions are called multi-revolution solutions and they occur in pairs. The number of revolutions is denoted by N. Therefore the output quantities are $2N + 1$ solutions, each consisting of a radial velocity V_r and a transverse velocity V_t at epoch t_0 and t_1.
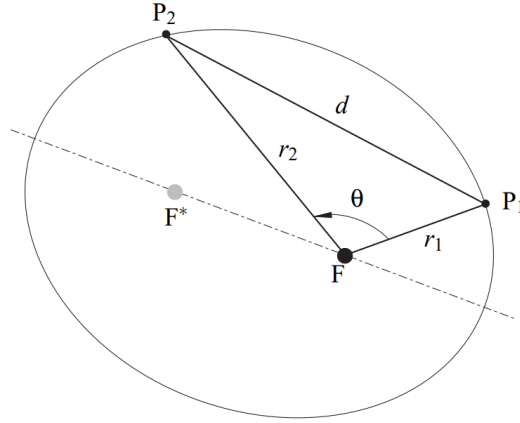
Fig. 3.7 – Geometry of the Lambert's problem (Zhang et al., 2010).

In order to find a solution to this problem, an iterative procedure is needed. One parameter needs to be defined on which to iterate. The choice of this parameter has a significant impact on the quality of the solution. Since the semimajor axis a is directly related to the orbital energy, it is a likely candidate as it will be relatively straightforward to derive the relations. However, this would result in having solutions in pairs or no solutions at all (depending on the geometry of the problem). Since at least one solution is required (and possible), this parameter choice alone does not fulfill the requirements. Instead, a new parameter is defined that is dependent on a. It is given in Eq. (3.7) (Gooding, 1990)

$$x^2 = 1 - \frac{s}{2a}, \tag{3.7}$$

where s is the semi-perimeter of the triangle FP_1P_2. The variable that is iterated can vary from one Lambert problem solver to another. Although the parameter x performs well (Lancaster (1969); Gooding (1990); Izzo (2014)), there is still a search for a parameter that might improve the solution procedure, such as in Sun et al. (1987). If the length of the orbit arc is expressed in a non-dimensional form as in Eq. (3.9), Fig. 3.8 is obtained. λ is defined as

$$\lambda^2 = \sqrt{\frac{s-c}{s}} \tag{3.8}$$

$\lambda \in [\text{-}1, 1]$ is positive when $\theta \in [0, \pi]$ and negative when $\theta \in [\pi, 2\pi]$. It is used by Izzo (2014) along with M which stands for number of revolutions. Zhang et al. (2010) talk about different possible Lambert solutions in terms of types of orbits. Given two points P_1 and P_2 in space, there are two elliptic orbits with the same semimajor axes that connect the two points. For a given Lambert's problem, there are three orbit categories defined by the location of the vacant focus (Zhang et al., 2010).

$$T = \sqrt{\frac{8\mu}{s^3}}\Delta t \tag{3.9}$$
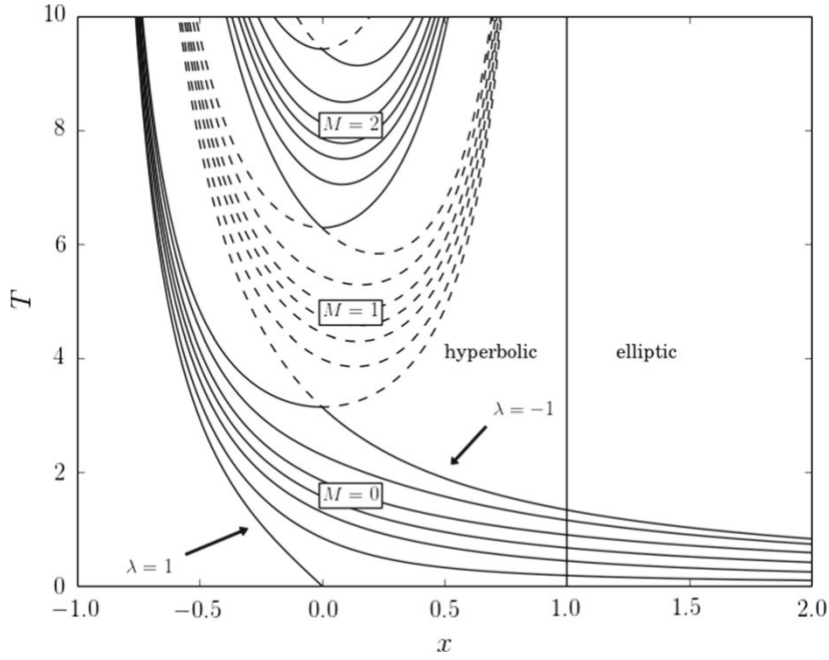
Fig. 3.8 – Time-of-flight curves parametrized using x for different λ and M values (Izzo, 2014).

1. The minimum-energy orbit is the one in which the vacant focus F^* lies on the $\overline{P_1 P_2}$ line segment. In this case, the semimajor axis of transfer orbit is

$$a_m = \frac{s}{2}, \tag{3.10}$$

where

$$s = \frac{r_1 + r_2 + d}{2}, d = \|\boldsymbol{r}_1 - \boldsymbol{r}_2\|, \tag{3.11}$$

which is the length of the chord connecting P_1 and P_2.

2. For $a > a_m$, the *short-path orbit* is shown in Fig. 3.9

3. For the same value of a, the *long-path orbit* is also shown in Fig. 3.9

The vacant focuses in the short- and long-path orbits are $F^*{}_{short}$ and $F^*{}_{long}$, respectively, which are symmetric about the connecting line $\overline{P_1 P_2}$. As shown in Fig. 3.9, for a long-path orbit, F and F^* lie on opposite sides of the $\overline{P_1 P_2}$ line segment, whereas for a short-path orbit, F and F^* lie on the same side of the $\overline{P_1 P_2}$ line segment.
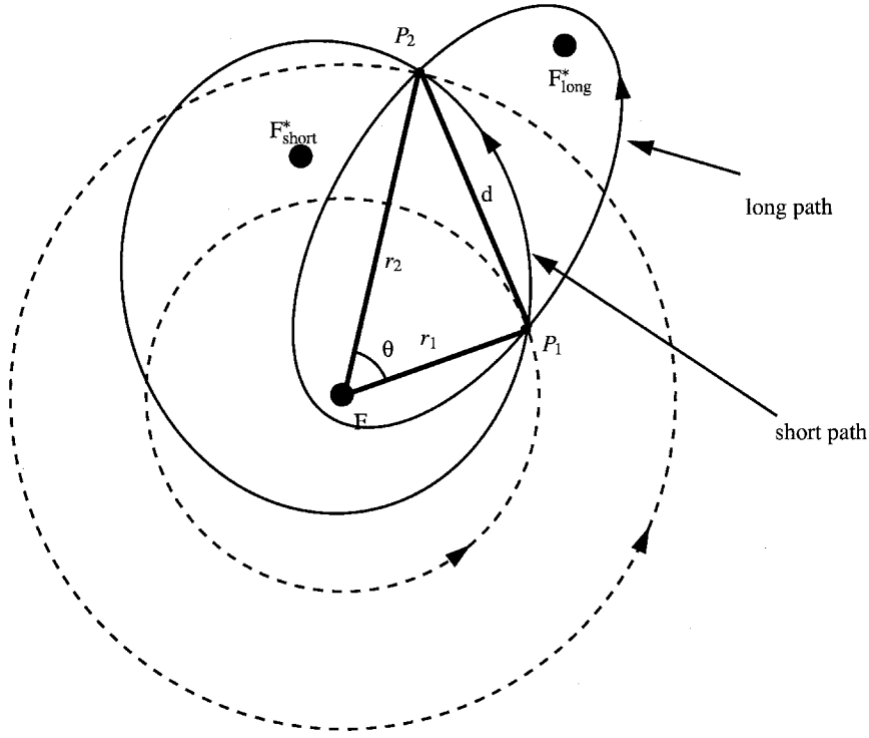
Fig. 3.9 – Orbital geometry for Lambert problem showing long path, short path and vacant focuses (Shen and Tsiotras, 2003).

From Lagrange's formulation of the multiple-revolution Lambert's problem, the relationship between transfer time t_f and semimajor axis a can be expressed as shown below:

$$\sqrt{\mu}t_f = a^{\frac{3}{2}}[2N\pi + \alpha - \beta - (\sin\alpha - \sin\beta)], \tag{3.12}$$

where μ is the gravitational parameter, N is the number of revolutions and α and β are Lagrange's parameters defined by

$$\begin{aligned}\sin\frac{\alpha}{2} &= (\frac{s}{2a})^{\frac{1}{2}}, \\ \sin\frac{\beta}{2} &= (\frac{s-d}{2a})^{\frac{1}{2}}.\end{aligned} \tag{3.13}$$

Let $\cos^{-1}(1 - \frac{s}{a}) = \alpha_0 \in [0, \pi]$ and $\cos^{-1}(1 - \frac{(s-d)}{a}) = \beta_0 \in [0, \pi]$, then from the geometric interpretation of the variables α and β, two distinct cases are obtained:

1. If $\theta < \pi$, then for the short path, $\alpha = \alpha_0$ and $\beta = \beta_0$, while for the long path, $\alpha = 2\pi - \alpha_0$ and $\beta = \beta_0$.

2. If $\theta \geq \pi$, then for the short path, $\alpha = 2\pi - \alpha_0$ and $\beta = -\beta_0$, while for the long path, $\alpha = \alpha_0$ and $\beta = -\beta_0$.

Zhang et al. (2010) discuss various constraints that can be possibly used to reduce the number of practical solutions to be computed from a Multiple-Revolution Lambert's Problem. These constraints were investigated, but the ranges of semimajor axis originating from

them were found to be a subset of the constraints defined in section 4.3.1. However, the constraints described in (Zhang et al., 2010) are more generic and could be tailored for cases where the user could define the apogee, perigee limits for a specific mission and find the solutions for a given orbital problem. The authors also mention about the relationship between eccentricity and semimajor axis, interested readers could refer to their paper for more details.

In Prussing (2000) a clear analysis of the multiple-revolution solutions to Lambert's problem based on the classical Lagrange's formulation is presented. It shows that for a given Lambert's problem, there are two N-revolution transfer orbits with $N > 0$ where N denotes the number of revolutions, and there is only one zero-revolution transfer orbit. Therefore, there are a total of $2N_{max} + 1$ solutions for a given Lambert's problem, with N_{max} being the maximum number of revolutions allowed. In Prussing (2000), the Newton-Raphson iteration scheme is used to solve for the $2N_{max} + 1$ solutions.

The next chapter will use the concepts described in the previous sections to discuss the new methods developed. The behavior of an initial orbit determination method based on Lambert's problem is shown. Especially the limitations of the latter in multiple-revolution scenarios and perturbed orbits.

4 Shooting method

In the previous chapter the OBVIOD method was presented which uses an optimization scheme to find the best fitting orbits from two short-arc tracklets. The IOD in OBVIOD provides an unperturbed solution. In order to add perturbations in the IOD, a so-called Shooting method is proposed here. The following sections will show the working of the latter and the development of the present version of the algorithm.

4.1 Introduction to Shooting method

When ordinary differential equations are required to satisfy boundary conditions at more than one value of the independent variable, the resulting problem is called a two point boundary value problem. As the terminology indicates, the most common case by far is where boundary conditions are supposed to be satisfied at two points — usually the starting and ending values of the integration. However, the phrase "two point boundary value problem" is also used loosely to include more complicated cases, e.g., where some conditions are specified at endpoints, others at interior (usually singular) points.

The crucial distinction between initial value problems and two point boundary value problems is that in the former case one is able to start an acceptable solution at its beginning (initial values) and just march it along by numerical integration to its end (final values); while in the latter case, the boundary conditions at the starting point do not determine a unique solution to start with — and a "random" choice among the solutions that satisfy these (incomplete) starting boundary conditions is almost certain not to satisfy the boundary conditions at the other specified point(s) (Zhang et al., 2010).

Acton (1970) talks about intelligent initial-value methods which can prove to be useful in a strongly nonlinear set of algebraic equations, as the number of effective methods for their solution is distressingly small. For the simplest boundary-value problem, the second-order equation, one is given a boundary condition at each end of an interval. To treat it as an initial-value problem one needs only to assume a second boundary condition at one end, integrate via standard predictor-corrector techniques until one gets to the other end, and there compare the value that one obtained with that which one desires. One can then make an adjustment in their assumed initial value and integrate a second time, and compare a second time. One's third choice for the unknown initial condition can be guided by an interpolative philosophy based on the two values they have already found at the far end of the range. The process is strictly brute force, contains no particular booby traps, and will ultimately succeed. On the negative side, it is a lot of work.
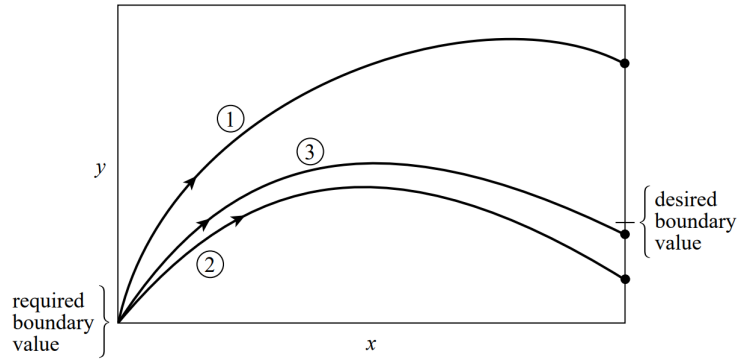
Fig. 4.1 – Working of Shooting method (Press et al., 1992).

The Shooting method proves to be useful in these cases. It belongs to the class of two-point boundary value problems. It treats the boundary value problem as an initial value problem. It chooses an initial value of the dependent variable at the first boundary, propagates the function to arrive at the other boundary. This solution is compared with the second boundary value. Free parameters at the first boundary are adjusted to satisfy the desired second boundary value. Fig. 4.1 shows how the different initial values of the dependent variable are taken at the first boundary value in order to reach the desired boundary value.

4.1.1 Shooting method in OBVIOD

The boundary values in the case of Shooting-OBVIOD are angular measurements at both the epochs. Using the attributable vector one has the mean angular positions and rates. The range hypothesis is made for both the boundaries. The station position and velocity at both the epochs is known, the only unknown parameter at the initial epoch is $\dot{\rho}_1$ (range-rate). It is chosen as the free parameter inside Shooting IOD and is hypothesized at the initial epoch. The orbit is computed at this epoch and propagated to the second epoch. The propagation step involves perturbations such as solar radiation pressure, Earth's geopotential terms, solar and lunar gravitational forces.

Fig. 4.2 – Process flow in Shooting-OBVIOD.

The iteration parameters inside Shooting-OBVIOD remain to be ρ_1 (range at first epoch) and ρ_2 (range at second epoch). This is based on the analysis done by Siminski et al. (2014) on the loss functions and performance.

The change of variables from (ρ_1, ρ_2) to $(\dot{\rho}_1, \rho_1)$ takes place inside Shooting procedure in order to allow for a propagation from the initial epoch to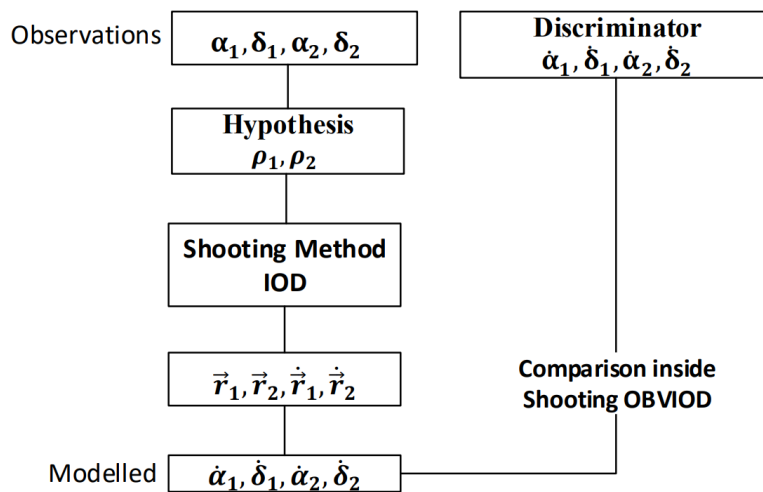 the final epoch for the pair ρ_1, ρ_2. This is because the Shooting method allows for IOD with the given pair with the addition of perturbations. The Shooting IOD replaces the Lambert IOD during the minimization of the loss function. The resulting schematic of Shooting-OBVIOD is shown in Fig. 4.2.

The OBVIOD algorithm uses line search inside the BFGS optimization to search for a direction of descent in order to move towards the function minima. The line search approach uses a variable stepsize for a (ρ_1, ρ_2) pair to search for a direction in which the loss function value decreases in the consecutive step. This technique adds or subtracts the value of stepsize from ρ_1 and/or ρ_2 to find the new pair of (ρ_1, ρ_2) that enables to iterate towards the loss function minimum. Once a solution is found, the least-squares orbit improvement takes place. If it results in a root mean square (rms) below threshold, that tracklet pair is said to be correlated and the orbit is accepted.

The first boundary value of Shooting IOD is the state at initial epoch, hence the geocentric position r_1 and velocity $\dot{r}_1$. Given the angular positions and angular velocities $(\alpha, \delta, \dot{\alpha}, \dot{\delta})$ from measurements and ρ_1, ρ_2 from OBVIOD hypothesis the only remaining unknown is the range-rate $(\dot{\rho})$. The orbit is computed using $\alpha_1, \delta_1, \dot{\alpha}_1, \dot{\delta}_1, \rho_1$ and $\dot{\rho}_1$. The range-rate at the first boundary $(\dot{\rho}_1)$ is chosen as a free parameter for the iterations. For a $\dot{\rho}_1$ hypothesis, the initial state is computed and propagated to the second boundary to get a ρ_2 value. The value of the free parameter $\dot{\rho}_1$ is updated based on the root-finding algorithm used in subsequent iterations until the value of range (ρ_2) is same (upto a precision factor) as the ρ_2 from the OBVIOD iteration. The method is described more in detail in the following sections.

4.2 Newton Raphson in Shooting

The Shooting procedure employs a root-finding algorithm to find a solution that satisfies the desired boundary value. Newton-Raphson method is used for this purpose. It extrapolates the local derivative to the next estimate of the root (Press et al., 1992). Assuming x_1 to be the current point and $f(x_1)$ to be the function value at that point, the next estimate of the root of function $f(x)$ becomes:

$$x_2 = x_1 - \frac{f(x_1)}{f'(x_1)} \tag{4.1}$$

Geometrically it consists of extending the tangent line at a current point x_1 until it crosses zero, then setting the next guess x_2 to the abscissa of that zero-crossing (see Fig. 4.3).

In case of Shooting IOD, it searches a root for the function $(\rho_{2j} - \rho_2)$ using the free parameter $\dot{\rho}_1$, j being the iteration number. The Newton-Raphson method requires an initial value of the latter to start the iterations. In the initial versions of the algorithm, the idea was to choose this value from admissible bounds proposed by (Schumacher et al., 2013) on different parameters including $\dot{\rho}$. The said bounds originate from apogee and maximum possible perigee speeds, which were tailored to the current scenario for geostationary orbits. A random value from this interval was chosen to be the starting value for the iterations inside Newton-Raphson. However, it was observed that it did not perform well and the method

failed to converge by taking random starting values from this interval. Even a small change of about 1% in the initial value could hinder the convergence and the Shooting method wasn't be able to find a root for a given (ρ_1, ρ_2). Hence, it was decided to use the solution of unperturbed Lambert algorithm as an initial value. The reason for poor performance with previous procedure could be due to the fact that the Newton-Raphson method works well only for local convergence and needs a good starting value.
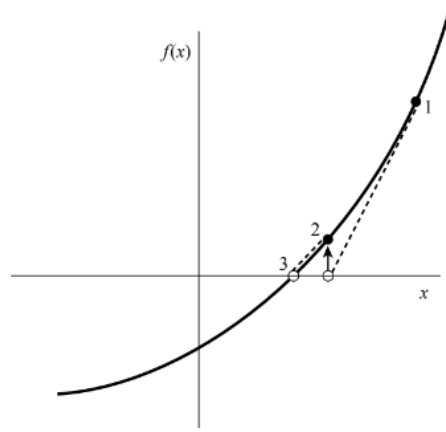

Fig. 4.3 – Function derivative at point x_1 is used to find the next estimate x_2 of the function's root (Press et al., 1992).

4.2.1 Performance improvements for Newton-Raphson Shooting-OBVIOD

The Newton-Raphson Shooting-OBVIOD was tested for different number of revolutions and Area-to-mass ratio (AMR) values. It was found that the execution time was much higher in comparison to the unperturbed Lambert OBVIOD, owing to the use of numerical propagator. In order to lower the execution time and maintain the correlation performance, flow control techniques were used. One of the measures taken was to perform half the iterations in Shooting IOD using a Keplerian propagator, while the rest half of iterations benefit from the propagation with perturbations. The resulting schematic of the Shooting IOD is as shown in Fig.4.4, j is the current iteration number in the IOD.

Other measures taken to improve the performance included:

1. Limit on minimum stepsize: In the original OBVIOD algorithm, the linesearch iterations taking place in the minimum gradient search algorithm (BFGS) continue until a decrease in the function value is noted for a particular step. The values of ρ_1, ρ_2 are then modified using a variable step size. The latter continues to decrease during these iterations and reached values around one micrometer or less in some cases. In Newton-Raphson Shooting OBVIOD, this value was limited to 1 centimeter in order to come out of the line search iterations loop if the stepsize keeps decreasing until the maximum linesearch iterations limit is reached. In this case, the Hessian matrix of the loss function to be used in the corresponding BFGS iteration is reset so that the further BFGS iterations can continue the minimum search.

2. Number of iterations in BFGS: The number of iterations taking place in the BFGS algorithm was 10,000 in the original OBVIOD. As the unperturbed Lambert IOD was

faster than the Shooting IOD this wasn't noticeable. However, with the introduction of Shooting IOD with perturbations, this number had to be reduced to an acceptable value in order to save time. The new number of iterations was chosen after testing various cases of revolutions, AMR values for correlation performance. It was made sure that the number of iterations did not limit the whole algorithm from making correlations. On the other hand, this number could be modified if the parameters in the functioning of the algorithm are changed somehow or if an unforeseen case with a particular number of revolutions and/or AMR value is tested in the future.
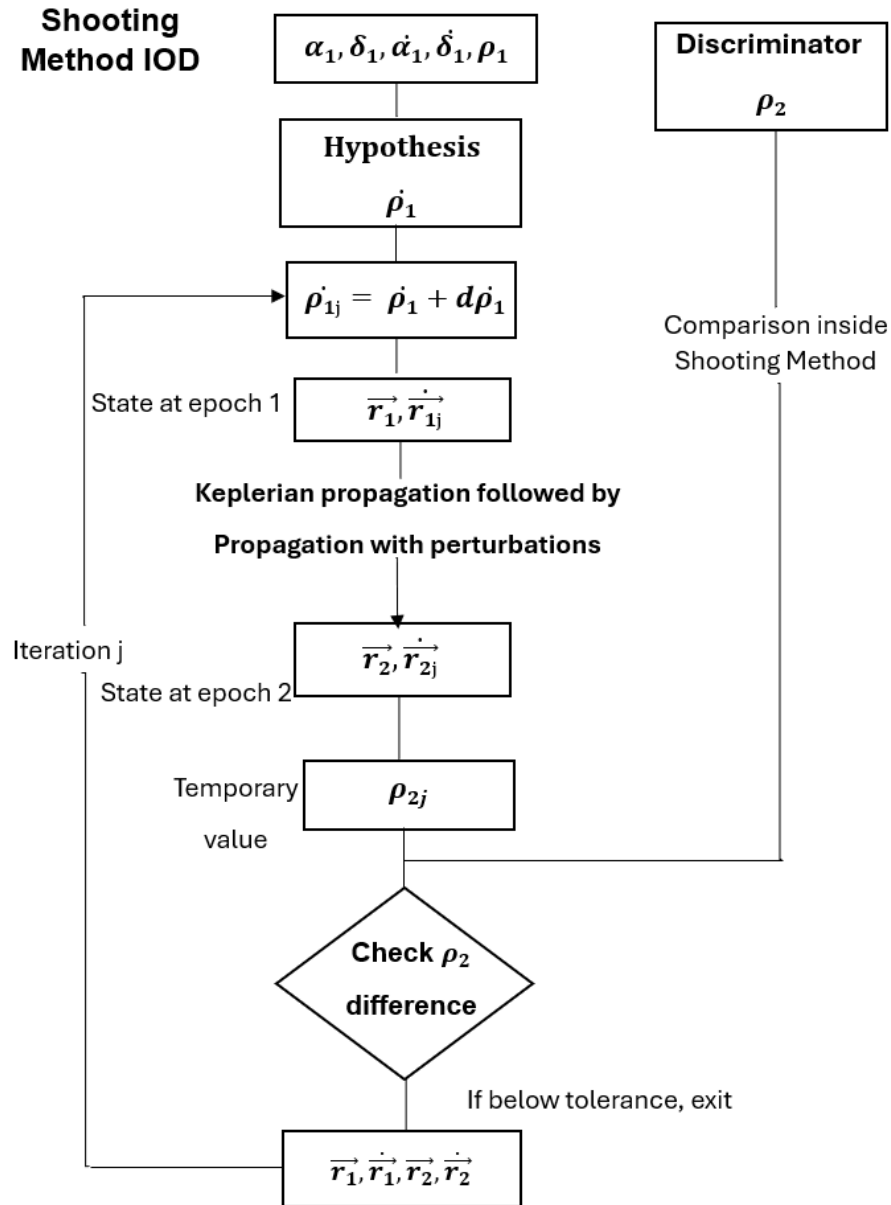

Fig. 4.4 – Flow diagram of Shooting IOD using Newton-Raphson method.

3. Divergence in Shooting algorithm: Flow control was used inside Shooting algorithm to prevent iterations in case the magnitude of the instantaneous difference $\rho_{2j} - \rho_2$ (Newton-Raphson function) is increasing rather than converging to the minimum.

4.2.2 Limitations of Newton-Raphson method

There were cases where the Newton-Raphson method could not find the root or diverged. This happened when observations from more than one night were considered for any AMR value. This was seen regardless the use of Keplerian propagator for half of the iterations in Shooting algorithm. The divergence for multiple night observations resonated with the fact that the multiple revolution cases have many possible solutions for the orbit determination problem. In these cases, the function inside Shooting method had multiple roots which made it difficult to converge. Another reason would be the effect of perturbations, which becomes higher for longer time intervals between the tracklets considered. The initial value from unperturbed Lambert solution was not good enough for the Newton-Raphson algorithm which has problems in global convergence.

There are additional challenges for tracklets that are close to full revolutions apart, implying the line of sight angles at first and final epoch are almost the same. In these cases the unperturbed Lambert algorithm fails and doesn't give a solution that could be used as an initial value for the Shooting iterations.

4.2.3 Limitations due to use of unperturbed Lambert solution as initial value

The initial value for Newton-Raphson algorithm is provided by the unperturbed Lambert solution. This means that the working of Shooting method is not shielded from the limitations of the Lambert algorithm. As mentioned in the previous chapter, the Lambert orbit determination takes place using the method from Izzo (2014). The Lambert's initial orbit determination algorithm mentioned in Izzo (2014) uses the Lambert problem's geometry to derive new variables in order to solve the problem. The derivations originate from the expression of time-of-flight as shown in Eq.(3.11). An important parameter used to solve the Lambert's problem in this algorithm is λ, which is defined in section 3.3.

This algorithm assumes no perturbations while solving the initial orbit determination problem. There are some scenarios where this algorithm begins to fail or becomes inaccurate. Some of the problems faced are described below:

1. Ambiguity near full revolutions: The line of sight vectors at the first epoch $\overrightarrow{u_1}$ and second epoch $\overrightarrow{u_2}$ almost overlap each other near full revolutions. The angle between $\overrightarrow{u_1}$ and $\overrightarrow{u_2}$ is called the transfer angle, it approaches zero if a full revolution case is concerned. This leads to the ambiguity in no. of revolutions and also the solution to be used (Izzo, 2014);(Zhang et al., 2010). Hence, the solution provided by the Lambert algorithm in these cases is not reliable.

2. Time-of-flight (tof) not computed for highly perturbed orbits: The algorithm proposed by Izzo (2014) involves various steps. A variable called x is defined (section 3.3), which is to be used as the iteration variable. It can be expressed as:

$$x = \cos\frac{\alpha}{2} \tag{4.2}$$

for elliptic orbits or,

$$x = \cosh\frac{\alpha}{2} \tag{4.3}$$

for hyperbolic orbits, where α is the angle derived from Lambert's problem's geometry and given in Eq.(3.11). The Lambert solver iterates on the Lancaster-Blanchard variable x using a Householder iteration scheme. Following this, various other variables are defined using x and λ. Finally the non-dimensional tof equation is derived, which is valid in all cases (parabolic, hyperbolic and elliptic). The derivations assume a non-perturbed motion of the object. The value of x is provided by initial guesses found exploiting the curve shape in a $\tau - \xi$ plane. τ and ξ are defined in terms of x and T (non-dimensional time-of-flight) respectively. ξ is the Lambert invariant according to Gooding (1990) since it is a transformation of x. The relation of τ and ξ to x and T is shown below, N is the number of revolutions.

$$d\xi = \begin{cases} \frac{1}{1+x}dx, N = 0, \\ \frac{2}{1-x}dx, N > 0 \end{cases} \quad d\tau = \frac{1}{T}dT \tag{4.4}$$

Once the initial value of x is supplied, the Householder iterations take place. A new value of non-dimensional tof and x is computed in every iteration and until the error is below tolerance, the iterations continue. The error term is defined as:

$$err = |x_0 - x_{new}| \tag{4.5}$$

The value of tof is computed using either Lagrange, Battin or Lancaster formula Izzo (2014) depending on the value of x. Fig.4.5 shows a case where the iterations take place using Lancaster formula. The tof equation in this case is as follows:

$$tof = \frac{(x - \lambda z - \frac{d_{lan}}{y})}{E} \tag{4.6}$$
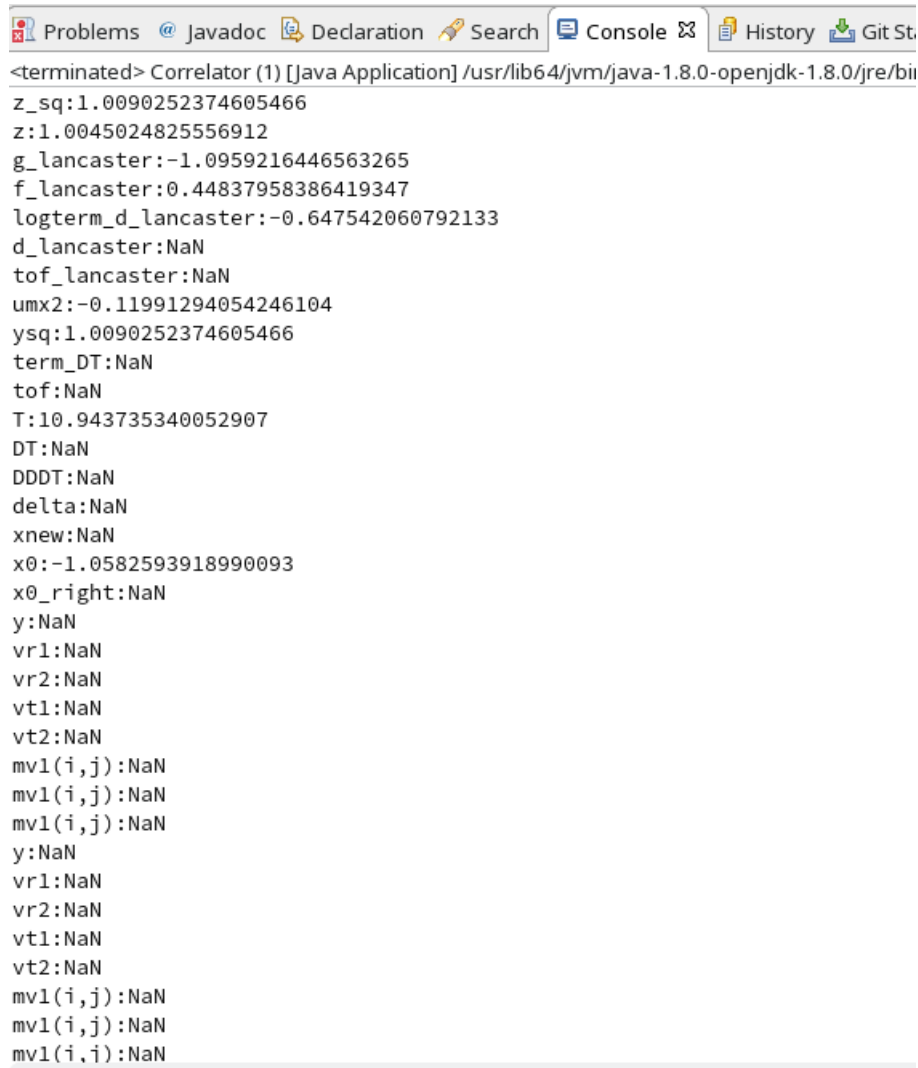
where d_{lan}, z, y and E are defined as

$$\begin{aligned} E &= x^2 - 1; \\ K &= \lambda^2; \\ z &= \sqrt{1 + KE}; \\ y &= \sqrt{|E|}; \\ d_{lan} &= \log(f + g); \\ f &= y(z - \lambda x); \\ g &= xz - \lambda E. \end{aligned} \tag{4.7}$$

The screenshot in Fig.4.5 shows that $(f + g) < 0$, which makes $d_{lan} = $ NaN. NaN standing for not a number, is a member of a numeric data type that can be interpreted as a value that is undefined such as the result of 0/0. This subsequently leads towards the failure to compute a value of tof. The values of velocity are not computed and one

does not get a solution for the initial orbit. Since this Lambert algorithm assumes an unperturbed geometry, it gives wrong/unexpected values which makes the algorithm fail in some cases.

3. Divergence due to Lambert solution being far from perturbed solution: If a full failure does not occur as shown in the previous case, there will still be some differences from the real solution because of the presence of perturbations. The difference between the Lambert solution and the real solution mainly depend on the time-of-flight (number of revolutions) between the two tracklets and the AMR value.


```
z_sq:1.0090252374605466
z:1.0045024825556912
g_lancaster:-1.0959216446563265
f_lancaster:0.44837958386419347
logterm_d_lancaster:-0.647542060792133
d_lancaster:NaN
tof_lancaster:NaN
umx2:-0.11991294054246104
ysq:1.0090252374605466
term_DT:NaN
tof:NaN
T:10.943735340052907
DT:NaN
DDDT:NaN
delta:NaN
xnew:NaN
x0:-1.0582593918990093
x0_right:NaN
y:NaN
vr1:NaN
vr2:NaN
vt1:NaN
vt2:NaN
mv1(i,j):NaN
mv1(i,j):NaN
mv1(i,j):NaN
y:NaN
vr1:NaN
vr2:NaN
vt1:NaN
vt2:NaN
mv1(i,j):NaN
mv1(i,j):NaN
mv1(i,i):NaN
```

Fig. 4.5 – An example showing a case where the Lambert algorithm fails for a highly perturbed orbit.

In some cases the function values are modified when a different propagator is used to propagate the states from the first tracklet's epoch to the second. An example is shown Fig.4.6, where the function values are plotted using Keplerian and numerical propagators for the same ρ_1, ρ_2. This could be another reason why the Newton-Raphson method didn't work well in the Shooting IOD with initial value from the Lambert solution. Since the
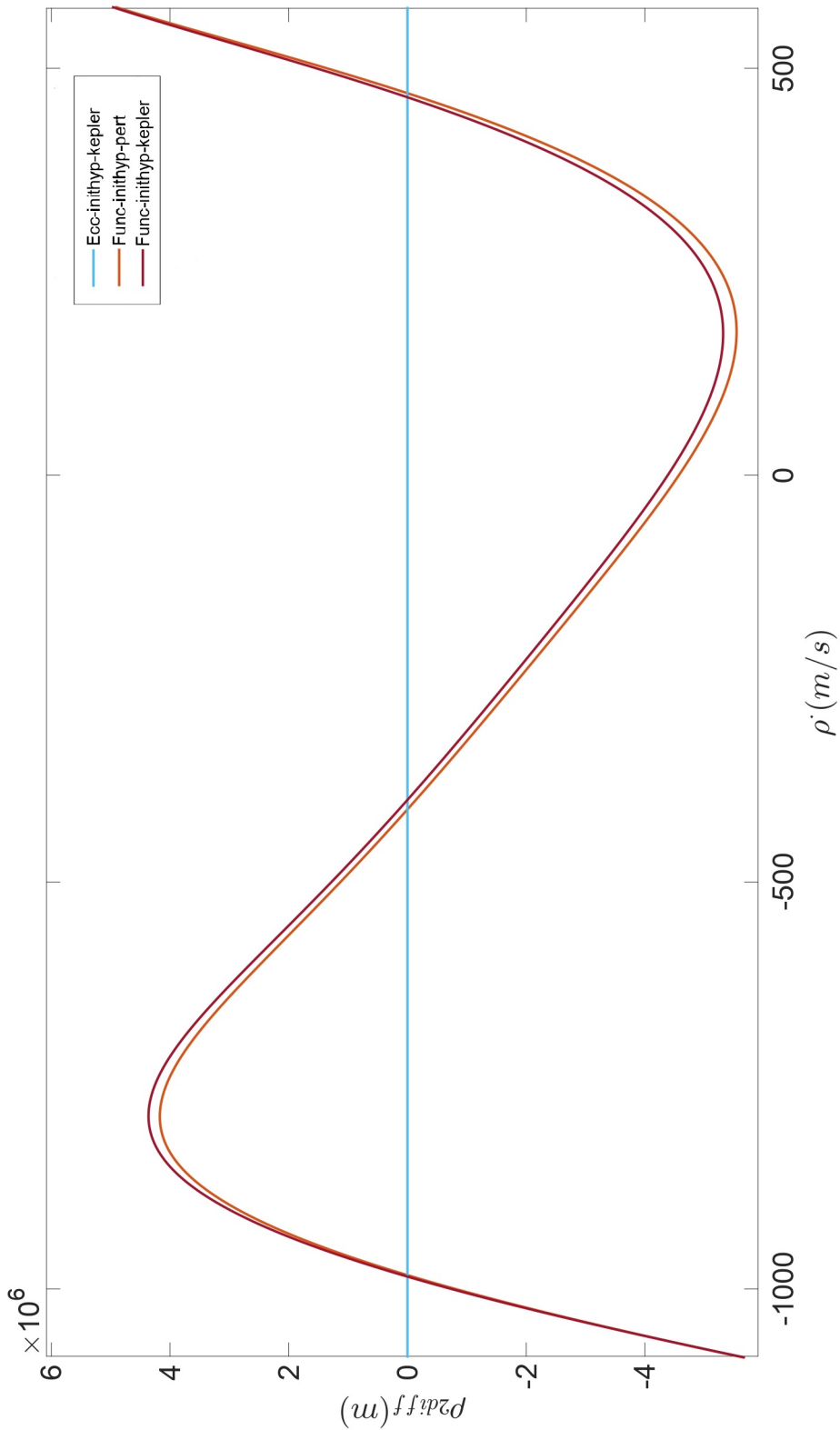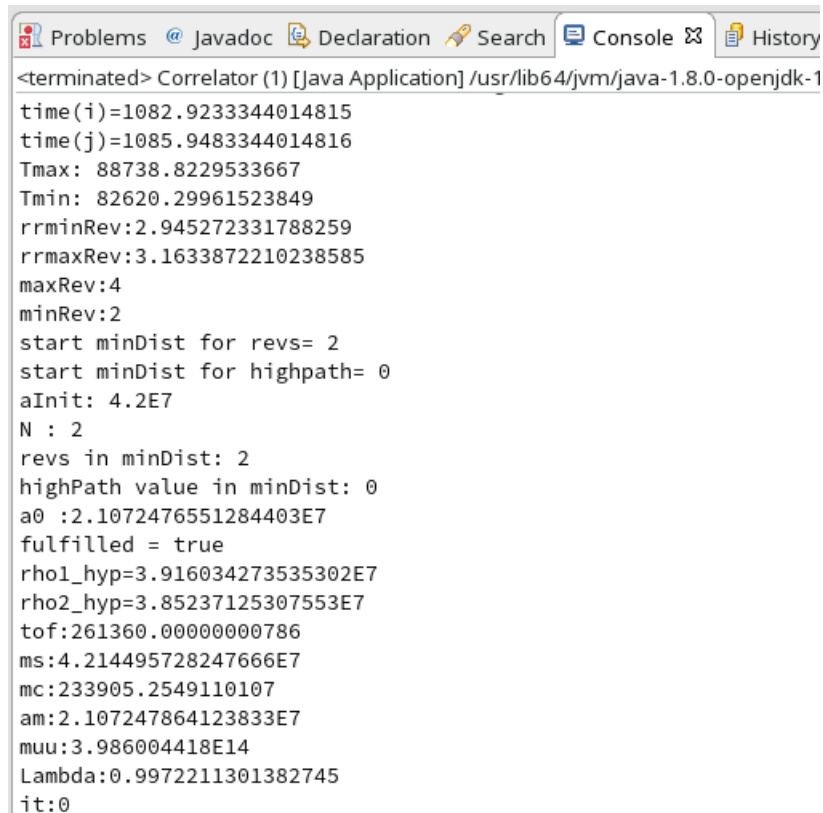
Fig. 4.6 – Function plot for the same ρ pair with Keplerian and numerical propagator.

function values using a Keplerian propagator or the numerical propagator are different, it would lead to slightly different values of roots. Since the Newton-Raphson method is very sensitive to even small changes in the initial values, it would mean that the algorithm couldn't converge in such cases.

4.2.4 Improvements in Shooting-OBVIOD

The previous sections showed the limitations of the Shooting-OBVIOD when using the unperturbed Lambert solution as initial value for Newton-Raphson method. The possible improvements considering various limitations are outlined here.

The solution in Shooting-OBVIOD has to be computed for all the possible numbers of revolutions. While solving the Lambert problem, each number of revolutions has two possibilities: high energy path and low energy path. For multiple revolutions, the number of possible scenarios could go up to a high number (6 in the case of 3 revolutions). The number of scenarios to be computed depends on the minimum and the maximum number of revolutions resulting from the maximum and minimum value of the semimajor axis allowed. Fig.4.7 shows such a case where solutions will be searched for 2, 3 and 4 revolutions for both highpath and lowpath scenarios. This number could be reduced by applying further constraints to the admissible region or by changing how each possible solution of Lambert's problem is followed.


```
Problems  @ Javadoc  Declaration  Search  Console  History
<terminated> Correlator (1) [Java Application] /usr/lib64/jvm/java-1.8.0-openjdk-1
time(i)=1082.9233344014815
time(j)=1085.9483344014816
Tmax: 88738.8229533667
Tmin: 82620.29961523849
rrminRev:2.945272331788259
rrmaxRev:3.1633872210238585
maxRev:4
minRev:2
start minDist for revs= 2
start minDist for highpath= 0
aInit: 4.2E7
N : 2
revs in minDist: 2
highPath value in minDist: 0
a0 :2.1072476551284403E7
fulfilled = true
rho1_hyp=3.916034273535302E7
rho2_hyp=3.85237125307553E7
tof:261360.00000000786
ms:4.214495728247666E7
mc:233905.2549110107
am:2.107247864123833E7
muu:3.986004418E14
Lambda:0.9972211301382745
it:0
```

Fig. 4.7 – An example showing a case when the Shooting-OBVIOD with Newton-Raphson will have to search through six possible solutions based on number of minimum and maximum revolutions.

The root finding method needs to be changed from Newton-Raphson to another method that is better for global convergence. It would be beneficial to use a method that doesn't fail if the function has multiple roots, which is the case in multiple revolution scenarios. Furthermore, the method should not depend on the initial value from Lambert's algorithm, which was the reason for failure in some cases.

4.3 Bisection method

Newton-Raphson method might have convergence issues if the initial estimate is far from the solution. In order to avoid such scenarios, a different root finding algorithm is needed which is more reliable in terms of convergence. Bisection is one such method, thus it is used to replace the Newton-Raphson method inside the Shooting IOD. It works by searching for the point where the function changes its sign. The interval containing the root needs to be identified to begin the search.

An interval based on the admissible region (constraining the semi-major axis) for our problem is chosen. A root lies in the interval (a, b) if $f(a)$ and $f(b)$ have opposite signs. The function is evaluated at the interval's midpoint and its sign is examined. The midpoint is used to replace whichever limit has the same sign. After each iteration, the bounds containing the root decrease by a factor of two. If after n iterations, the root is known to be within an interval of size ϵ, then after the next iteration it will be within an interval of size $\epsilon/2$. The iterations are carried out until the function value is below tolerance.

If the function is continuous, in case of a sign change at least one root must lie in that interval (the intermediate value theorem)(Russ, 1980). If the function is discontinuous, but bounded, then instead of a root there might be a step discontinuity which crosses zero (see Fig.4.9).

If the interval happens to contain two or more roots, bisection will find one of them. If the interval contains no roots and merely straddles a singularity, it will converge on the singularity. The different scenarios mentioned are shown in Fig.4.8, 4.9, 4.10 and 4.11 (Press et al., 1992).
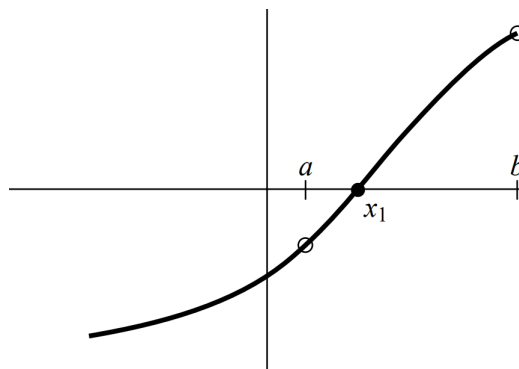

Fig. 4.8 – The figure shows an isolated root x_1 bracketed by two points a and b at which the function has opposite signs.
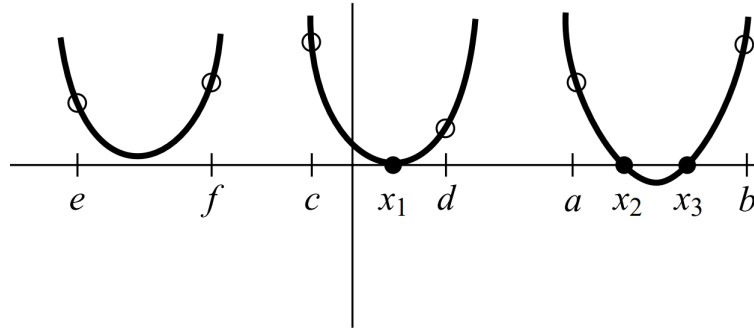
Fig. 4.9 – The figure illustrates that there is not necessarily a sign change in the function near a double root (in fact, there is not necessarily a root!).
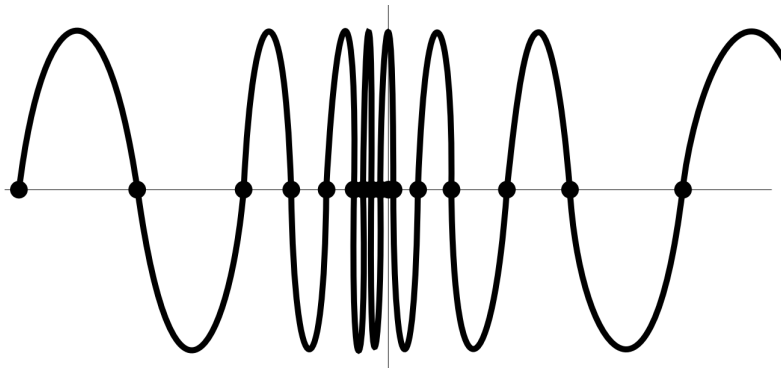
Fig. 4.10 – Example of a pathological function with many roots.
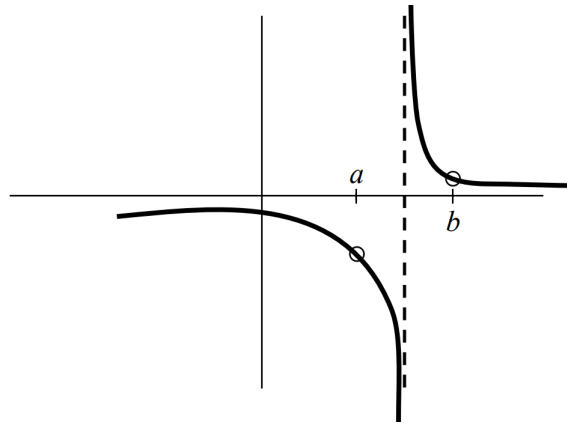
Fig. 4.11 – The function has opposite signs at points a and b, but the points bracket a singularity, not a root.

4.3.1 The Shooting algorithm function

If one is given a function in a black box, there is no sure way of bracketing its roots, or of even determining that it has roots. An example of a function plot was made for $(\rho_{2j} - \rho_2)$ for an initial OBVIOD hypothesis (ρ_1, ρ_2) in case of three revolutions and AMR 10 m^2/kg. Fig.4.12 illustrates two points (A, B) on the function, which constitute the boundary of an interval that contains three roots. The function inside the Shooting algorithm is $\rho_{2j} - \rho_2$ (j is the iteration number in the Shooting IOD) as mentioned in the section above. This

is referred to as ρ_{2diff} in the figure and the mid-point of the (A, B) interval is C. Another case of 3 revolutions and AMR 10 m^2/kg for a different pair of tracklets and (ρ_1, ρ_2) an extended function plot was made. The possible $\dot{\rho}$ values for a geostationary orbit were first used to compute the function values and then extended to higher magnitudes of $\dot{\rho}$ where the function diverged. The plot is shown in Fig.4.13 below. The function is continuous with multiple roots. As seen in the introduction, the bisection method could be used for this type of function. Since the function has multiple roots, it will need to be divided into various intervals (also called brackets) in order for bisection algorithm to find all the roots in the desired intervals.

Fig. 4.12 – Function plot between an interval A and B.
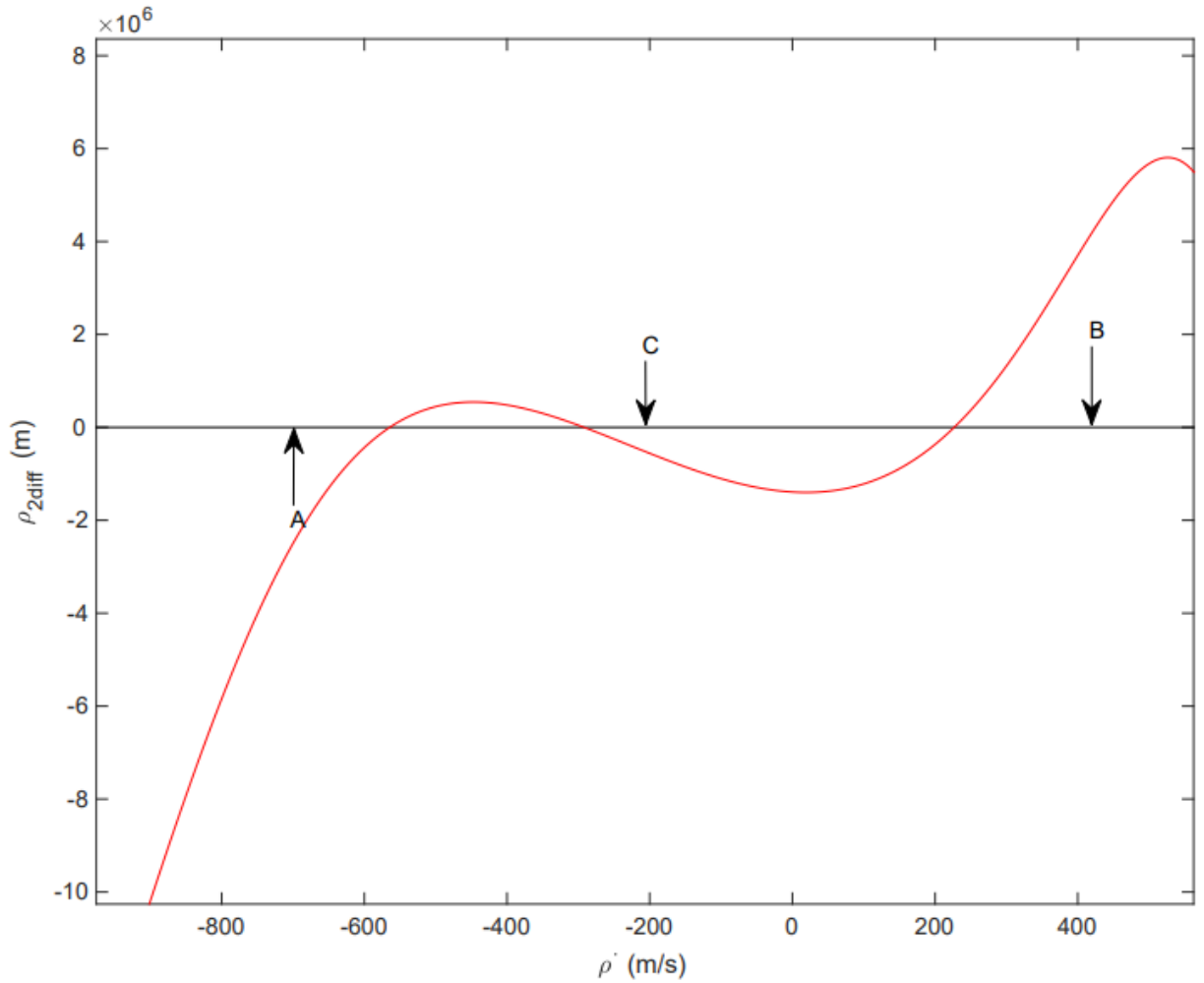
Constraints for Brackets in Bisection

Brackets are searched in the admissible region defined by the semimajor axis, between 41,000 km and 43,000 km. The orbital velocity expression from the vis-viva equation is:

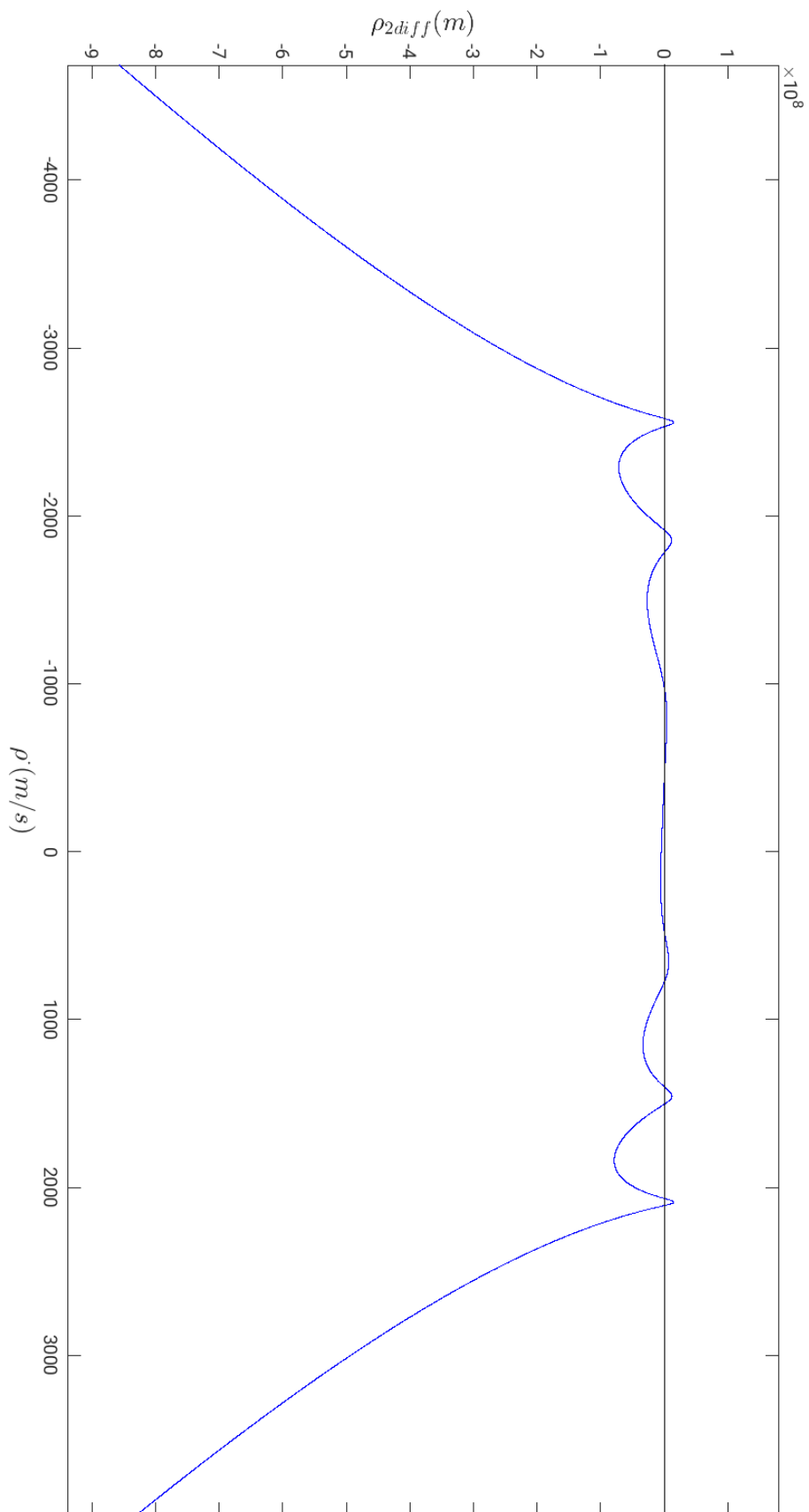$$v^2 = GM\left(\frac{2}{r} - \frac{1}{a}\right) \tag{4.8}$$

Fig. 4.13 – Function plot made by varying $\dot{\rho}$ values for a given ρ_1, ρ_2.

If the maximum semimajor axis value (43,000 km) is substituted in the above quadratic equation, one gets two roots for the velocity. The geocentric position and velocity as a function of ρ, $\dot{\rho}$ can be expressed as:

$$r(\rho) = \overrightarrow{r_s} + \rho\,\overrightarrow{u} \tag{4.9}$$

$$v(\rho, \dot{\rho}) = \overrightarrow{v_s} + \rho\,\dot{\overrightarrow{u}} + \dot{\rho}\,\overrightarrow{u} \tag{4.10}$$

The information about $\overrightarrow{r_s}$ and $\overrightarrow{v_s}$ (station position and velocity) is available. $\overrightarrow{u}$ is the line of sight vector and $\dot{\overrightarrow{u}}$ is its rate of change. The only unknown in Eq.(4.10), $\dot{\rho}$ can be computed using velocity values one gets from the constraints. Using the values from the semimajor axis constraints, one obtains a quadratic in range-rate. Rearranging Eq.(4.8) and using Eq.(4.10), one gets

$$a = \frac{rGM}{2GM - r(\dot{\rho}\,\overrightarrow{u} + \rho\,\dot{\overrightarrow{u}} + \overrightarrow{v_s})^2}. \tag{4.11}$$

The roots of this quadratic will correspond to the bounds of our function by inserting respective a values. For the minimum value or maximum value of semimajor axis either zero, one or two values of $\dot{\rho}$ can be obtained depending on the function. The $\dot{\rho}$ values corresponding to the semimajor axis minimum or maximum are used as the starting brackets for the bisection method. Point C in the Fig. 4.12 corresponds to the semimajor axis minimum on the $\dot{\rho}$ axis and points A and B correspond to the maximum.

Intervals containing multiple roots are separated into smaller brackets. This will be done in cases similar to Fig. 4.12 where there is more than one root in the A,B bracket. Since there are odd number of roots, a sign change is noticed in the function value from A to B. However, when the search begins between the midpoint C and A there is no change in the function sign, which could mean no root or even number of roots in the interval. The interval A,C is again divided into two to make sure no roots were missed in either of the halves. In the end, the final number of brackets are established each containing a single root. In this particular case there will be three. All of them are searched for roots using bisection method and once found need to be filtered in the OBVIOD algorithm to choose the solution for a given pair of tracklets.

Similarly eccentricity can be expressed using the geocentric position, velocity and semimajor axis as:

$$e = \sqrt{1 - \frac{(\overrightarrow{r} \times \overrightarrow{v})^2}{\mu a}}. \tag{4.12}$$

Once one substitutes the value of a from Eq.(4.11) and values of $\overrightarrow{r}$ and $\overrightarrow{v}$ in terms of ρ, $\dot{\rho}$ one obtains a quartic equation in $\dot{\rho}$. The solution to the quartic equation was comparatively difficult to calculate, contrary to the semimajor axis relation. Hence, only the latter was used to define function bounds. The Eq.(4.12) also shows that for every value of semimajor axis we will have two values of eccentricity, with only one exception of minimum value of semimajor axis.

The eccentricity and semimajor axis are plotted separately with respect to $\dot{\rho}$ for the same object whose function plot is shown in Fig. 4.13. The eccentricity plot (Fig. 4.15) shows
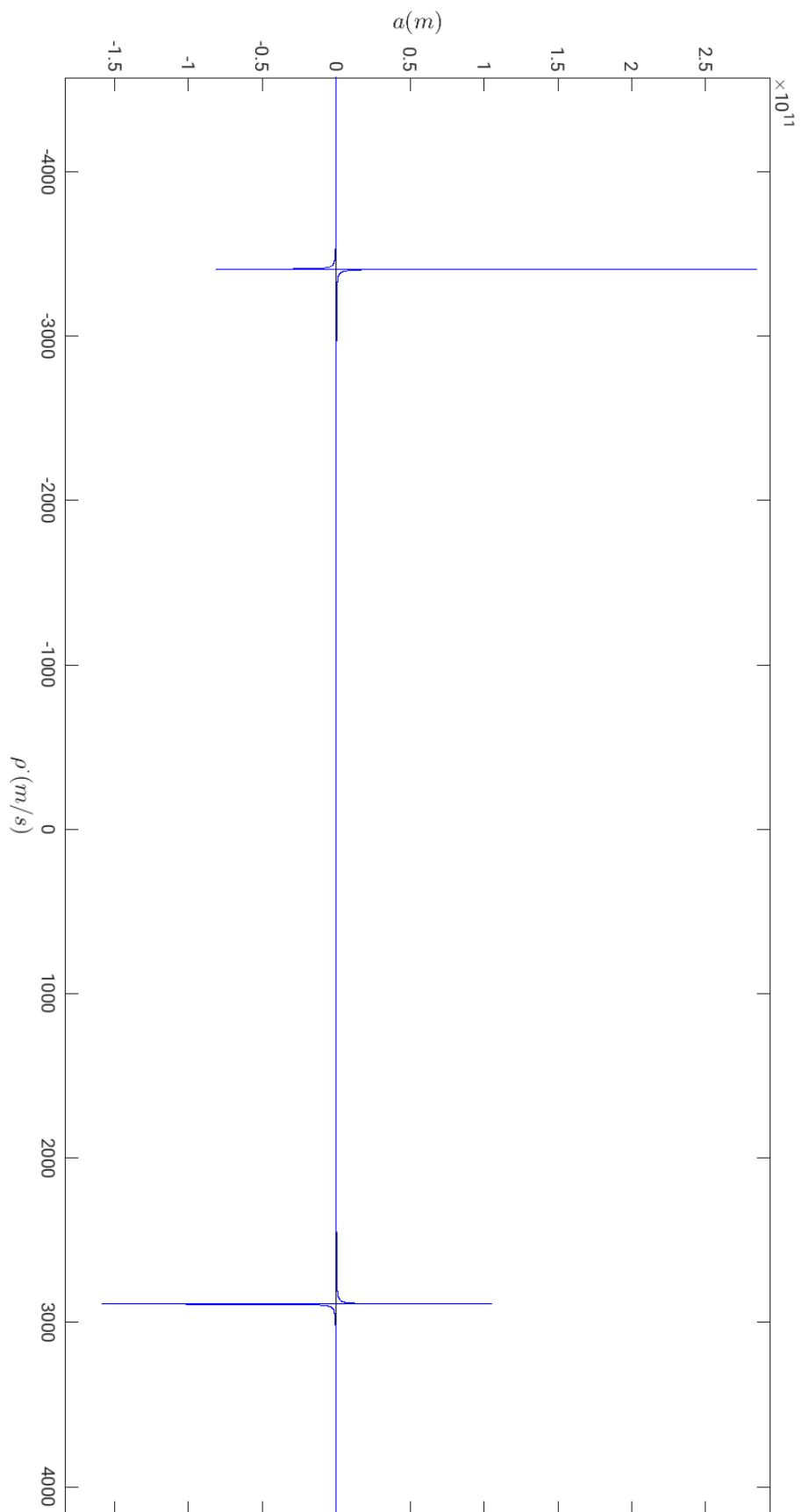
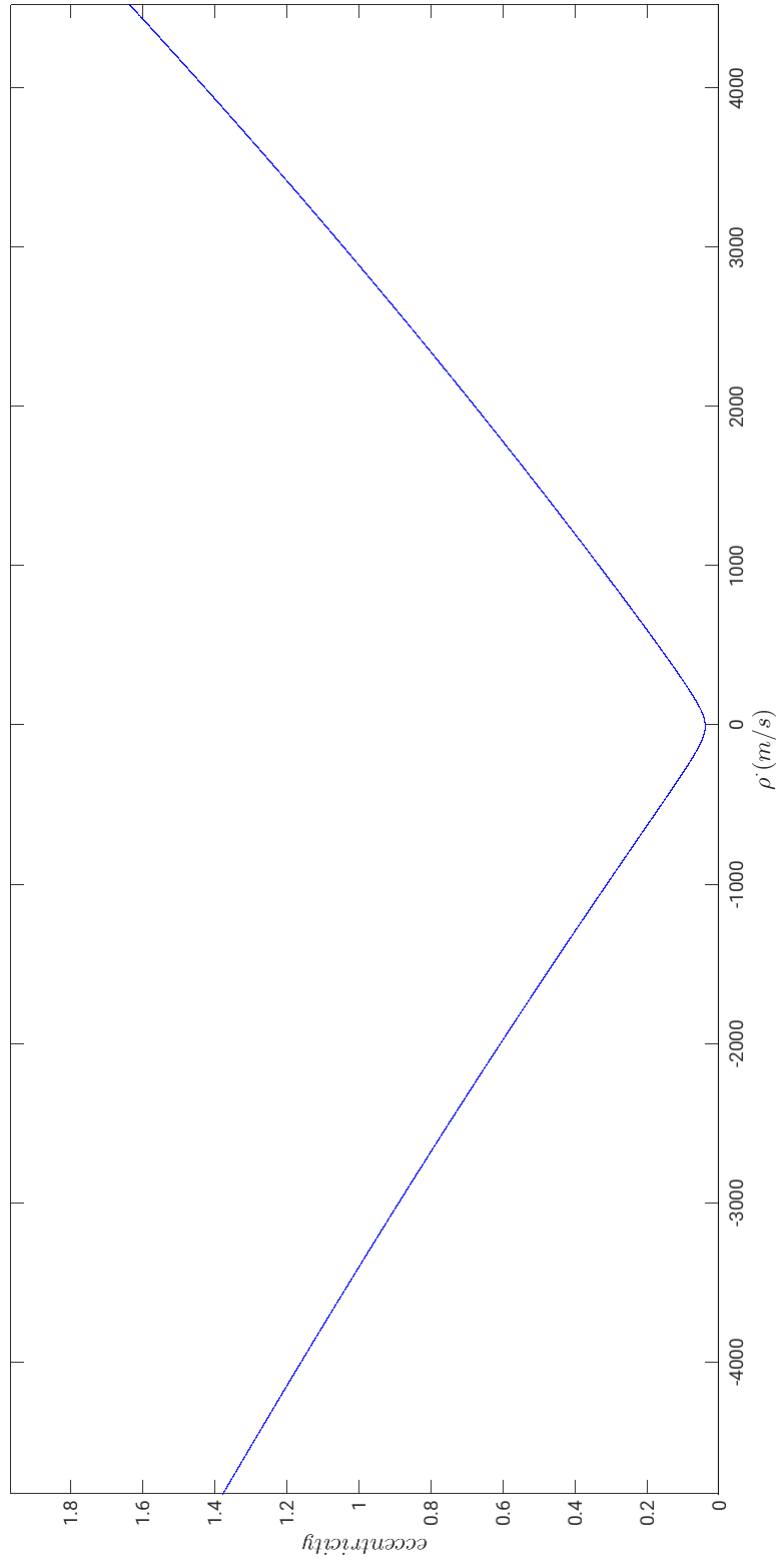**Fig. 4.14** – semimajor axis values plotted against the $\dot{\rho}$ values.

Fig. 4.15 – Eccentricity values plotted against the $\dot{\rho}$ values.

that there are hyperbolic solutions ($e > 1$) for higher magnitudes of $\dot{\rho}$ and elliptical solutions for smaller values. This is also reflected in the semimajor axis plot (Fig. 4.14) where one can see hyperbolic solution ($a < 0$) for some values of $\dot{\rho}$. The elliptical solutions of semimajor axis can be seen for some lower values of $\dot{\rho}$ which also include the semimajor axis limits used to define the brackets in bisection. The semimajor axis plot is zoomed in to show what happens at high values of $\dot{\rho}$, the semimajor axis values increase sharply and finally go below zero (see Fig. 4.16). The semimajor axis plot for elliptical orbits is shown in Fig. 4.17. The e vs a plot is shown as well for the elliptical orbits, one can see that there are two solutions for eccentricity for every value of a (Fig. 4.18).
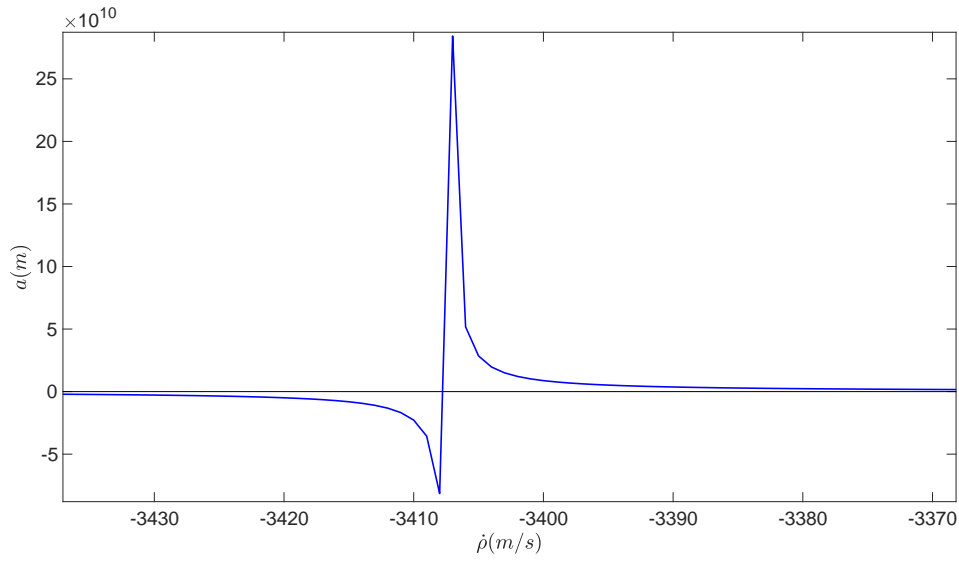

Fig. 4.16 – Semimajor axis plot zoomed between $\dot{\rho}$ values of $(-3500, -3400)$ to show the transition from elliptical to hyperbolic orbits.
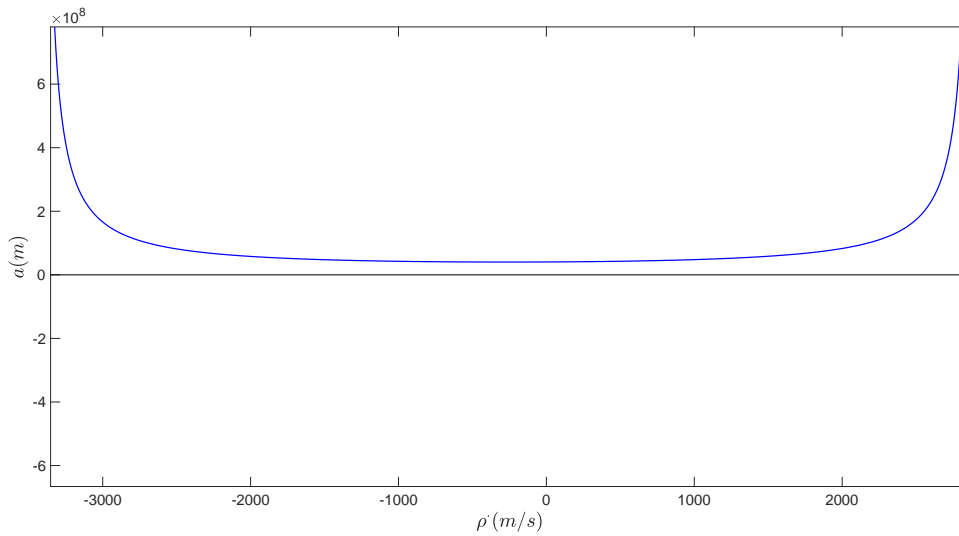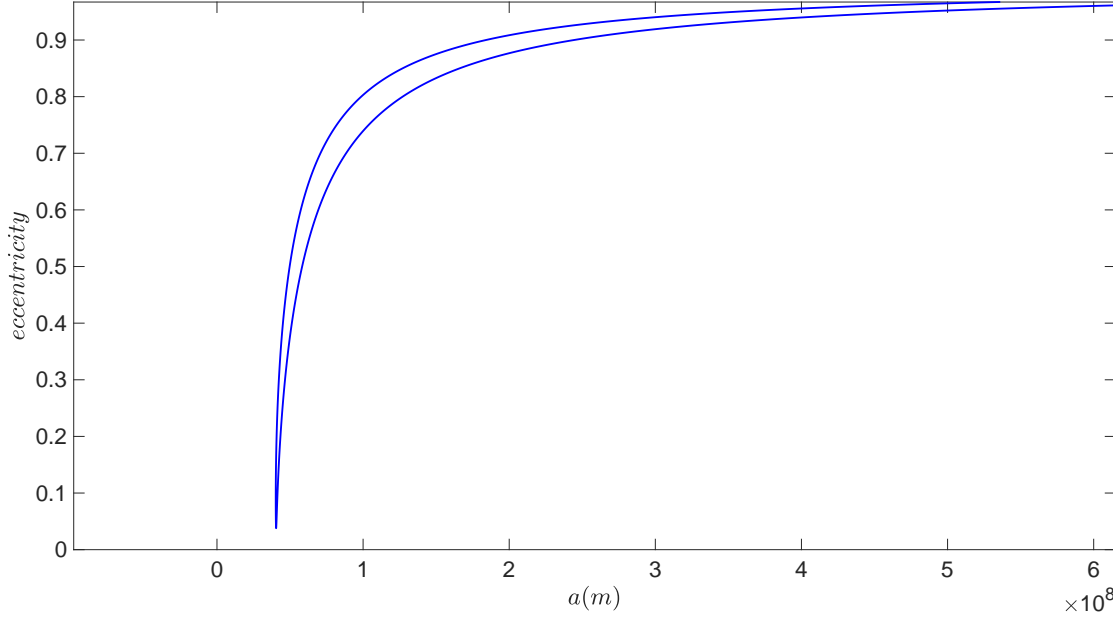
Fig. 4.17 – Semimajor axis plot for lower values of $\dot{\rho}$ where the orbits are elliptical.

Fig. 4.18 – Eccentricity vs semimajor axis plot showing two values of eccentricity for every value of semimajor axis except for the minimum energy orbit.

4.3.2 Bisection-Shooting

The constraints mentioned in the previous section are used to find the bounds of the function (also referred to as brackets). The principal brackets interval resulting from the semimajor axis maximum and minimum value are searched for roots. The basic bisection strategy is followed and the change of sign of the function is noted. After defining the brackets, they are followed one by one to search for the roots. The value of $\dot{\rho}_1$ is updated in the consecutive iterations by moving towards the mid-point of a bracket.

This can be illustrated using the interval shown in Fig. 4.12. In order to search for a root inside C,B the $\dot{\rho}_1$ value will move inside ρ_{1C} and ρ_{1B} by examining the sign at the midpoint of the new interval (assuming it to be D). The latter can be calculated using the relation below.

$$\dot{\rho}_{1D} = \dot{\rho}_{1C} + \frac{(\dot{\rho}_{1B} - \dot{\rho}_{1C})}{2} \tag{4.13}$$

After computing the root from a given bracket, it is followed in the iterations in the BFGS. The root finding takes place for each iteration until all of them are exhausted or the minimum gradient is reached. If a loss function minimum is found, that particular solution from a given bracket is accepted. Otherwise, the next bracket is followed and the same procedure is repeated, until the solution is found, each bracket is followed one by one starting from the positive value of $\dot{\rho}$ corresponding to the a_{max} root.

The $\dot{\rho}_1$ root depends on the ρ_1 value which changes through different iterations. Hence the size of the brackets changes as well. The strategy adopted in those cases is to take the root from the adjacent bracket (the one which was not searched before).

The values of α_2 and δ_2 are not used in the Shooting IOD. These values could be used along with ρ_2. However, the resulting differences in state at epoch 2 would be positive or null because they will be computed for the vectors and vector difference's magnitude is always positive. Since the strategy in Bisection method works by detecting the change in sign of the functions, this was not possible. Consequently, only the difference between ρ_2 computed in the Shooting method and ρ_2 from OBVIOD was used.
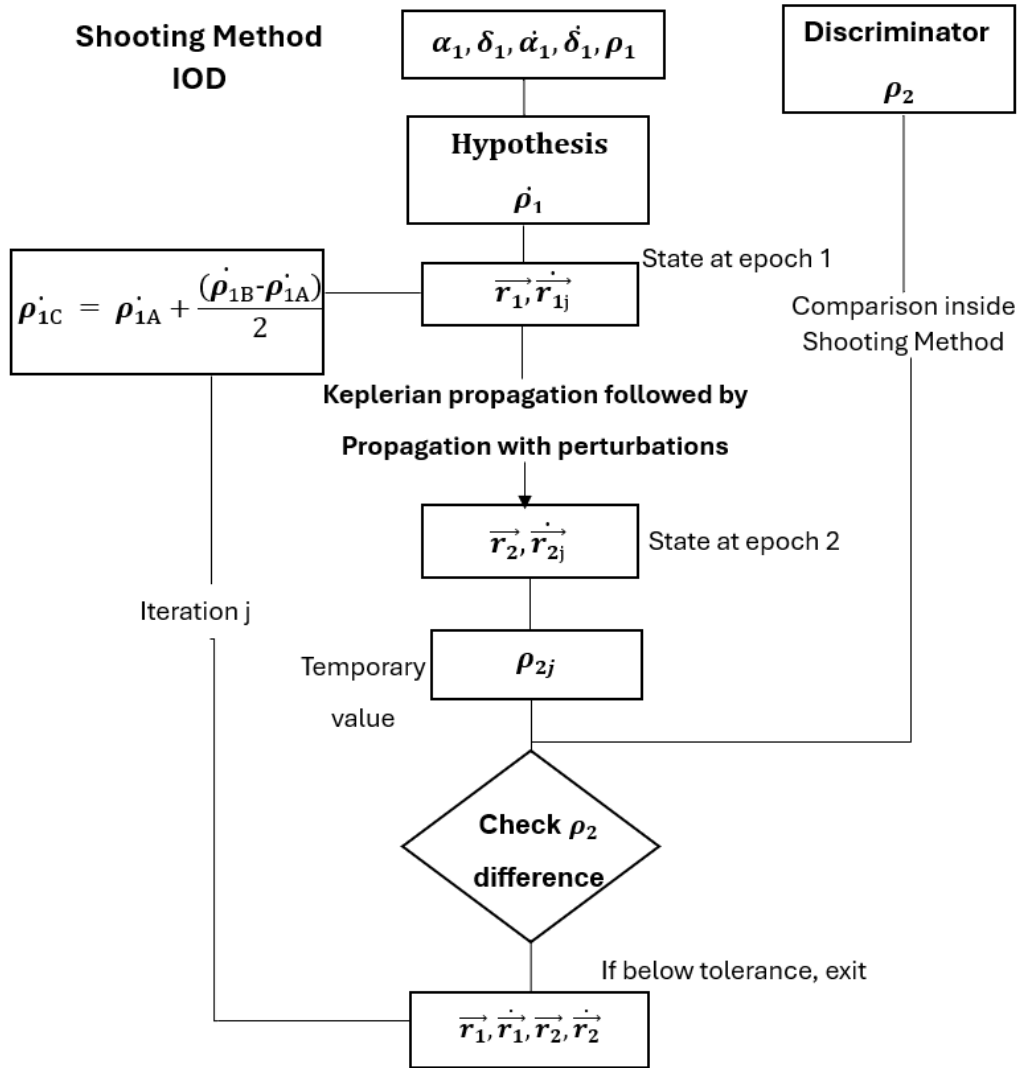

Fig. 4.19 – Process flow in Bisection-Shooting IOD.

The values of α_2 and δ_2 are used in the final discriminator of Shooting-OBVIOD in one of the versions of Bisection-Shooting OBVIOD. The structure of the latter is given in subsection 4.3.3.

Minimum semimajor axis constraint

The value of semimajor axis was constrained between values 41,000 km and 43,000 km as mentioned in Section 4.3.1. In some cases the minimum of the semimajor axis function is greater than 41,000 km. So the constraint was modified in order to accommodate different situations. The minimum of the function is calculated and if it is below 41,000 km then this value is chosen as the minimum to start brackets else the function minimum itself is chosen to define the brackets.

Examples are shown for two of the objects tested. In Fig. 4.20 the minimum of a is more than the minimum set for constraints. The $\dot{\rho}$ value corresponding to the minimum a is the starting point for Bisection brackets. In Fig. 4.21 the minimum of a is less than the minimum set for constraints. In such cases, the semimajor axis constraint value of 41,000 km is used to define the brackets. This will result in two values of $\dot{\rho}$ for the minimum a. These values along with the $\dot{\rho}$ values corresponding to the maximum a are used to define the brackets.

Fig. 4.20 – Semimajor axis vs $\dot{\rho}$ plot showing minimum value higher than the chosen admissible region minimum.

Use of brackets

The $\dot{\rho}_1$ root depends on the ρ_1 value which may change during different iterations. Hence the size and number of brackets change as well. The brackets are always searched one by one starting from one of the two values of $\dot{\rho}$ corresponding to the semimajor maximum. The numbering of brackets starts from the first interval containing root between $\dot{\rho}_{amin}$ and $\dot{\rho}_{amax}$

(positive value). The description of brackets originating from the admissible region is shown in Fig. 4.21 for a given object and (ρ_1, ρ_2).

In the original OBVIOD algorithm, the number of possible solutions could go up to six for a case of three revolutions. The admissible region used in Bisection and definition of brackets reduces the number of possible solutions to be computed. This is essential when the numerical propagation is expensive in terms of time especially in multi-revolution scenarios.
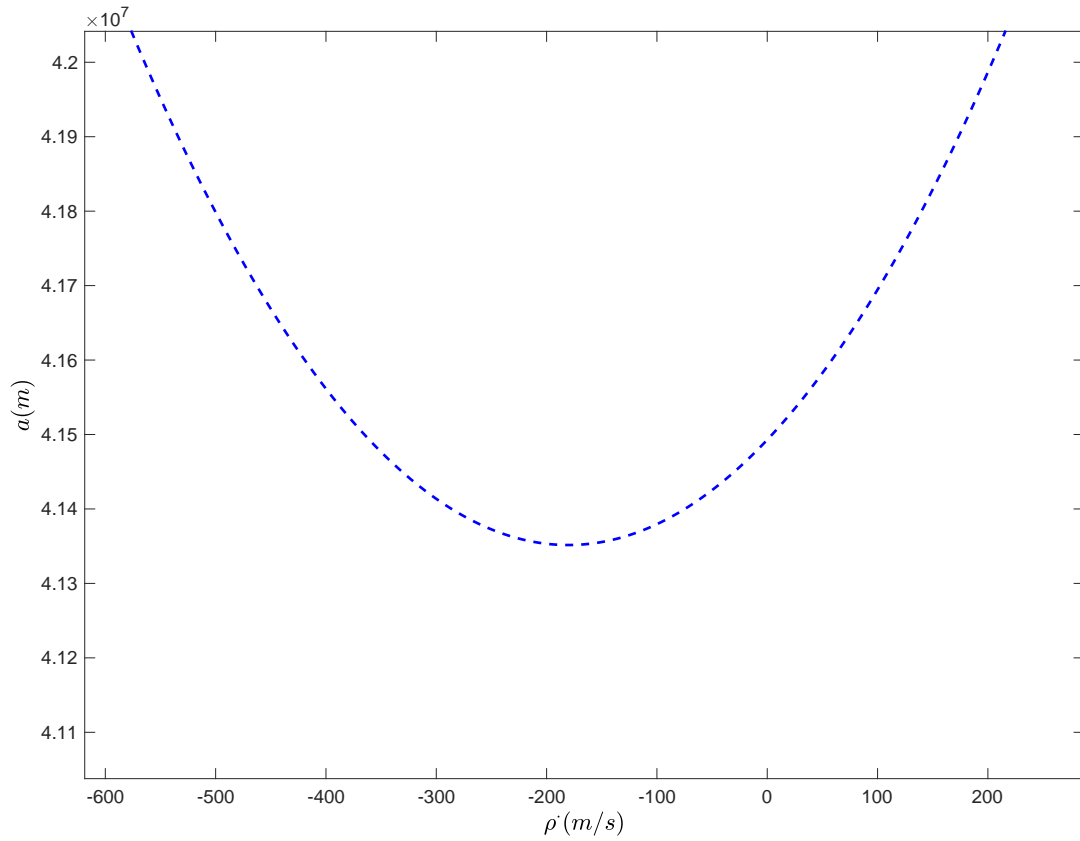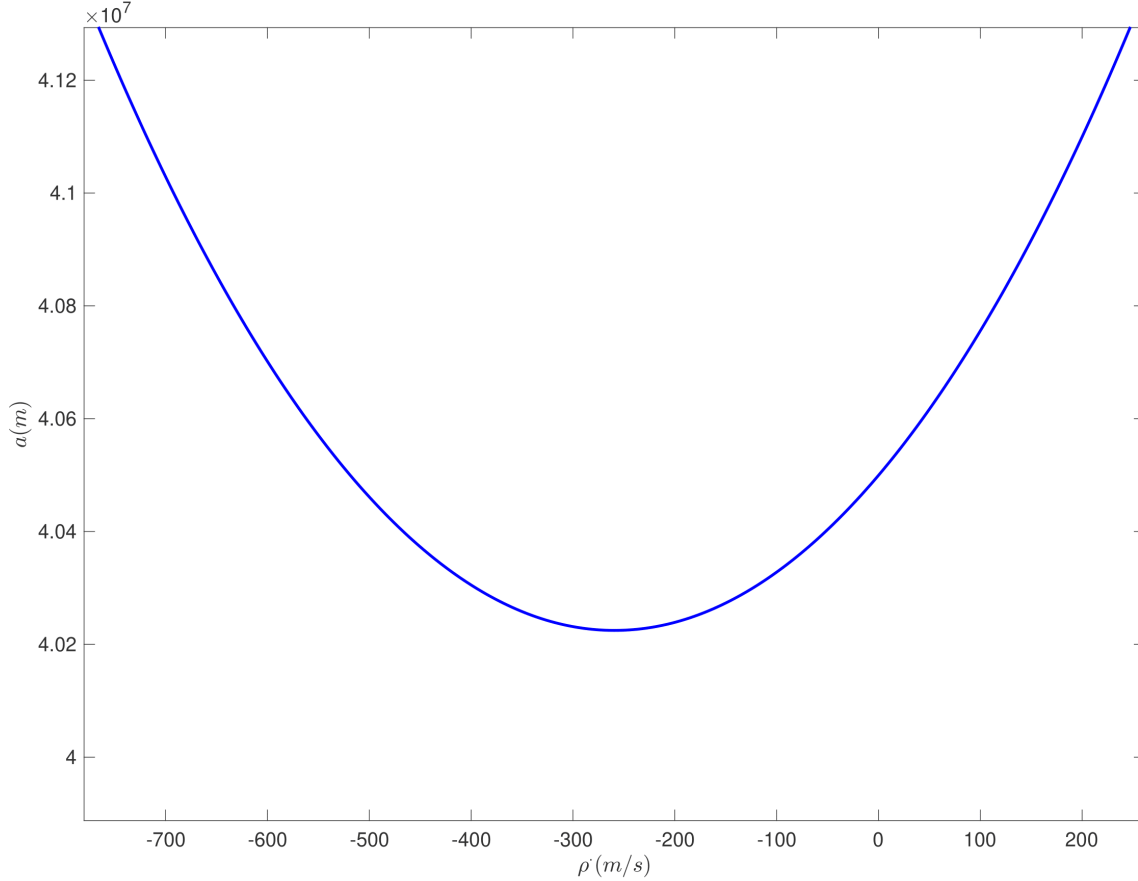

Fig. 4.21 – Semimajor axis vs $\dot{\rho}$ plot showing minimum value lower than the chosen admissible region minimum.

In case the bracket being followed disappears because there is no root in that interval anymore for a (ρ_1, ρ_2), the root is searched in the next bracket. This is achieved by awarding a serial number to the brackets. An example of number of brackets reducing from one ρ pair to another is shown in Fig. 4.22. The number of roots in the admissible region reduces from two to one.

Hence, the serial number of the bracket is being followed rather than strict values of $\dot{\rho}$. For example from the Fig. 4.22 one can note that the bounds of one bracket shift from (-200, 550) to (-200, 200) and so on.

Sometimes there is no root in a bracket. This can happen when a ρ_1, ρ_2 pair does not correspond to the $\vec{u_1}$, $\dot{\vec{u_1}}$, $\vec{r_s}$ and $\vec{v_s}$. In such a case a different combination of ρ_1 and ρ_2 should be considered. This is handled by varying the ρ_1 by steps to widen the bracket until there is a root in the bracket. The OBVIOD algorithm uses the admissible region approach to set ρ_1 and ρ_2 thresholds. The ρ_1 value can be varied to search for roots until the threshold.
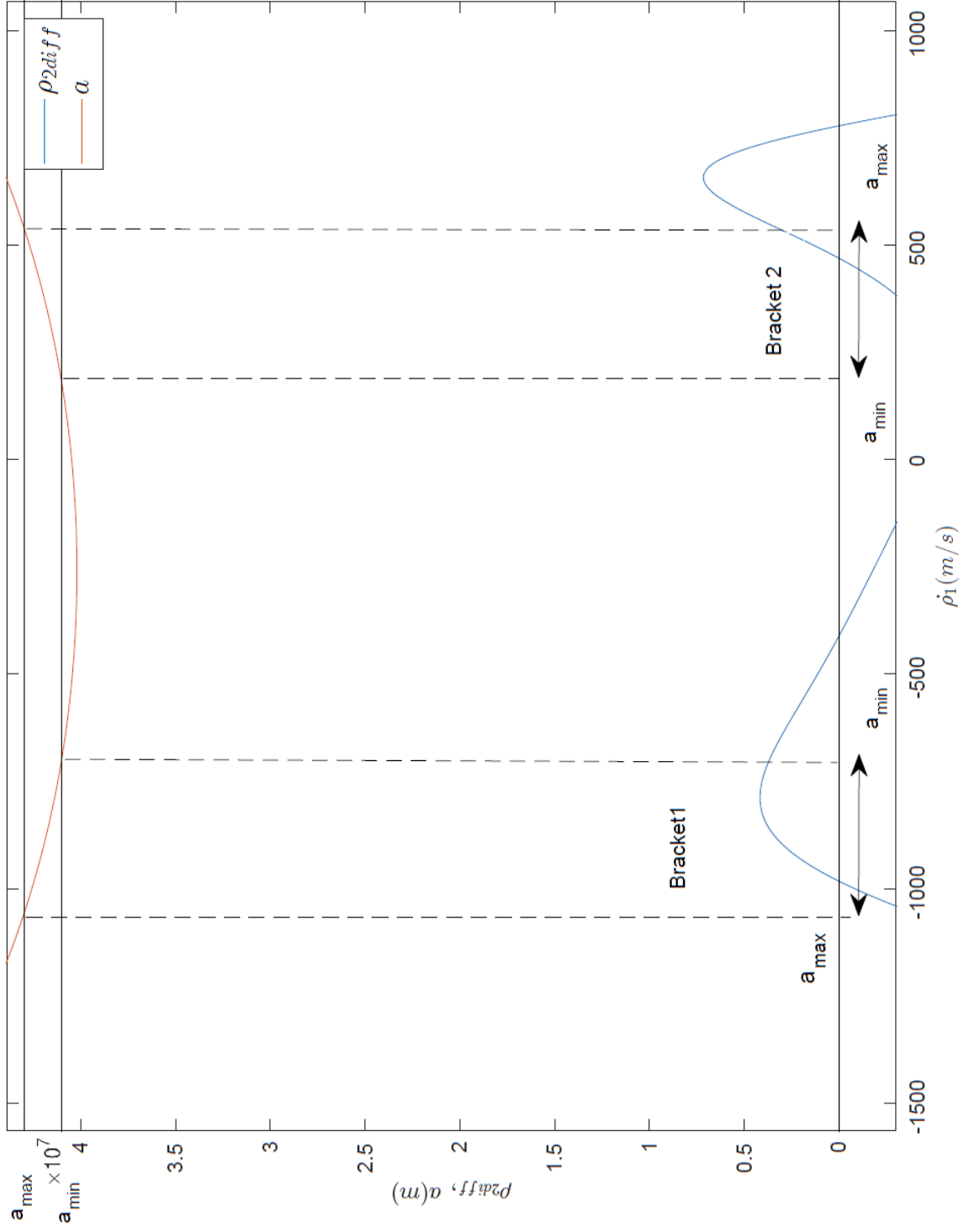
Fig. 4.22 – Brackets are defined for a function based on the admissible region bounds chosen for semimajor axis. The second bracket has one of its boundaries at $\dot{\rho} \approx 600$ m/s. It corresponds to the point of intersection of a curve at a_{max}. The second boundary of Bracket 2 lies at $\dot{\rho} \approx 200$ m/s. It corresponds to the point of intersection of a curve at a_{min}. The same is true for Bracket 1.

Fig. 4.23 – The number of brackets and their limits changed with a new ρ pair which lead to different a_{max}.

In these cases, the semimajor axis quadratic Eq.(4.11) used to find $\dot{\rho}_1$ values for a_{amin} and a_{max} does not give a result as the determinant is negative (imaginary $\dot{\rho}$) or sometimes, it gives $\dot{\rho}_1$ for a_{amin} and a_{max} but with no roots inside that interval. The screenshot in Fig. 4.23 shows such a case where the algorithm fails to fin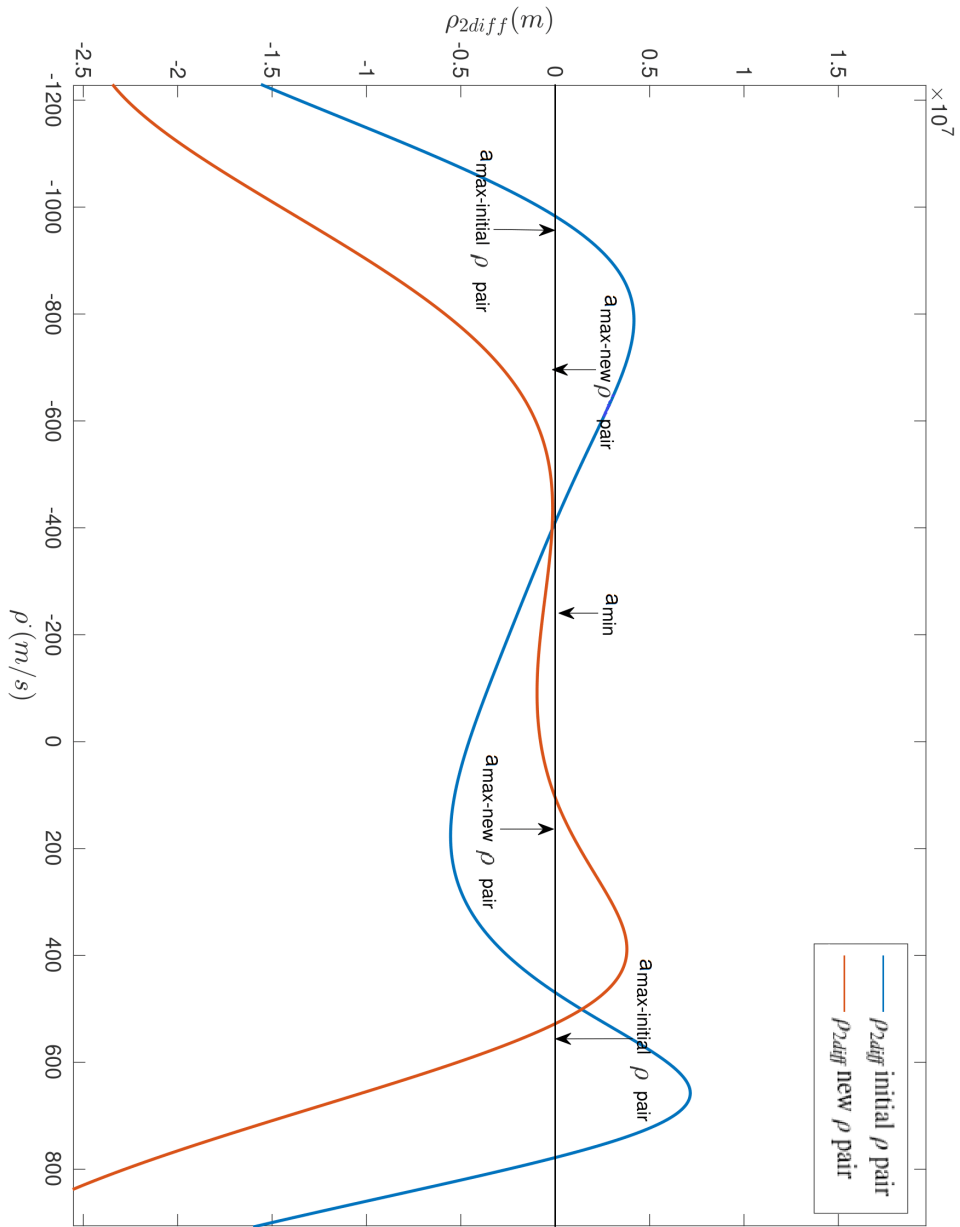d the bounds containing a root and the value of ρ_1 needs to be modified until one gets an interval with valid values.

```
bracket1_root1amax[1]:0.0
bracket2_root1amax[0]:0.0
bracket2_root1amax[1]:0.0
bracket3_root1amax[0]:0.0
bracket3_root1amax[1]:0.0
bracket4_root1amax[0]:0.0
bracket4_root1amax[1]:0.0
bracket1_root2amax[0]:0.0
bracket1_root2amax[1]:0.0
bracket2_root2amax[0]:0.0
bracket2_root2amax[1]:0.0
bracket3_root2amax[0]:0.0
bracket3_root2amax[1]:0.0
bracket4_root2amax[0]:0.0
bracket4_root2amax[1]:0.0
```

Fig. 4.24 – Example of a scenario where the semimajor axis bounds are not found from the quadratic equation due to a certain value of ρ_1.

4.3.3 The Bisection-Shooting OBVIOD versions

There are two versions of the Bisection-Shooting OBVIOD algorithm with two different sets of discriminators. Chapter 3 showed how the change of free parameters to ρ_1, ρ_2 lead to a more optimal function topography and hills, valleys disappeared for a given interval of revolutions. In the versions of the algorithm with Bisection-Shooting for IOD, the same hypothesis variables (ρ_1, ρ_2) are used. This pair of variables provides the advantage of a more favorable search space than $\rho_1, \dot{\rho}_1$. Once the range hypothesis is made, this pair enters the Shooting scheme where the $\dot{\rho}$ hypothesis is made in order to determine the orbit for a given ρ pair. The Mahalanobis distance is computed using $(\alpha_2, \delta_2, \dot{\alpha}_2, \dot{\delta}_2)$ as the discriminator inside BFGS algorithm in the one version of the algorithm and using $(\dot{\alpha}_1, \dot{\delta}_1, \dot{\alpha}_2, \dot{\delta}_2)$ in the other version. The angular positions are used as a part of the discriminator in the first version of algorithm because they are not used in the Shooting IOD.
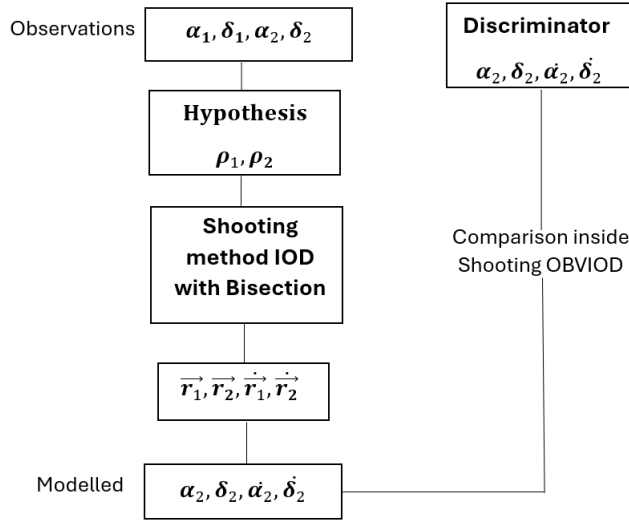
Fig. 4.25 – Process flow in the first version of the Bisection-Shooting OBVIOD with angular positions and rates at the second epoch as the discriminator.

The discriminator in the first version makes the Shooting-OBVIOD algorithm similar to the initial value orbit determination algorithm. However, due to the change of iteration variables from $\rho_1, \dot{\rho}_1$ (initial value algorithm) to ρ_1, ρ_2 in BFGS, the function topography is kept optimal. The schematic of this version is shown in Fig. 4.25 and the second version in Fig. 4.2. The only difference between the two is the discriminator.

The flow control procedures and other optimization constraints used to enhance performance of Newton-Raphson Shooting OBVIOD (mentioned in 4.2) were used for the Bisection Shooting OBVIOD as well. The details about different constraints and parameters used inside the algorithm are mentioned below:

1. Limit on minimum stepsize: The linesearch iterations taking place in the minimum gradient search algorithm (BFGS) continue until a decrease in the function value is noted for a particular step. The values of ρ_1, ρ_2 are modified using a variable step size. The latter continues to decrease and was limited to 1 centimeter as mentioned in section 4.2, this value is kept in the Bisection-Shooting OBVIOD.

2. Number of iterations in BFGS: The new number of iterations was chosen after testing various cases of revolutions and AMR for correlation performance. It was made sure that the number of iterations did not limit the whole algorithm from making correlations. On the other hand, this number could be modified if the parameters in the functioning of the algorithm are changed somehow or if an unforeseen case with a particular number of revolutions and/or AMR value is tested in the future.

3. Divergence in Shooting: Flow control was used inside Shooting algorithm to prevent iterations in case the magnitude of instantaneous function value ρ_{2diff} is increasing rather than converging to the minimum. The Bisection-Shooting IOD uses admissible region bounds for semimajor axis and computes brackets containing roots of the function. A divergence scenario was not encountered and algorithm is shielded from it. Hence, the condition was not needed and removed for Bisection-Shooting IOD.

4. Hessian matrix reset limit: The number of times Hessian matrix can be reset is limited so that in cases where the BFGS function is stuck near a ρ_1, ρ_2, the time is not wasted and one can either jump to processing the next bracket or the processing will finish if the bracket was the last in line.

5. The first bracket that gives MD below the threshold is chosen and the rest of the brackets are not looked for a solution because of time constraints.

The Function topography

The loss function topography for OBVIOD was analysed by Siminski et al. (2013a) in order to find a strategy for minimization. The loss function topography provides insights to the function behavior. Some of the tests involved a pool of an hour long tracklets from which one pair didn't correlate. However, the same tracklet pair of 7 minutes length or lower correlated. The behavior of the hour long tracklet pair was investigated by using the loss function topography for the second version of Bisection-Shooting OBVIOD, it can be seen in Fig. 4.26. This version uses $(\dot{\alpha}_1, \dot{\delta}_1, \dot{\alpha}_2, \dot{\delta}_2)$ as the discriminator. The figure shows the path followed by the function during processing. It is visible that the path followed leads in the opposite direction to that of the actual solution region. The solution region is plotted as well and can be seen in Fig. 4.27, which shows the real solution. The long length of the tracklets prevented them from being correlated mainly because the linear model of attributables is not valid for such long tracklets. Moreover, the long tracklets separated by about three revolutions lead to higher uncertainty, and a good initial orbit is never computed.

The function topography of the same tracklet pair with 7 minutes length for the same version of Bisection-Shooting OBVIOD is shown in Fig. 4.28. The real solution is marked using a data point in the plot. The processing path leads one towards the correct solution and the tracklet pair is correlated.

The loss function topography in the $(\rho_1, \dot{\rho}_1)$ space is plotted for the first version of the algorithm, the one that uses $(\alpha_2, \delta_2, \dot{\alpha}_2, \dot{\delta}_2)$ as discriminator for the MD. The plot was made in order to investigate if this variable space is optimal for search, and has a clearly defined minimum. The plot was made for 7 minutes long tracklet pair and is shown in Fig. 4.29. The global minimum lies in the region with $2 <$ revolutions < 3. However it can be seen that for the same $\dot{\rho}_1$ bracket, one has a possibility to find minimum in either of the revolutions space. The second version of the algorithm performs slightly better in this respect for the cases investigated.
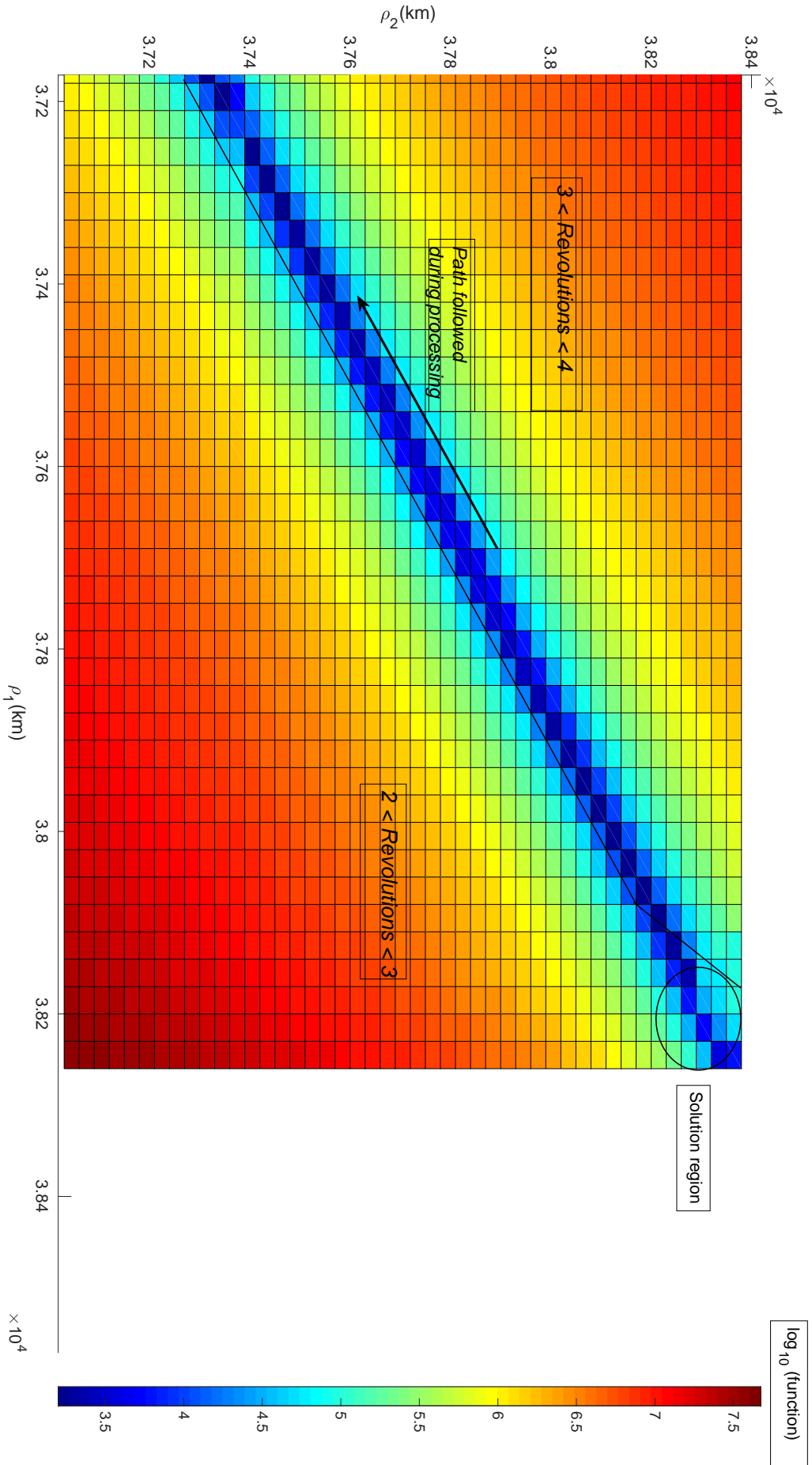
Fig. 4.26 – Loss Function topography for an hour long tracklet pair with the second version of Bisection-Shooting OBVIOD. The plot shows the regions with different number of revolutions, the path followed while processing, as well the real solution region.

Fig. 4.27 – The solution region for the same tracklet pair showing number of revolutions as well the function clearly.
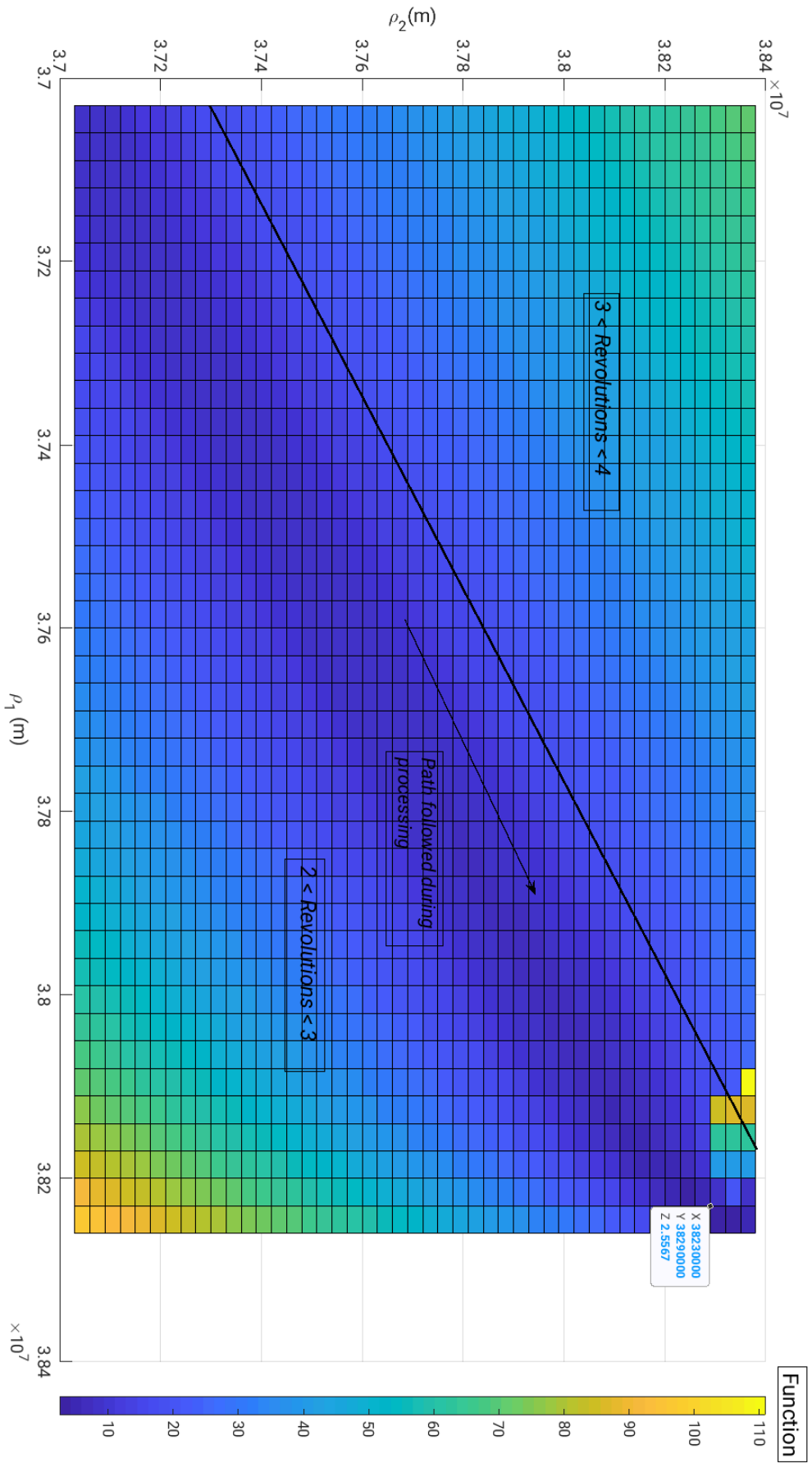
Fig. 4.28 – Function topography for the same tracklet pair with **7** minutes length using the second version of Bisection-Shooting OBVIOD. The plot shows the regions with different number of revolutions, the path followed while processing, as well as the real solution with a data point.
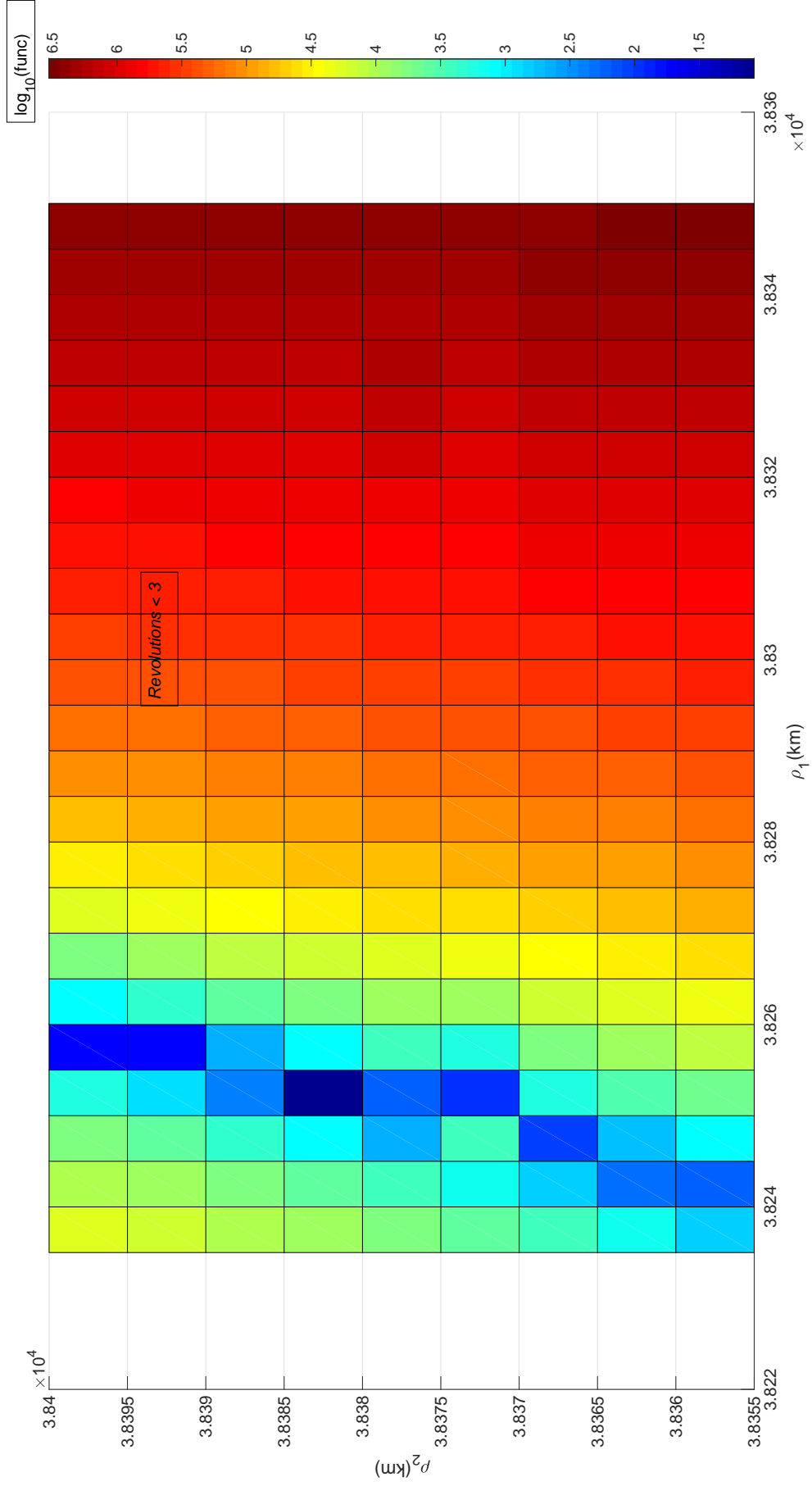
Fig. 4.29 – Function topography for a short length tracklet pair using the new discriminator. The plot shows the regions with different number of revolutions and the solution region.

5 Tests and Results

This chapter will show the results obtained with different versions of the OBVIOD algorithm. The following sections will discuss the reasons behind the specific results. The performance of the latest version of the algorithm will be s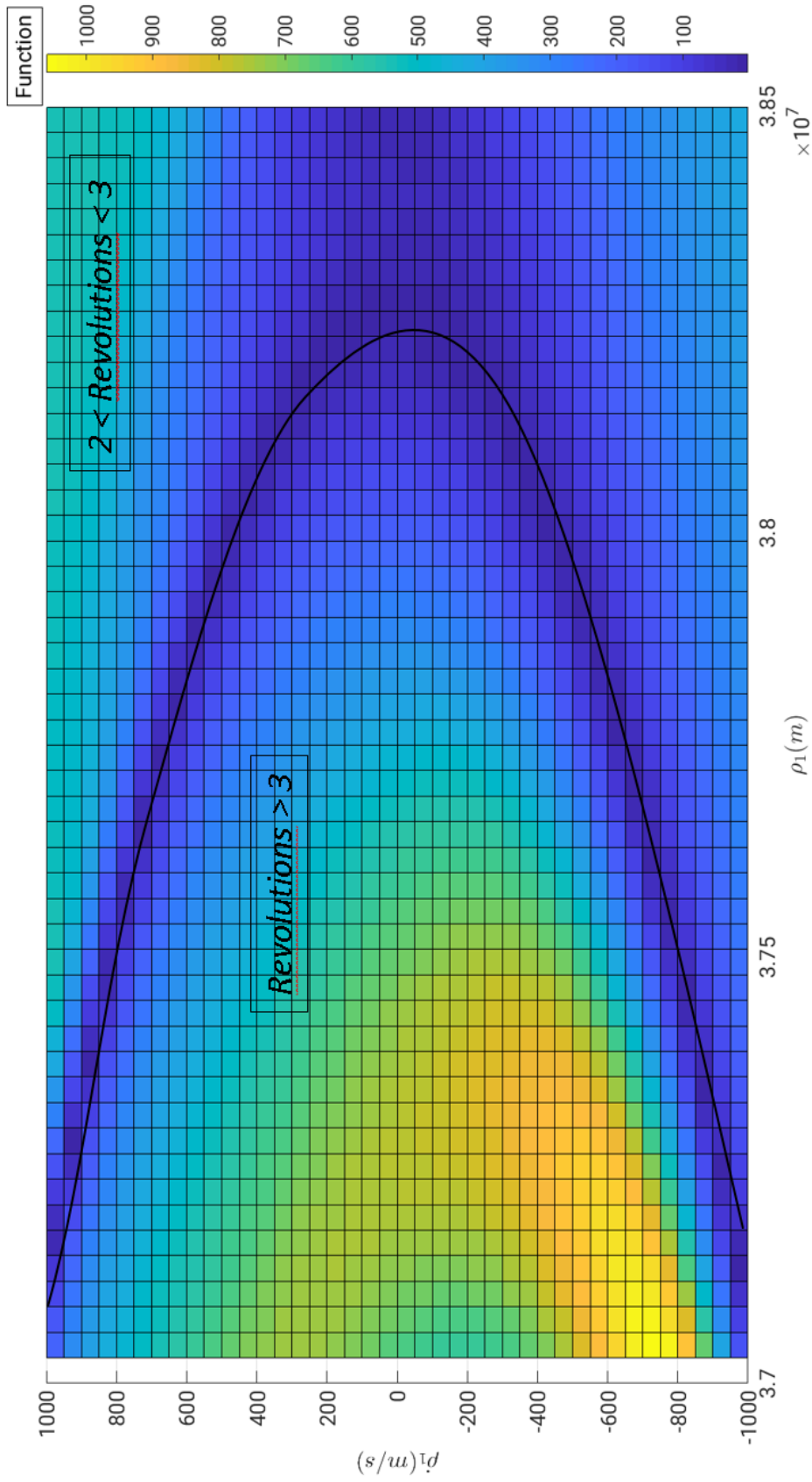hown with variation of several parameters for a set of tracklet pairs. In total more than 60 different tracklet pairs were tested.

5.1 Simulation of input files

The survey strategy consists of repeatedly scanning a declination stripe with a fixed right ascension. The declination interval is chosen as $\pm 8°$ for each right ascension. Observations were simulated using the Zimmerwald station coordinates to get topocentric angular positions over the length of 2 to 3 minutes. The TLEs used were extracted from Spacetrack (SPACE-TRACK, 2019) objects catalog. Perturbations were added for: geopotential terms, solar radiation pressure, third body attraction forces for Sun and Moon. In the following tests observations simulated for the GEO regime were considered. The constraints applied on different elements were: inclination < 10, eccentricity < 0.3, semimajor axis between 41,000 km and 43,000 km. Two tracklets are tested at a time. They are separated by a few hours, one, two or three revolutions in different cases. The Ω, ω and v are not constrained while simulating the observations. A normally distributed optical error of one arc second was added for all the observations.

5.2 Tests performed

5.2.1 Comparison between Newton-Raphson Shooting and unperturbed OBVIOD

This section shows results of the tests performed on a group of tracklets. The Newton-Raphson Shooting and the unperturbed OBVIOD are compared by varying the number of revolutions and AMR values. All the tests are done with different objects so as to increase the sample size. The number of tracklet pairs tested are still limited owing to the high computation time consumed by the numerical propagator used in Shooting-OBVIOD. The results are shown starting from Fig.5.1 to Fig.5.6.
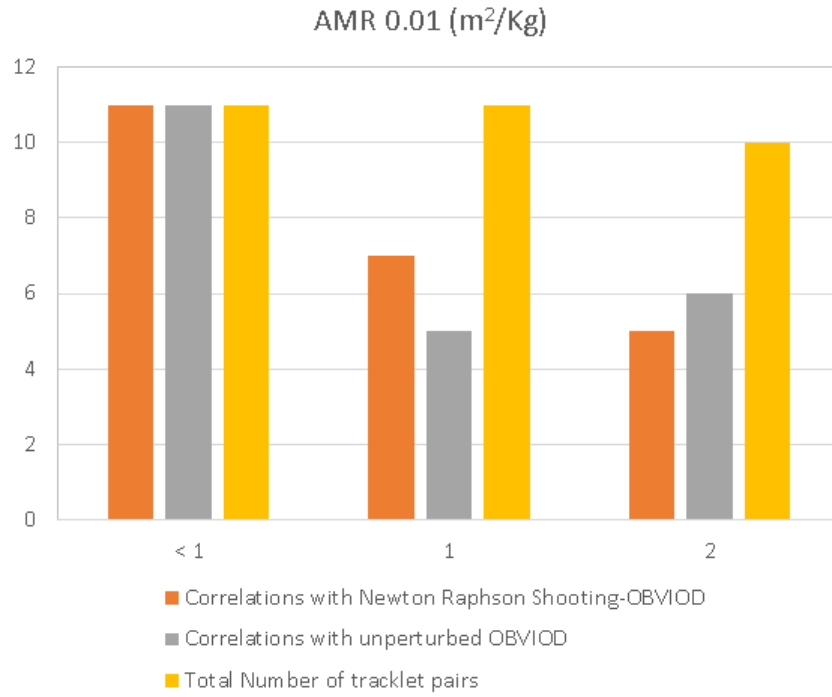
Fig. 5.1 – The number of revolutions are shown in the x-axis. For tracklet pairs separated by less than 1 revolution, the unperturbed OBVIOD and Newton-Raphson OBVIOD perform well. With increasing number of revolutions there is a fluctuation in the correlations made by these methods.
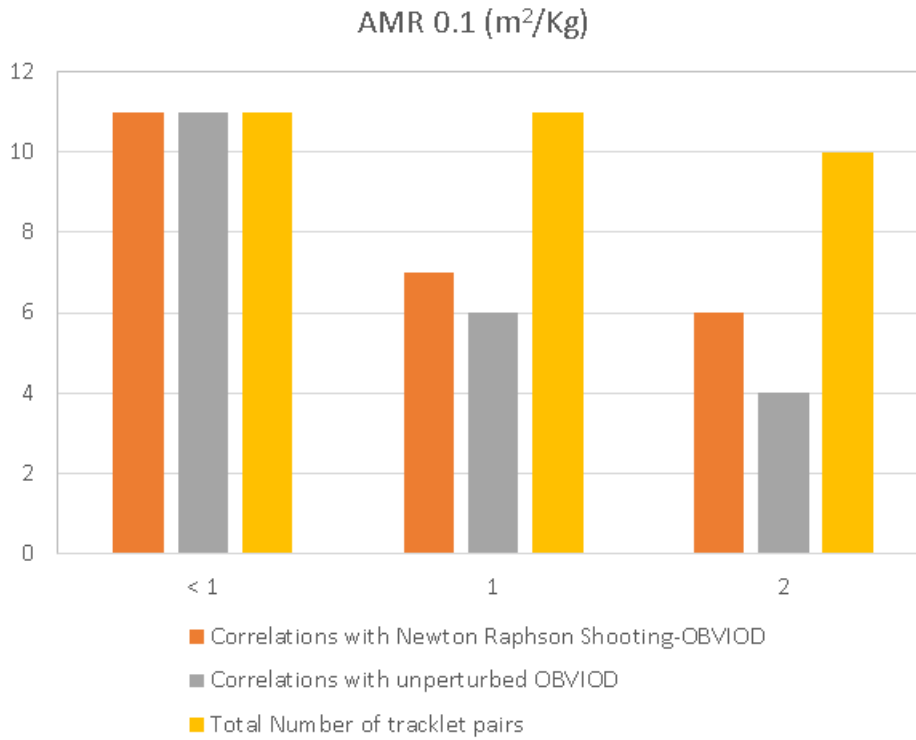
Fig. 5.2 – The number of revolutions are shown in the x-axis. With AMR of 0.1 m^2/Kg and increase in number of revolutions the Newton-Raphson method is slightly better than the unperturbed OBVIOD.
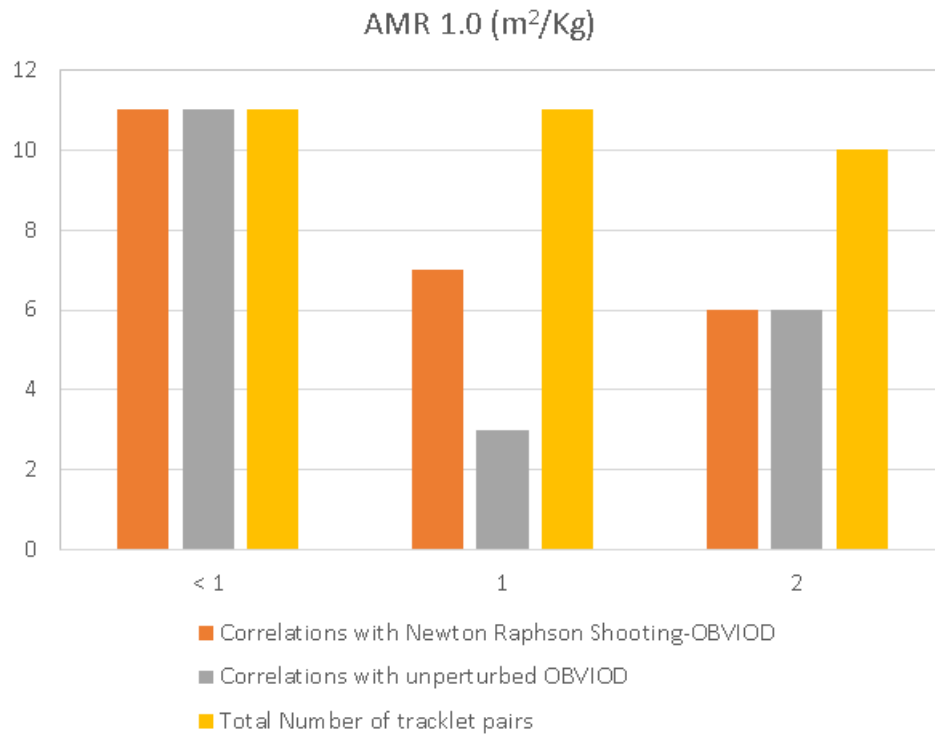
Fig. 5.3 – The number of revolutions are shown in the x-axis. In case of high AMR value and increasing number of revolutions the Newton-Raphson method performs equally well or better than the unperturbed OBVIOD.
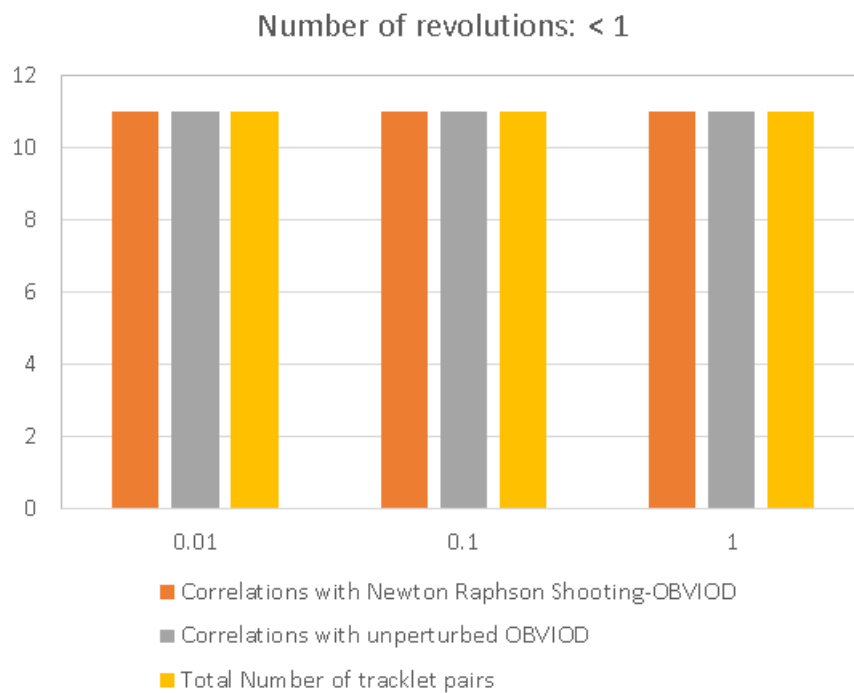
Fig. 5.4 – The AMR is shown in the x-axis. Neither unperturbed OBVIOD nor the Newton-Raphson OBVIOD miss any correlations for tracklet pairs separated by less than 1 revolution. This is true for any of the AMR values tested.
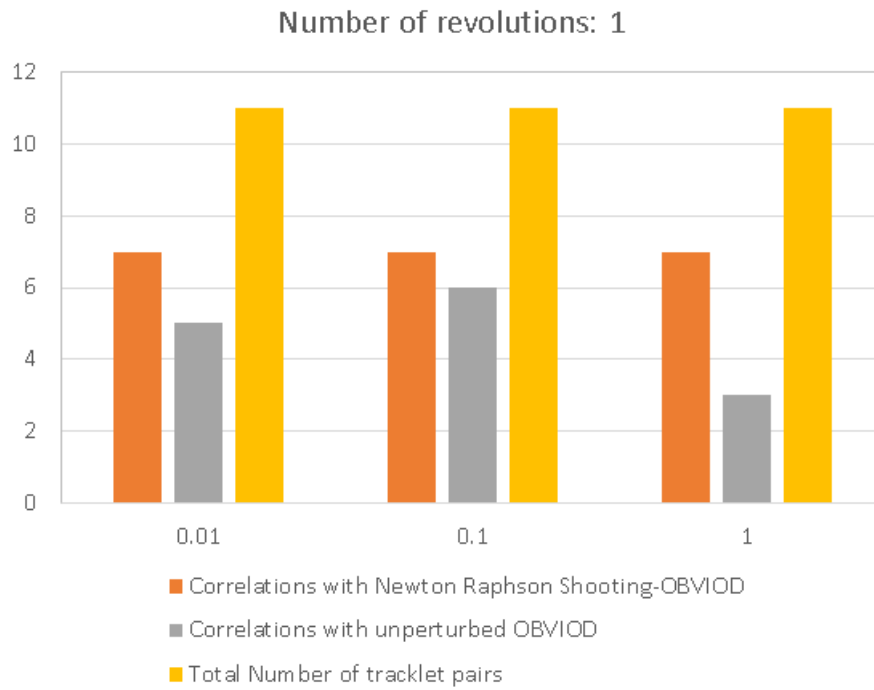
Fig. 5.5 – The AMR is shown in the x-axis. For tracklets one revolution apart the Newton-Raphson performs slightly better than the unperturbed OBVIOD.

Fig. 5.6 – The AMR is shown in the x-axis. The correlations for Newton-Raphson and unperturbed OBVIOD are shown for a given number of tracklets tested.

The variation of AMR values while keeping the number of revolutions constant and vice-versa gives an insight about the limitations of unperturbed OBVIOD and to what extent the Newton-Raphson Shooting-OBVIOD is able to overcome them.

The degradation of unperturbed OBVIOD results is evident for 1 or more revolutions (Fig.5.1, Fig.5.2 and Fig.5.3) and similarly for High-Area-to-Mass-Ratio (HAMR) objects (Fig.5.4, Fig.5.5 and Fig.5.6). This is expected because with increase in AMR and tof the perturbations have a higher impact, especially the solar radiation pressure.

The Table 5.1 below shows the summary of missed correlations for different number of revolutions with variation of AMR value. The missed correlations refer to the number of pairs that could not be associated together whereas they truly belong to the same object. It can be noticed that both the Newton-Raphson and the unperturbed OBVIOD miss some correlations for high AMR value, although this number is higher in case of the unperturbed OBVIOD than of Newton-Raphson Shooting-OBVIOD.

No. of Revolutions	AMR (m²/Kg)	Unperturbed OBVIOD	Newton Raphson Shooting-OBVIOD
< 1	0.01	0	0
1	0.01	6	4
2	0.01	4	5
< 1	0.1	0	0
1	0.1	5	4
2	0.1	6	4
< 1	1.0	0	0
1	1.0	8	3
2	1.0	4	3

Table 5.1 – The number of correlations missed are higher in case of the unperturbed OBVIOD than the Newton-Raphson, for high AMR value and observations separated by one or more revolutions.

5.2.2 Comparison between Newton-Raphson Shooting and Bisection-Shooting OBVIOD

The objective after finding out the limitations of Newton-Raphson method was to use a new root finding method inside Shooting IOD. Bisection method was chosen due to the type of function inside Shooting algorithm and the convergence requirements. This section analyses the correlation performance for both the Newton-Raphson method and the Bisection method. Fig. 5.7, Fig. 5.8 and Fig. 5.9 show the number of correlations for the Newton-Raphson and second version of Bisection-Shooting methods for different AMR values for tracklets separated by <1, 1 or 2 revolutions. The Newton-Raphson OBVIOD starts to miss correlations when tracklets are separated by 1 or more revolutions. However Bisection-Shooting is always able to correlate the tracklets.

AMR 0.01 (m^2/Kg)

Fig. 5.7 – The number of revolutions are shown on the x-axis. The Bisection-Shooting performs better than the Newton-Raphson method when the tracklets are separated by one or more revolutions.

AMR 0.1 (m^2/Kg)
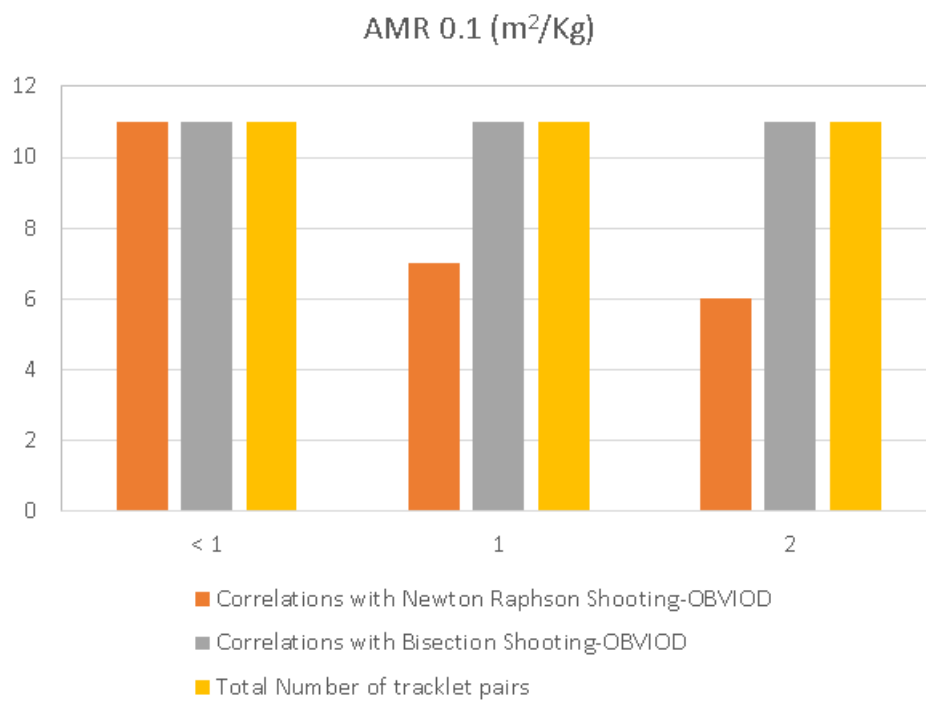
Fig. 5.8 – The number of revolutions are shown on the x-axis.
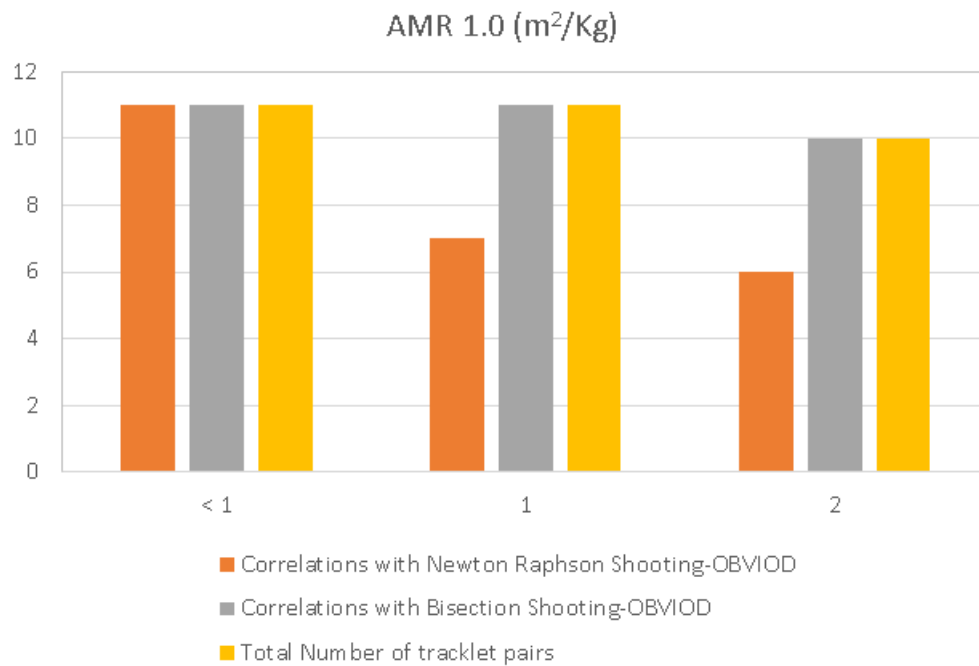
Fig. 5.9 – The number of revolutions are shown on the x-axis. The Bisection-Shooting OB-
VIOD correlates all number of tracklets.
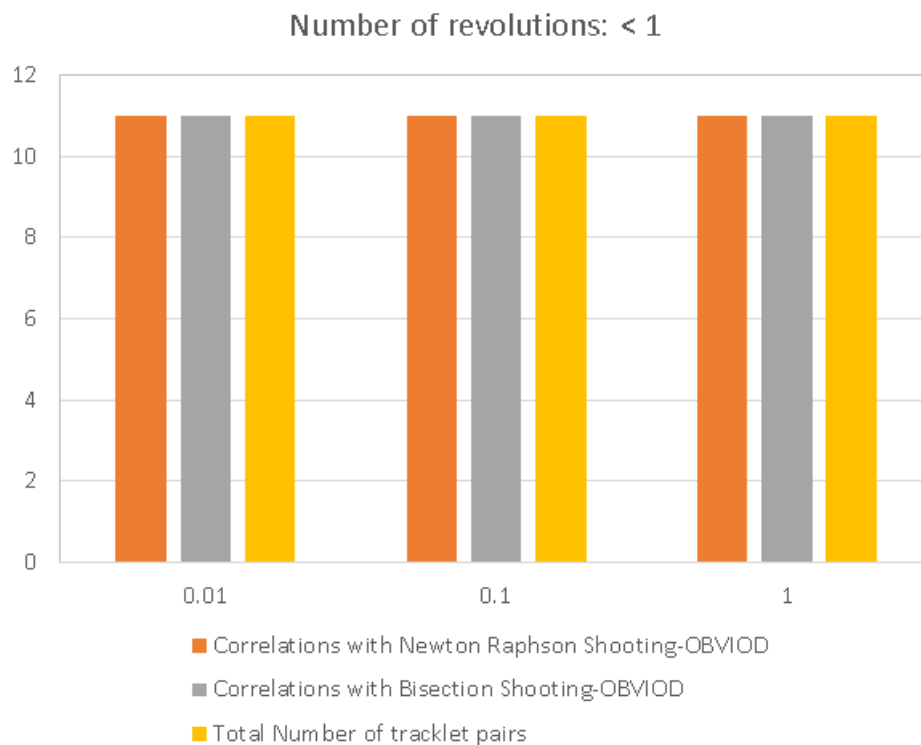
Fig. 5.10 – The x-axis shows the AMR values. Both Newton-Raphson method and Bisection-
Shooting OBVIOD correlate all the tracklet pairs separated by less than one re-
volution.

Fig. 5.11 – The x-axis shows the AMR values. The Newton-Raphson OBVIOD misses some correlations when tracklets are separated by one revolution. However Bisection-Shooting OBVIOD is always able to correlate the tracklets.

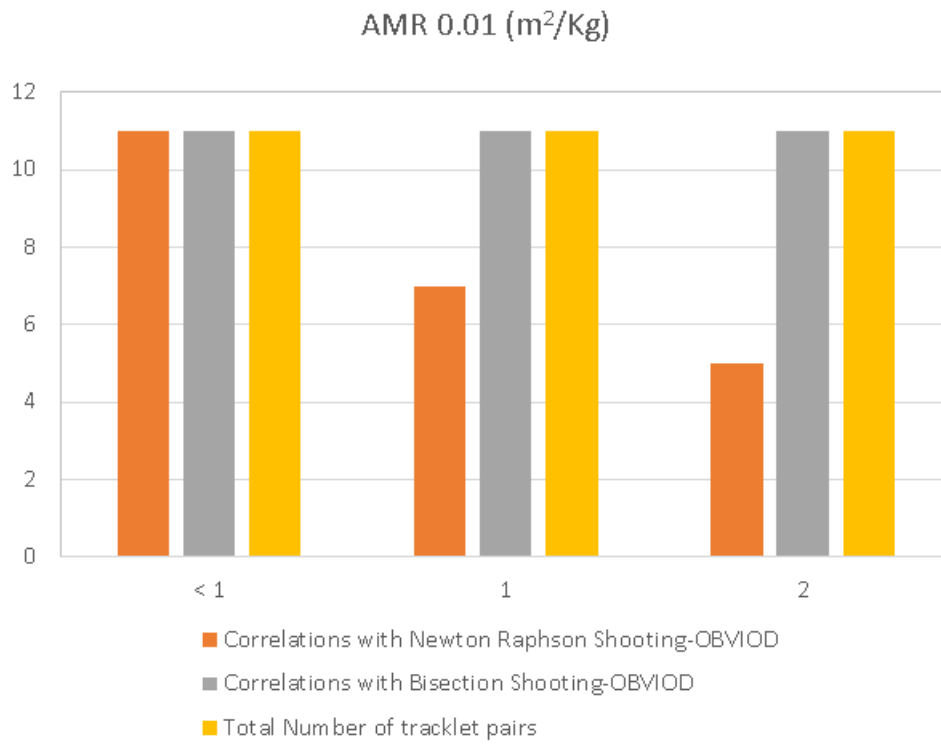**Fig. 5.12** – The x-axis shows the AMR values. Bisection-Shooting OBVIOD correlates all the tested tracklet pairs separated by 2 revolutions.

No. of Revolutions	AMR (m^2/Kg)	Newton Raphson Shooting-OBVIOD	Bisection Shooting-OBVIOD
< 1	0.01	0	0
1	0.01	4	0
2	0.01	**5**	**0**
< 1	0.1	0	0
1	0.1	4	0
2	0.1	**4**	**0**
< 1	1.0	0	0
1	1.0	**3**	**0**
2	1.0	**3**	**0**

Table 5.2 – The Newton-Raphson Shooting-OBVIOD misses some correlations when tracklets are separated by one or more revolutions, this is true for al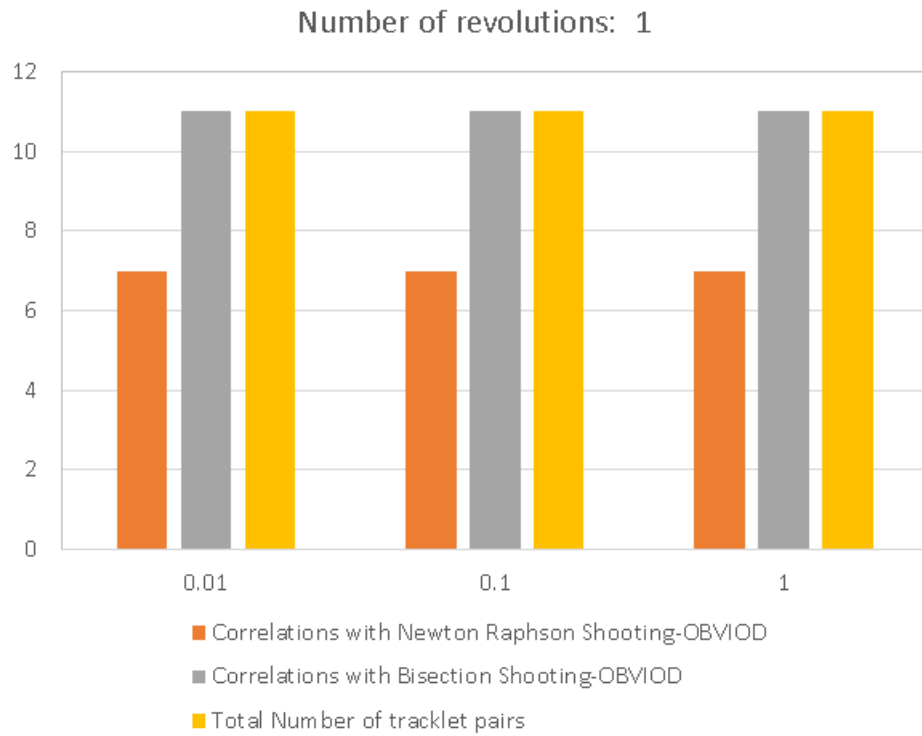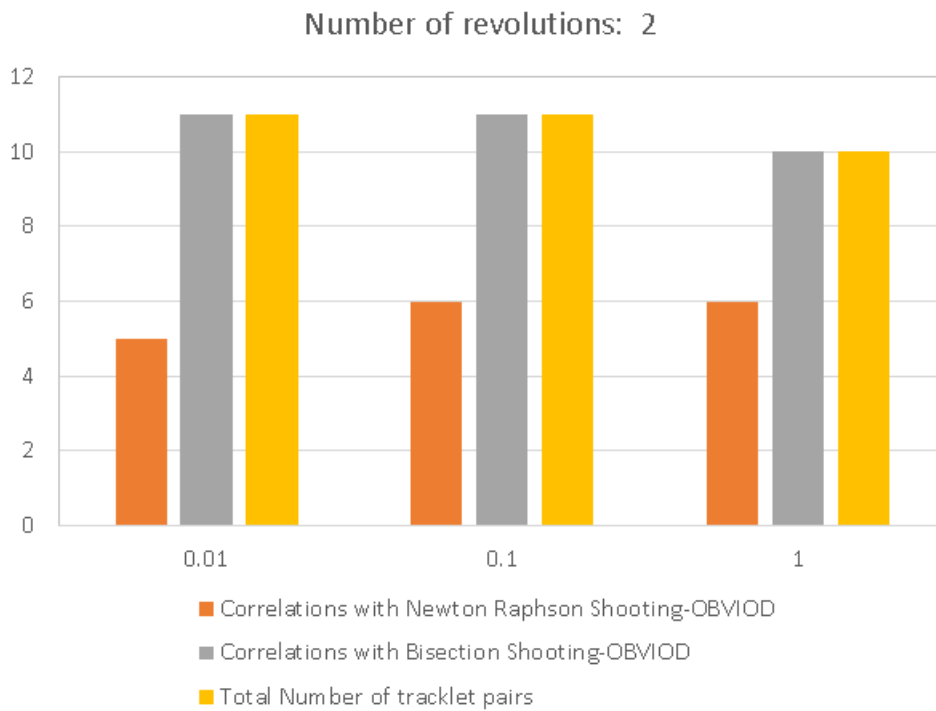l the AMR values tested. The Bisection-Shooting OBVIOD does not miss any correlations for the tracklet pairs tested for different number of revolutions and AMR values.

Fig. 5.10, Fig. 5.11 and Fig. 5.12. show the number of correlations for both the methods for different number of revolutions over a range of AMR values. The summary of all the tests is shown in Table 5.2. The Shooting method with the Newton-Raphson technique is able to correlate all the tracklets, which are only a few hours apart or are separated by less than one revolution. This applies for all the AMR values considered in the tests. However, when the tracklets are one or more revolutions apart, it misses some correlations. Since it takes its initial value from the Lambert solution, it tries to find the root closest to the unperturbed solution. As mentioned in subsection 4.2.3, Newton-Raphson method works well only for good starting values and may diverge otherwise.

For the multiple revolution cases with the increasing number of possible solutions, this starting value is not accurate enough to lead it to the solution. Moreover, for some high AMR cases the unperturbed Lambert algorithm does not converge and hinders the working of Shooting OBVIOD as well.

Significance of results obtained from tests comparing Newton-Raphson Shooting and Bisection Shooting

1. The use of Bisection method inside the Shooting OBVIOD makes it independent from the unperturbed Lambert solution and is not affected by the latter's limitations.

2. Use of semimajor axis constraints: In addition, the use of admissible region based on semimajor axis reduces the number of possible scenarios to be computed. This number reduces to almost half the number of scenarios which were to be considered in the Newton-Raphson Shooting OBVIOD.

3. Convergence: For each bracket that contains a root, Bisection method converges and finds a solution unlike the Newton-Raphson method. Furthermore, it is not affected by the initial boundaries chosen for the bracket as long as the latter contains a root.

4. Use of numerical propagator: In Bisection Shooting all the iterations use the numerical propagator in the root finding procedure. The brackets containing a root are also found using the numerical propagator. This is especially important because doing so one makes sure that the computed results are close to the real scenario. In Newton-Raphson Shooting IOD, the initial value was taken from the unperturbed solution to the Lambert's problem and some of the iterations in the root-finding procedure use the Keplerian propagator. It could be a possible reason why it was difficult for the method to find a root because the Keplerian function plot and the numerical propagator function plot are different. An example of this difference is shown in Fig.4.24.

These are the reasons that make the Shooting OBVIOD with the Bisection method for the root search, a better choice for correlation.

5.2.3 Comparison between unperturbed OBVIOD and Bisection Shooting OBVIOD

Both the methods are compared by varying the number of revolutions and AMR values. All the tests are done with different objects so as to increase the sample size. The number of tracklet pairs tested are still limited owing to the high computation time consumed by the numerical propagator used in Shooting-OBVIOD.

Nevertheless, variation of AMR values while keeping the number of revolutions constant and vice-versa does give an insight about the limitations of unperturbed OBVIOD and how well Shooting OBVIOD is able to overcome them. The results are shown starting from Fig.5.13 to Fig.5.20. The degradation of unperturbed OBVIOD results is evident for one or more revolutions and similarly for very high-area-to-mass-ratio (HAMR) objects. This is expected because with increase in AMR and time-of-flight the perturbations have a higher impact, especially the solar radiation pressure.
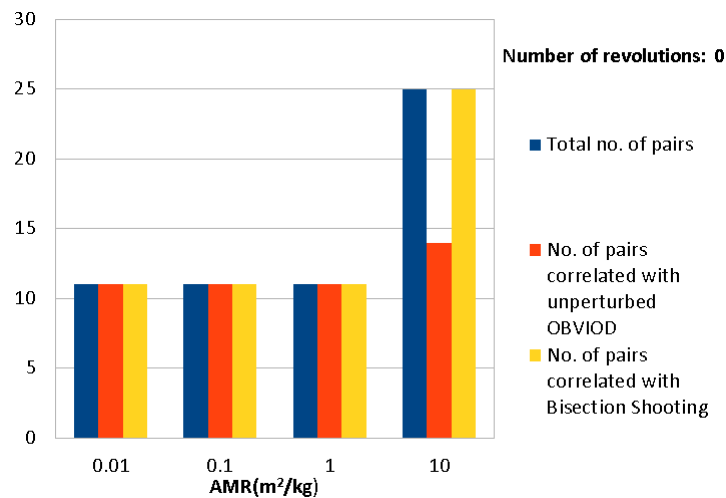
Fig. 5.13 – The AMR value is shown on the x-axis. For tracklet pairs separated by less than 1 revolution, the unperturbed OBVIOD performs equally well except in case of very high AMR.
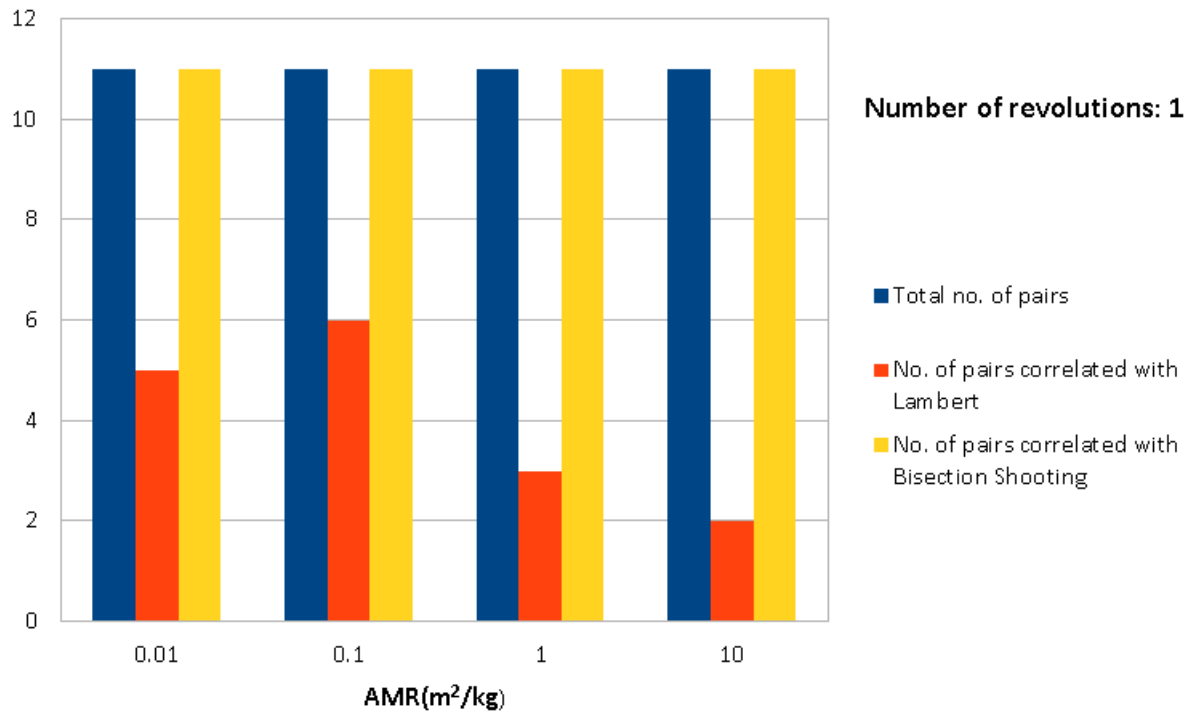
Fig. 5.14 – The AMR value is shown on the x-axis. The performance of the unperturbed OB-
VIOD begins to worsen starting from a case of tracklets separated by 1 revolution.
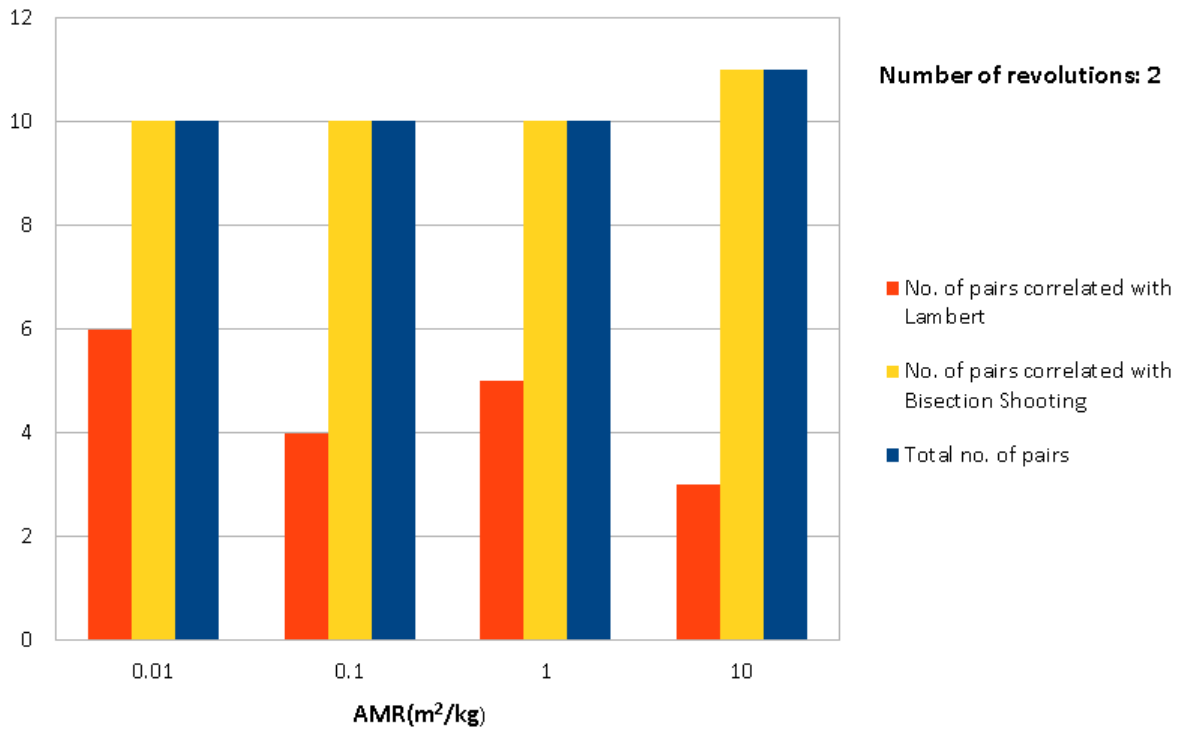
Fig. 5.15 – The AMR value is shown on the x-axis.
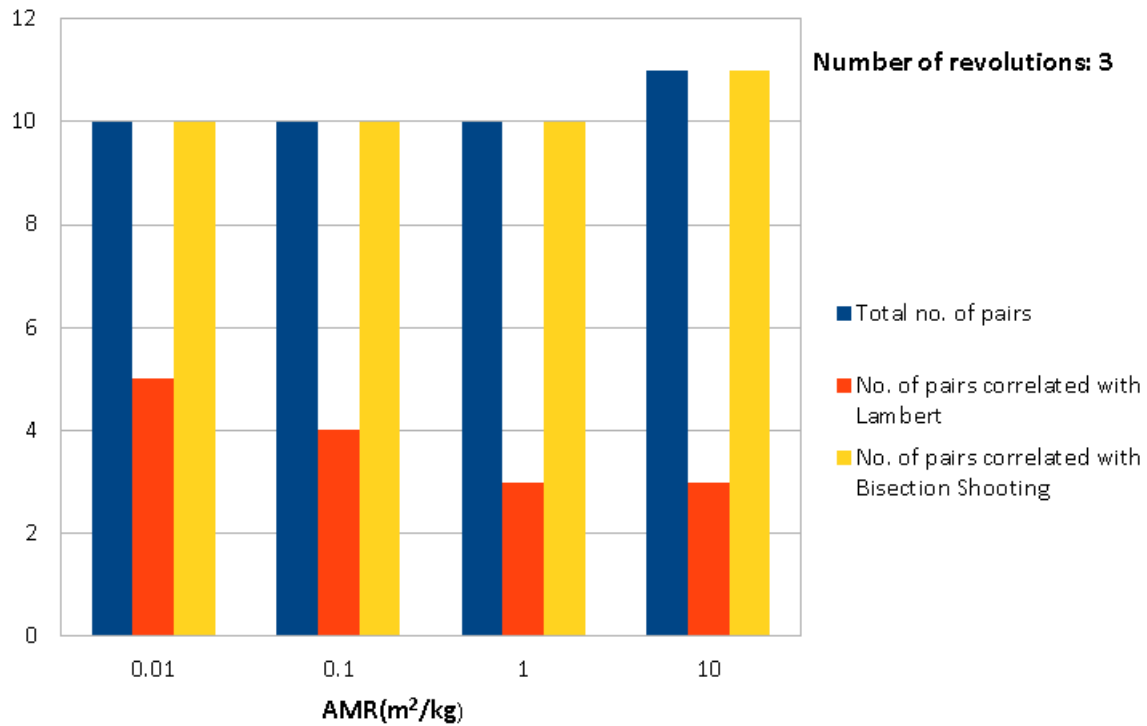
Fig. 5.16 – The AMR value is shown on the x-axis. This case shows a clear decline of number of correlations with the increase in AMR value.
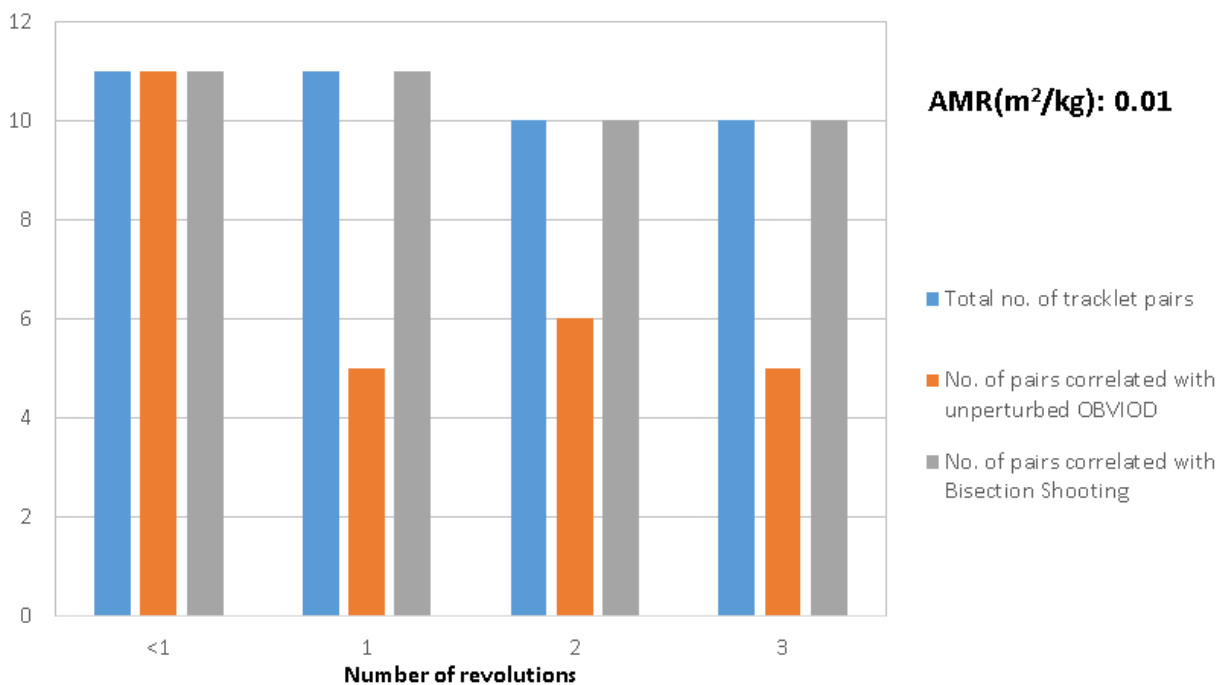
Fig. 5.17 – The number of revolutions are shown on the x-axis. For a small AMR value, the number of correlations decrease with increase in number of revolutions, however, one still gets around 50% of the tracklet pairs correlated.
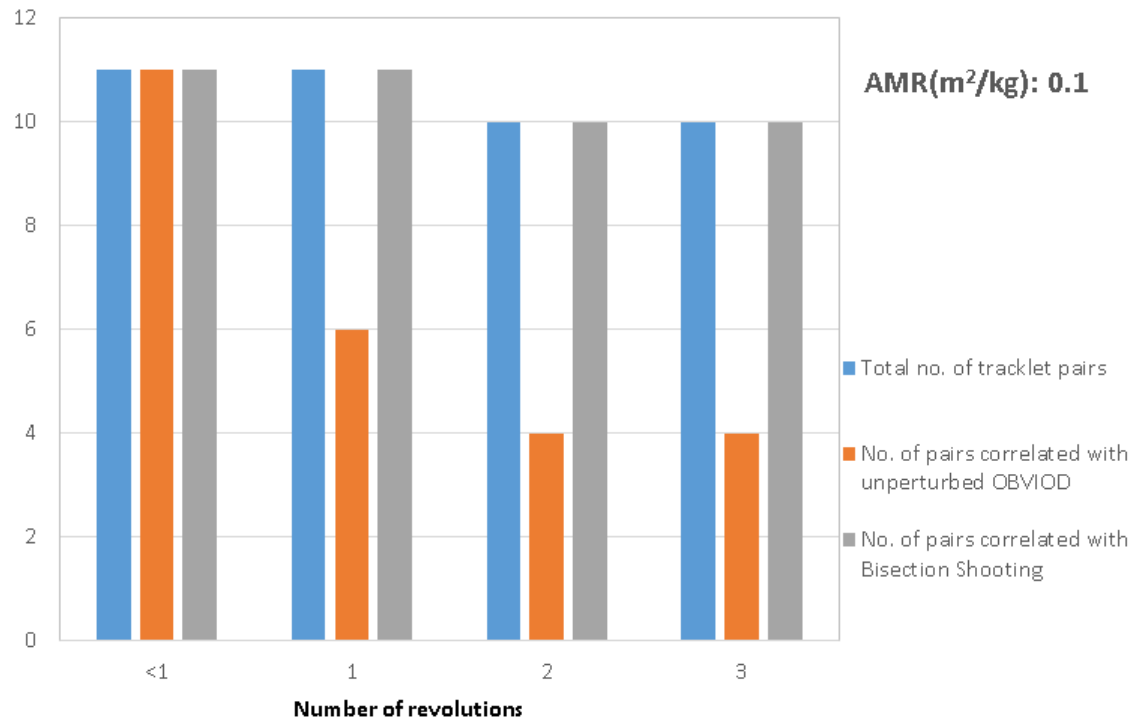
Fig. 5.18 – The number of revolutions are shown on the x-axis. For a slightly higher AMR, the decline in number of correlations is evident with increasing number of revolutions.
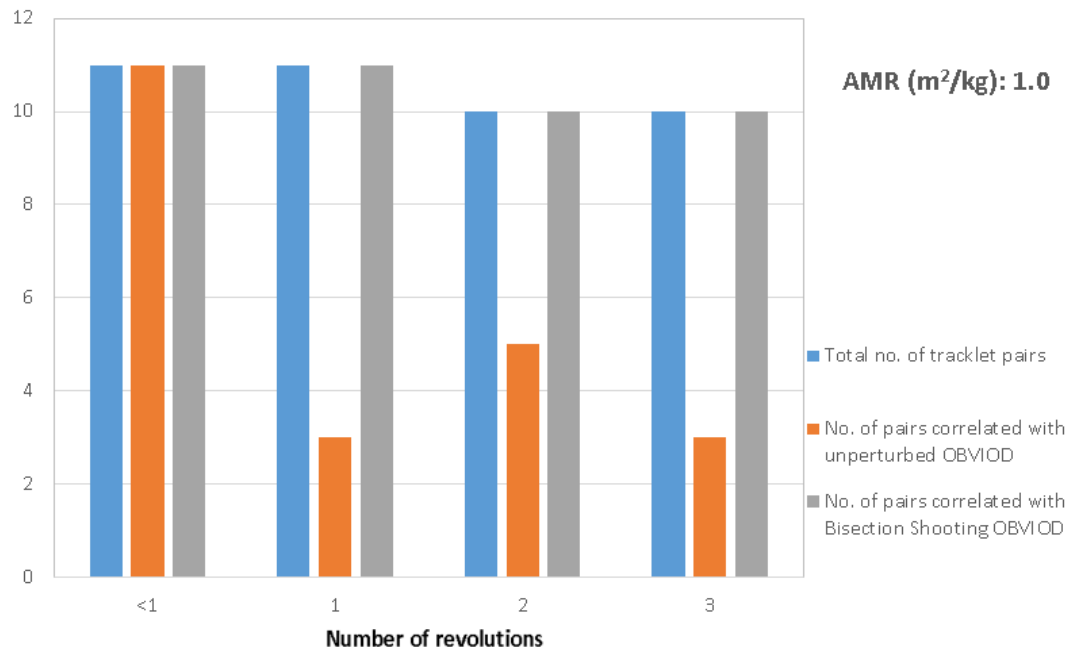
Fig. 5.19 – The number of revolutions are shown on the x-axis. The number of correlations further decreases with increase in the AMR value. Although, the performance does fluctuate between different number of revolutions.
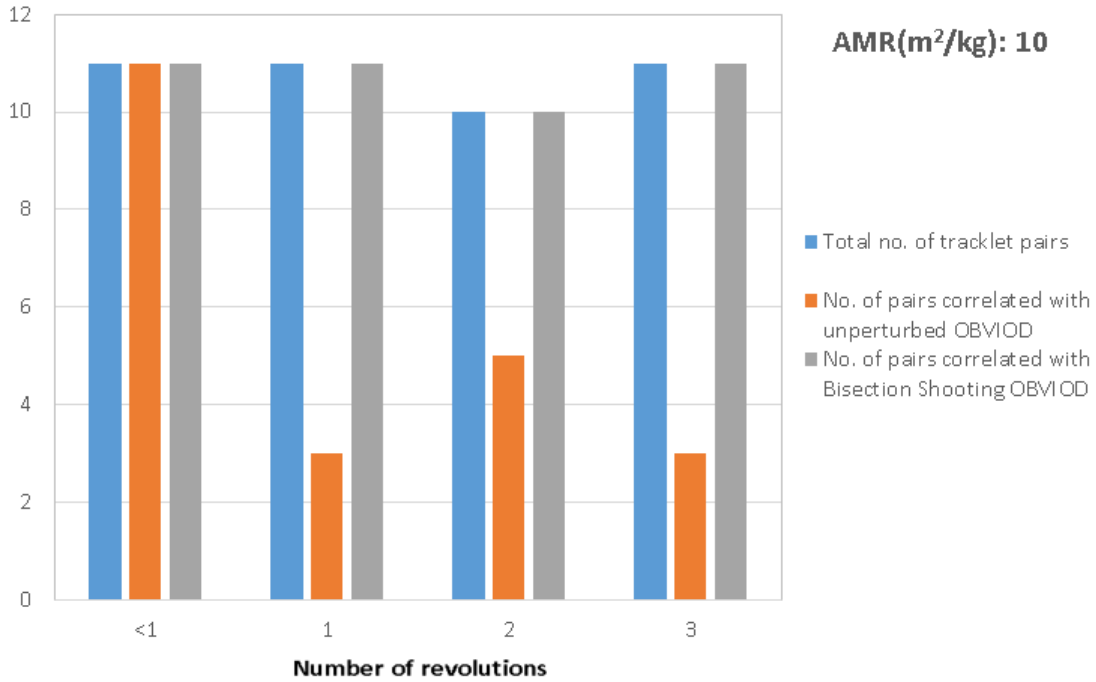
Fig. 5.20 – The number of revolutions are shown on the x-axis. The performance for very high AMR value is comparable to the previous case, when the effect of number of revolutions is considered.

Fig. 5.13, Fig. 5.14, Fig. 5.15 and Fig. 5.16 show the number of correlations for the unperturbed OBVIOD and the Bisection-Shooting OBVIOD for varying number of revolutions over different AMR values. The performance of unperturbed OBVIOD is somewhat similar between 1 and 2 revolutions, with highest AMR value resulting in minimum number of correlations. Fig. 5.17, Fig 5.18, Fig. 5.19 and Fig.5.20 show the correlations for different AMR vlues over varying number of revolutions for both the methods. Unperturbed OBVIOD begins to fail with increase in number of revolutions. This also happens for high AMR objects. The proposed algorithm performs well even in case of HAMR values and multiple revolutions when compared to the unperturbed OBVIOD. Shooting-OBVIOD could replace the latter in case correlation does not take place.

However, the Shooting-OBVIOD comes with some challenges. It works on the basis of brackets which can disappear later in the iterations. In such cases, one could miss the solution (no correlation) because the bracket containing root was not one of the available brackets. There are cases where none of the brackets resulting from the initial hypothesis contain the root. The right bracket may or may not appear in the later iterations. This method has a dependency on the initial ρ pair hypothesis that is taken to begin the iterations. Besides, the numerical propagation makes this algorithm much more slower when compared to the unperturbed OBVIOD.

5.2.4 Factors affecting correlation for Bisection Shooting OBVIOD

Many tracklet pairs with eccentricities between 0 and 0.3 are tested. Fig.5.21 shows number of correlations for different groups of eccentricity values. For tracklets belonging to higher eccentricities (between 0.1 and 0.3) less than half of the pairs are correlated. After investigating the causes it was found that in almost half of the cases that did not work, they

converged on a wrong solution (usually with higher eccentricities, close to 0.5 sometimes) and later the orbit could not be validated using the least-squares improvement. In the other half of the cases that did not work, it is because the algorithm did not converge and ended with a high MD value. In the latter case, the problem was following the wrong bracket (the interval containing a root that does not correspond to the real orbital solution), which also happened in cases where it did converge but with a wrong orbit.
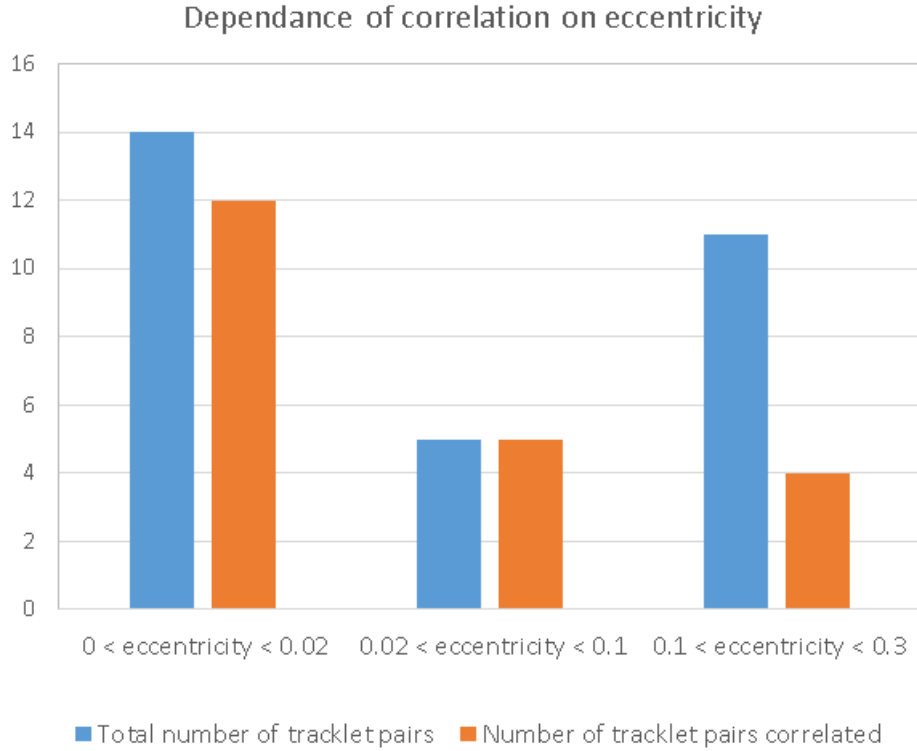
Fig. 5.21 – The number of tracklet pairs correlated decreased for higher eccentricities for new version of the OBVIOD algorithm using angular positions and rates at the second epoch as discriminator in Bisection-Shooting OBVIOD.

In consecutive iterations it is possible that the bracket that initially had a root disappears in the next iteration. In those cases a different bracket is given the same serial number because for the current ρ_1, ρ_2 the older bracket doesn't exist. The brackets appearance and disappearance throughout the iterations has been a big problem in these cases. The reason for this behavior could be the same as in the case when no brackets are found (refer to subsection 4.3.2), there is no solution for the ρ_1, ρ_2 in the current iteration for the given $\overrightarrow{u_1}$, $\overrightarrow{\dot{u_1}}$, $\overrightarrow{r_s}$ and $\overrightarrow{v_s}$. Such a case is shown in Fig.5.22.

One of the parameters that might affect the performance of an initial orbit determination algorithm based on angles-only observations is the transfer angle. This is widely mentioned in the literature also for the Lambert's problem (Battin (1999), Gauss (1963), Zhang et al. (2010), Gooding (1990), Vallado (2007)). The transfer angle, θ is the angular difference between the line-of-sight angles at epoch of the first tracklet and the second. Some of the solutions proposed to IOD problem had a sensitivity at certain θ values which varies depending on the algorithms.

Many tracklet pairs were further tested to find out if the algorithm performance depended on the transfer angle. The groups were divided into θ less than 1 degree, between 1 and

```
bracket1_root1amax[0]:-19.106679444780895
bracket1_root1amax[1]:548.3144021070449
bracket2_root1amax[0]:0.0
bracket2_root1amax[1]:0.0
bracket3_root1amax[0]:0.0
bracket3_root1amax[1]:0.0
bracket4_root1amax[0]:0.0
bracket4_root1amax[1]:0.0
bracket1_root2amax[0]:-19.106679444780895
bracket1_root2amax[1]:-302.8172202206939
bracket2_root2amax[0]:0.0
bracket2_root2amax[1]:0.0
bracket3_root2amax[0]:0.0
bracket3_root2amax[1]:0.0
bracket4_root2amax[0]:0.0
bracket4_root2amax[1]:0.0
```

(a)

```
bracket1_root1amax[0]:-19.106679444780895
bracket1_root1amax[1]:363.0592732482155
bracket2_root1amax[0]:0.0
bracket2_root1amax[1]:0.0
bracket3_root1amax[0]:0.0
bracket3_root1amax[1]:0.0
bracket4_root1amax[0]:0.0
bracket4_root1amax[1]:0.0
bracket1_root2amax[0]:0.0
bracket1_root2amax[1]:0.0
bracket2_root2amax[0]:0.0
bracket2_root2amax[1]:0.0
bracket3_root2amax[0]:0.0
bracket3_root2amax[1]:0.0
bracket4_root2amax[0]:0.0
bracket4_root2amax[1]:0.0
```

(b)

Fig. 5.22 – An example showing the disappearance of second bracket from one BFGS iteration to another. In case the second bracket was being followed for a solution in BFGS iterations, this occurrence forces the Shooting IOD solution to be that of the first bracket instead.

20 degrees, and finally between 90 and 140 degrees. The separation of line-of-sight angles at small values is a problem in some cases where it is difficult to find out the number of revolutions. It is an issue from geometric point of view, it can cause numerical instability and may yield incorrect answers. The information about angular positions may not be sufficient in these cases and adding the error makes it even more challenging. For high values of the difference in line-of-sight angles some of the correlations were missed (Fig. 5.23). In the latter cases, the algorithm converged on a wrong solution.
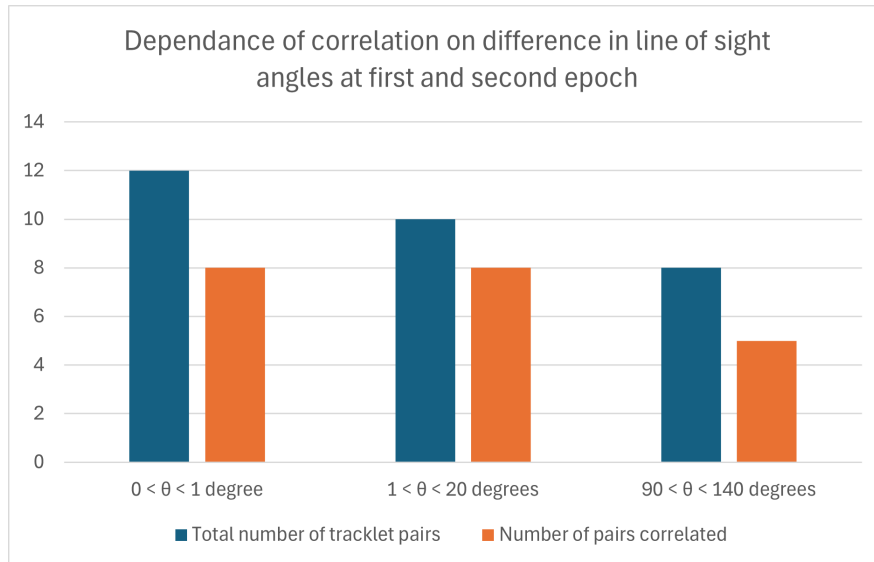
Fig. 5.23 – The number of tracklet pairs correlated decreased for higher value of the transfer angle θ and for very small values for second version of the OBVIOD algorithm using angular positions and rates at the second epoch as discriminator in Bisection-Shooting OBVIOD.
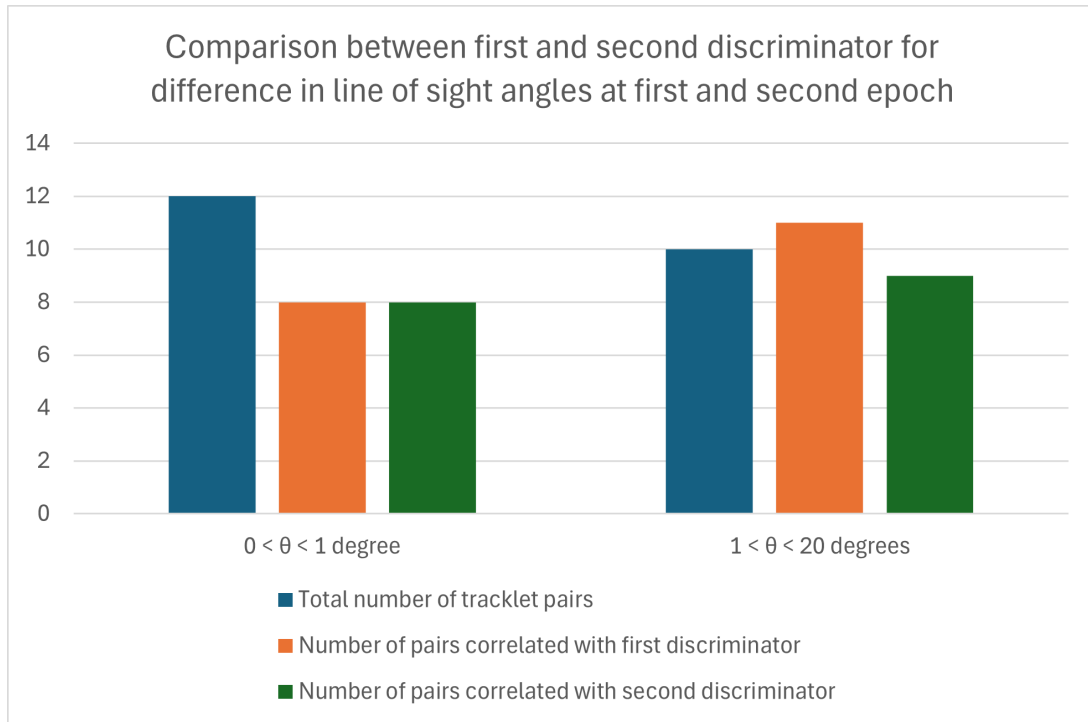
Fig. 5.24 – The range of θ angle values is tested for various tracklets and it is found that the second version discriminator using angular rates at both epochs performs slightly better than the first discriminator.
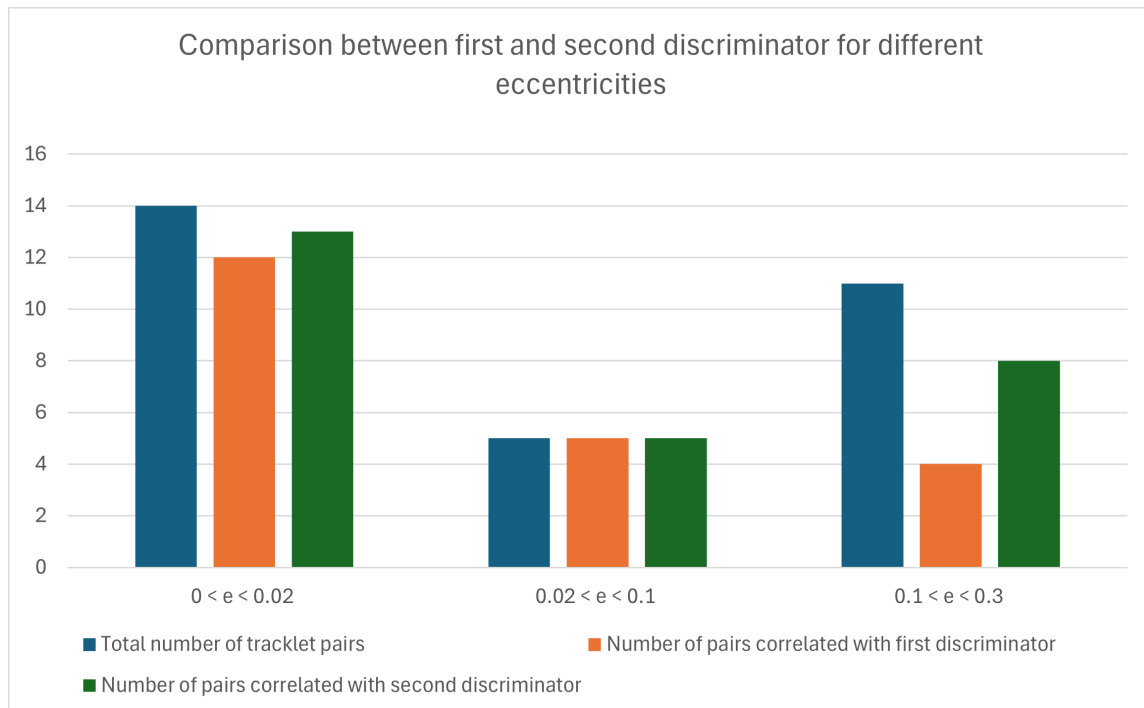
Fig. 5.25 – The range of eccentricity values is tested for both the versions of the Bisection-Shooting algorithm. It is found that the second version discriminator performs better for lower and the higher eccentricity values where the first discriminator misses many correlations between the tracklet pairs.

In order to find out if the second version of the Bisection-Shooting algorithm performed differently it was tested for the same groups of tracklet pairs for eccentricity. It was tested for some of the tracklet pairs for angle θ as well. The results are shown in Fig.5.24 and Fig.5.25.

As can be seen from the figures the higher eccentricities group performs better with the second discriminator (angular rates at both the epochs). The number of correlations are either equal or higher than the first discriminator. It could possibly signal that the second discriminator values $(\dot{\alpha}_1, \dot{\delta}_1, \dot{\alpha}_2, \dot{\delta}_2)$ are more accurate than the ones used with the first discriminator $(\alpha_2, \delta_2, \dot{\alpha}_2, \dot{\delta}_2)$. The former are redundant in the sense that $(\dot{\alpha}_1, \dot{\delta}_1)$ are used in the Shooting method IOD as well.

On the other hand, several solutions are possible. This happens because the algorithm in first version of Bisection-Shooting uses angular positions at the second epoch as a discriminator, which are not very reliable because of the very-short-arc observations and the observation error. The latter is more pronounced in the angular positions than angular rates. In the orbital boundary value problem, even with angular positions multiple solutions are possible, angular rates help solve the ambiguity through the discriminator. Having 4 rates reinforces the disambiguation w.r.t. 2 rates only and 2 boundary values (α_2, δ_2), the latter creating ambiguity as in the original Lambert problem. So, one can take the second discriminator as the better algorithm. Based on the all the tests conducted the second discriminator performs equal to or better than the first discriminator.

The processing path of the algorithm is shown in Fig. 5.26 and Fig. 5.27 for a tracklet pair which was tested using both the versions of the Bisection-Shooting algorithm. Even though the tracklet pair was correlated with both the versions, the true solution is closer to the solution found by the second discriminator.
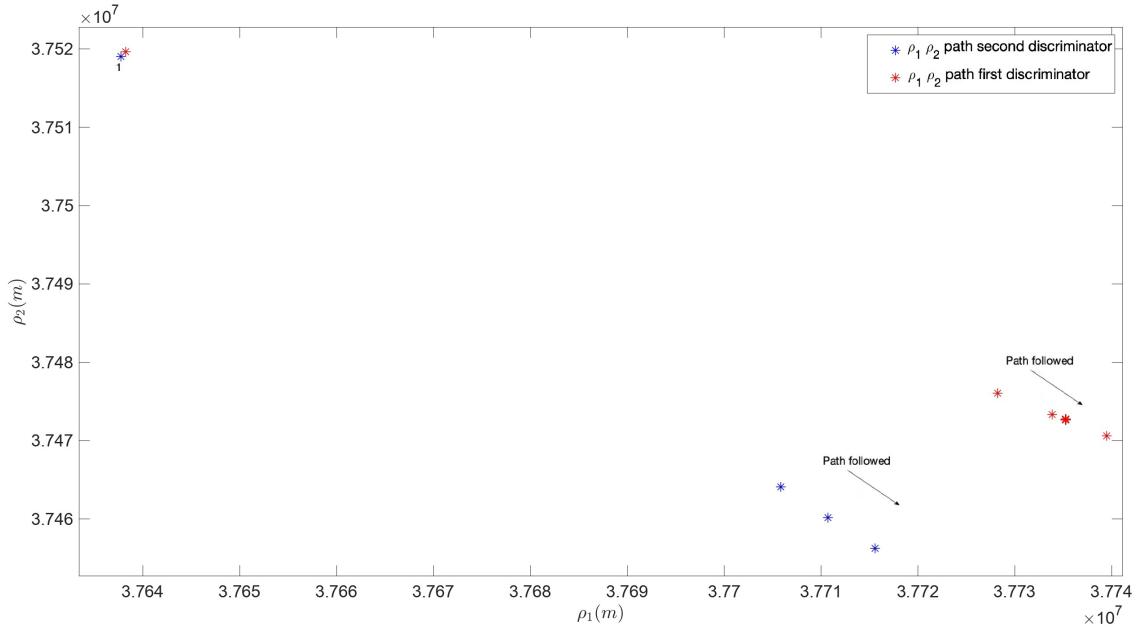
Fig. 5.26 – The path followed by ρ_1, ρ_2 during processing in the first and second version of the Bisection-Shooting algorithm is shown above.
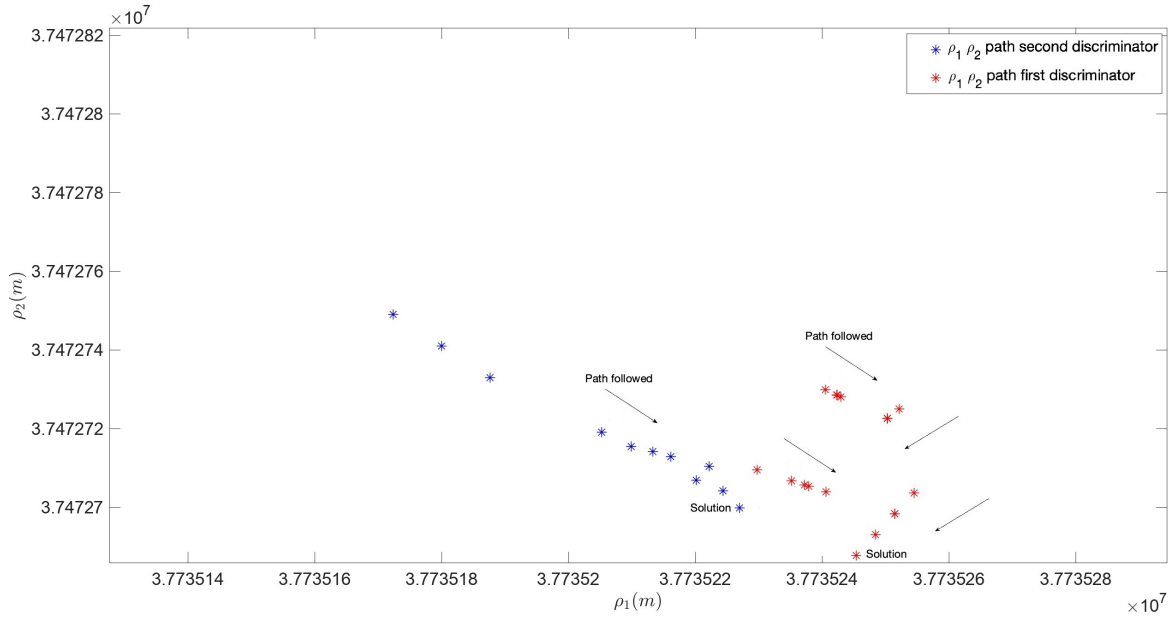
Fig. 5.27 – The path followed by ρ_1, ρ_2 during processing in the first version and second version of the Bisection-Shooting algorithm with a focus on the solution region.

5.2.5 Summary of tests conducted

The tests conducted followed the path of development of the Shooting OBVIOD algorithm starting from the Newton-Raphson method to different versions of the Bisection Shooting OBVIOD. The correlation performance with varying number of revolutions and AMR values was explored, discussed for various versions. For the Bisection-Shooting algorithm the effect of eccentricity and the difference of line-of-sight angles at the first, second epoch was tested as well. A comparison was drawn between both the discriminators and the results were interpreted for the cases tested. Finally the processing path of both the versions was plotted in order to visualize the difference for a tracklet pair which was correlated by both the versions.

6 Conclusion

6.1 Summary

This thesis contributes a tracklet-to-tracklet correlation and initial orbit determination method with perturbations. In the first chapter, the space debris problem is introduced. The survey strategies for optical observations using ground based telescopes are briefly described in addition to the object tracking techniques. It is followed by the orbit determination and catalog correlation which is a part of the processing of the survey series. The optical measurements obtained from the observation strategies are defined along with the concept of a tracklet.

The second chapter describes various concepts starting from the admissible region (AR) to the tracklet-to-tracklet correlation for space objects.

The AR is used in many of the methods presented from literature survey including Milani et al. (2004), Milani et al. (2005), Tommei et al. (2007), Fujimoto et al. (2014) and Spoto et al. (2018). The former two sources also introduce the concept of attributable which became popular and was used by some other authors. In the tracklet correlation methods some of authors like Musci et al. ('Orbit improvement for GEO objects using follow-up observations') proposed determination of circular orbits. Some authors mapped the AR to a different element space (Delaunay or Poincaré) to find the point of intersection at a common epoch. Another approach uses the concept of Virtual Debris or Virtual Particles to represent the possible state of the observed object over the AR. The presented works from the literature survey are analysed based on performance, multi-revolution problem and perturbations.

The work in this thesis is based on a previously developed work on the orbital boundary value problem called OBVIOD (Siminski et al., 2014). The latter is explained in the third chapter, where the Lambert's problem is also described. The OBVIOD algorithm uses the solution of Izzo (2014) for a given ρ_1, ρ_2 hypothesis in the BFGS iterations.

The addition of perturbations in the existing OBVIOD technique is done using Shooting method. It treats the boundary value problem as an initial value problem and propagates an initial hypothesis from one boundary value such that the second boundary value condition is met. The Newton-Raphson mechanism is used as a root-finding procedure inside the Shooting-OBVIOD. The unperturbed OBVIOD and the Newton-Raphson Shooting-OBVIOD are compared by varying the number of revolutions and AMR values. The performance of the Shooting-OBVIOD is better than the unperturbed version. However, the Newton-Raphson method suffers from different limitations owing to its sensitivity to the starting value, the dependance on Lambert's solution and convergence issues.

It became imperative to investigate the function behavior in the Shooting IOD and come up with a suitable root-finding routine. It is discovered that the function is continuous with multiple roots. An AR based on semimajor axis value is introduced and Bisection method is chosen due to its reliability for continuous functions. Since the angular positions at the second epoch are not being used in the Shooting IOD, they are included in the first version

of Bisection Shooting OBVIOD as the discriminator along with the angular rates at the second epoch. The second version of Bisection Shooting OBVIOD has the angular rates at both the epochs as the discriminator, same as the unperturbed OBVIOD. The loss function topography of both these versions is analysed. The effect of length of a tracklet on correlation is studied shedding light on the limitations of linear model of the attributables.

The unperturbed OBVIOD and both the versions of Bisecting Shooting OBVIOD undergo various tests, which are done with different simulated objects so as to increase the sample size. The number of tracklet pairs tested are still limited owing to the high computation time consumed by the numerical propagator in Shooting OBVIOD. Nevertheless, variation of AMR values while keeping the number of revolutions constant and vice-versa does give an insight about the limitations of unperturbed OBVIOD and how well Shooting-OBVIOD is able to overcome them. The degradation of unperturbed OBVIOD results is evident for 1 or more revolutions and similarly for very high-area-to-mass-ratio (HAMR) objects. This is expected because with increase in AMR and tof the perturbations have a higher impact, especially the solar radiation pressure.

Unperturbed OBVIOD begins to fail with increase in number of revolutions. This especially happens for HAMR objects. The proposed Bisection-Shooting algorithm performs well even in case of HAMR values and multiple revolutions when compared to the unperturbed OBVIOD. Shooting OBVIOD could replace the latter in case the correlation doesn't take place for a tracklet pair. The second version of the Bisection-Shooting OBVIOD (angular rates discriminator) fares better than the first and is the one which should be further developed.

However, the Shooting-OBVIOD comes with some challenges. It works on the basis of brackets which can disappear later in the iterations. In such cases, one could miss the solution (no correlation) because the bracket containing root was not one of the available brackets. There are cases where none of the brackets resulting from the initial hypothesis contain the root. The right bracket may or may not appear in the later iterations. This method has a dependency on the initial ρ pair hypothesis that is taken to begin the iterations. Besides, the numerical propagation makes this algorithm much more slower when compared to the unperturbed OBVIOD.

6.2 Future Work

The future work foreseen for the methods developed in this thesis could begin from using a different propagator. A semi-analytical propagator called Draper Semi-analytical Satellite Theory (DSST) was tested from the Orekit library, however, its execution time was not very different than the numerical one finally used. Although the analysis by Setty et al. (2016) shows there is a performance gain expected, the Orekit 9.0 and Orekit 10.0 space dynamics libraries (more info at Orekit (2018)) failed to reach that. The main culprit turned out to be the SRP force model being used which was very expensive. Analytical approximation of the SRP force model could reduce the computational load. In order to reduce the latter, the search for a different root-finding routine or a modified version of the proposed Bisection method would also be helpful. In case a modified version of Bisection method is considered, the shifting or disappearance of the brackets would have to be tackled. If a different routine is used, a strategy to separate the different roots inside the Shooting IOD would need to be formed. It could be based on the number of revolutions, however, its dependence on the free

parameters used should be investigated using function topography.

In addition, the choice of AR could be modified to study its impact on the gated interval for Shooting IOD. For a modified Bisection technique it could shed light on how the range hypothesis from OBVIOD gives rise to varied number of brackets over subsequent BFGS iterations. Moreover, the correlation performance of Shooting-OBVIOD could be examined by changing the free parameters in either of the iterations. A different method to add perturbations in OBVIOD could also be explored.

Finally tests should be performed with real observations, a gain on performance would facilitate such tests. That would enable this method to be used for catalog maintenance in addition to the non-perturbed IOD techniques.

Bibliography

Acton, F. S. (1970). *Numerical methods that work*. The Mathematical Association of America. DOI: `10.2307/2318938`.

Bate, R., Mueller, D. and White, J. E. (1971). *Fundamentals of Astrodynamics*. Dover Publications. ISBN: 0-486-60061-0.

Battin, R. H. (1999). *An Introduction to the Mathematics and Methods of Astrodynamics*. American Institute of Aeronautics and Astronautics. ISBN: 978-1-56347-342-5. DOI: `https://doi.org/10.2514/4.861543`.

Bern, M. and Eppstein, D. (1992). *Mesh Generation and Optimal Triangulation*. Tech. rep. Palo Alto Research Center, Palo Alto, California 94304, U.S.A.

Beutler, G. (2004). *Methods of Celestial Mechanics:Theory and Applications*. Springer-Verlag. ISBN: 978-3-540-40750-8.

Cordelli, E., Lauber, P., Prohaska, M., J.Rodriguez, Schlatter, P. and Schildknecht, T. (2019). 'Recent Developments at the Swiss optical ground station and geodynamics observatory Zimmerwald'. In: *1st NEO and Debris Detection Conference, Darmstadt, Germany*.

Curzi, G., Modenini, D. and Tortora, P. (2020). 'Large Constellations of Small Satellites: A Survey of Near Future Challenges and Missions'. In: *Special Issue Advances in Aerospace Sciences and Technology* 7.9. DOI: `10.3390/aerospace7090133`.

DeMars, K. J. and Jah, M. K. (2013). 'Probabilistic Initial Orbit Determination Using Gaussian Mixture Models'. In: *Journal of Guidance, Control and Dynamics* 36.5, pp. 1324–1335. DOI: `10.2514/1.59844`.

ESA (2020). *About space debris*. URL: `https://www.esa.int/Safety_Security/Space_Debris/About_space_debris`.

ESOC (2020). *ESA's Annual Space Environment Report*. Tech. rep. ESA/ESOC, Darmstadt, Germany.

Früh, C. and Schildknecht, T. (2012). 'Object image linking of earth orbiting objects in the presence of cosmics'. In: *Advances in Space Research* 49.3. ISSN: 0273-1177. DOI: `https://doi.org/10.1016/j.asr.2011.10.021`.

Fujimoto, K. and Scheeres, D. J. (2012). 'Correlation of Optical Observations of Earth-Orbiting Objects and Initial Orbit Determination'. In: *Journal of Guidance, Control and Dynamics* 35.1.

Fujimoto, K., Scheeres, D. J., Herzog, J. and Schildknecht, T. (2014). 'Association of optical tracklets from a geosynchronous belt survey via the direct Bayesian admissible region approach'. In: *Advances in Space Research* 53.2. ISSN: 0273-1177. DOI: `https://doi.org/10.1016/j.asr.2013.11.021`.

Gadaleta, S. M., Horwood, J. T. and Poore, A. B. (2012). 'Short Arc Gating in Multiple Hypothesis Tracking for Space Surveillance'. In: *Proceedings of SPIE, Baltimore, Maryland, U.S.A.*

Gauss, C. F. (1963). 'Theory of the Motion of the Heavenly Bodies Moving about the Sun in Conic Sections, reprinted'. In: *Dover publications*.

Gooding, R. (1990). 'A procedure for the solution of Lambert's orbital boundary-value problem'. In: *Celestial Mechanics and Dynamical Astronomy* 48.2. DOI: `https://doi.org/10.1007/BF00049511`.

Herrick, S. and Liu, A. (1959). 'Two Body Orbital Determination From Two Positions and Time of Flight'. In: *Aeronutronic (Retired Journal)* Volume C (365 1959).

Herzog, J., Schildknecht, T., Hinze, A., Ploner, M. and Vananti, A. (2013). 'Space Surveillance Observations at the AIUB Zimmerwald Observatory'. In: *European Space Debris Conference, Darmstadt, Germany*.

Hussein, I. I., Roscoe, C. W. T., Schumacher, P. W. and Wilkins, M. P. (2014). 'Probabilistic Admissible Region for Short-Arc Angles-Only Observations'. In: *AMOS, Maui, Hawaii, U.S.A.*

Izzo, D. (2014). 'Revisiting Lambert's problem'. In: *Celestial Mechanics and Dynamical Astronomy* 121 (Mar. 2014). DOI: `10.1007/s10569-014-9587-y`.

Jehn, R., Klinkrad, H. and Schildknecht, T. (2007). 'Observing the geostationary ring'. In: *3rd International Conference on Recent Advances in Space Technologies, Istanbul, Turkey*.

Kessler, D. J. and Cour-Palais, B. G. (1978). 'Collision frequency of artificial satellites: The creation of a debris belt'. In: *Journal of Geophysical Research* 83 (A6 1978). DOI: `10.1029/JA083iA06p02637`.

Lagrange, J. L. (1788). *Mécanique Analytique Vol. II*. Académie des Sciences. DOI: `https://doi.org/10.1017/CBO9780511701795`.

Lancaster, E. R. (1969). *Solution for Lambert problem for short arcs*. Tech. rep. NASA Goddard Space Flight Center, Greenbelt, MD, United States.

Maruskin, J. M., Scheeres, D. J. and Alfriend, K. T. (2009). 'Correlation of Optical Observations of Objects in Earth Orbit'. In: *Journal of Guidance, Control, and Dynamics* 32.1, pp. 194–209. DOI: `10.2514/1.36398`.

Maruskin, J. M., Scheeres, D. J. and Bloch, A. M. (2007). 'SubVolumes in Dynamical Systems and the Tracking of Space Debris'. In: *The Proceedings of the 2007 AAIA/AAS Astrodynamics Specialist Conference, AIAA, Reston, VA*.

Milani, A. and Gronchi, G. (2009). *Part III - Population Orbit Determination*. Cambridge University Press. ISBN: 9781139175371. DOI: `https://doi.org/10.1017/CBO9781139175371`.

Milani, A., Gronchi, G., Vitturi, M. M. and Knezevic, Z. (2004). 'Orbit Determination with Very Short Arcs. I Admissible Regions'. In: *Celestial Mechanics and Dynamical Astronomy* 90. DOI: `https://doi.org/10.1007/s10569-004-6593-5`.

Milani, A., Gronchi, G. F., Knezevic, Z., Sansaturio, M. E. and Arratia, O. (2005). 'Orbit determination with Very Short Arcs. II Identifications'. In: *Icarus* 179.2, pp. 350–374. ISSN: 0019-1035. DOI: `https://doi.org/10.1016/j.icarus.2005.07.004`.

Milani, A. and Knezevic, Z. (2005). 'From astrometry to celestial mechanics: Orbit determination with very short arcs'. In: *Celestial Mechanics and Dynamical Astronomy* 92. DOI: `https://doi.org/10.1007/s10569-005-3314-7`.

Milani, A., Sansaturio, M. E. and Chesley, S. R. (2001). 'The asteroid identification problem IV: Attributions'. In: *Icarus* 151.

Muinonen, K., Granvik, M., Oszkiewicz, D., Pieniluoma, T. and Pentikäinen, H. (2012). 'Asteroid orbital inversion using a virtual-observation Markov-chain Monte Carlo method'. In: *Planetary and Space Science* 73, 15–20. DOI: `10.1016/j.pss.2012.07.016`.

Muinonen, K., Virtanen, J., Granvik, M. and Laakso, T. (2006). 'Asteroid orbits using phase-space volumes of variation'. In: *Monthly Notices of the Royal Astronomical Society* 368.2, pp. 809–818. ISSN: 0035-8711. DOI: `10.1111/j.1365-2966.2006.10168.x`.

Musci, R., Schildknecht, T., Flohrer, T. and Beutler, G. (2005). 'Concept for a catalogue of space debris in GEO'. In: *European Space Debris Conference, Darmstadt, Germany*.

Musci, R., Schildknecht, T. and Ploner, M. 'Orbit improvement for GEO objects using follow-up observations'. In: *Advances in Space Research* ().

Orekit (2018). *A Space Dynamics Library*. URL: `https://orekit.org/`.

Porras, D. (2018). *Towards ASAT Test Guidelines*. Tech. rep. The United Nations Institute for Disarmament Research.

Press, W., Teukolsky, S., Vetterling, W. and Flanner, B. (1992). *Numerical Recipes in Fortran 77, second ed.* Cambridge University Press. ISBN: 0-521-43064-X.

Prussing, J. E. (2000). 'A class of Optimal Two-Impulse Rendezvous Using Multiple-Revolution Lambert Solutions'. In: *Journal of Astronautical Sciences* 48. DOI: `https://doi.org/10.1007/BF03546273`.

Prussing, J. E. and Conway, B. A. (1993). *Orbital Mechanics*. Oxford University Press. ISBN: 978-0-19-983770-0.

Russ, S. (1980). 'A translation of Bolzano's paper on the intermediate value theorem'. In: *Historia Mathematica* 7.2, pp. 156–185. ISSN: 0315-0860. DOI: `https://doi.org/10.1016/0315-0860(80)90036-1`.

Schildknecht, T. (1994). 'Optical astrometry of fast moving objects using CCD detectors'. PhD thesis. University of Bern.

Schildknecht, T. (2007). 'Optical surveys for space debris'. In: *Astronomy and Astrophysics Review* 14. DOI: `https://doi.org/10.1007/s00159-006-0003-9`.

Schildknecht, T., Hugentobler, U. and Ploner, M. (1999). 'Optical Surveys of Space Debris in GEO'. In: *Advances in Space Research* 23.1, pp. 45–54. ISSN: 0273-1177. DOI: `https://doi.org/10.1016/S0273-1177(98)00229-4`.

Schildknecht, T., Hugentobler, U. and Ploner, M. (2001). 'The search for debris in GEO'. In: *Advances in Space Research* 28.9, pp. 1291–1299. ISSN: 0273-1177. DOI: `https://doi.org/10.1016/S0273-1177(01)00399-4`.

Schildknecht, T., Hugentobler, U. and Verdun, A. (1995). 'Algorithms for ground-Based Optical Detection of Space Debris'. In: *Advances in Space Research* 16.11. ISSN: 0273-1177. DOI: `https://doi.org/10.1016/0273-1177(95)98752-A`.

Schildknecht, T., Hugentobler, U. and Verdun, A. (1997). 'Optical observations of space debris with the zimmerwald 1-m telescope'. In: *Advances in Space Research* 19. Space Debris, pp. 221–228. ISSN: 0273-1177. DOI: `https://doi.org/10.1016/S0273-1177(97)00004-5`.

Schildknecht, T., Musci, R., Ploner, M., Beutler, G., Flury, W., Kuusela, J. et al. (2004). 'Optical observations of space debris in GEO and in highly-eccentric orbits'. In: *Advances in Space Research* 34.4. DOI: `10.1016/j.asr.2003.01.009`.

Schildknecht, T., Vananti, A., Cordelli, E. and Flohrer, T. (2019). 'Optical Surveys to Characterize Recent Fragmentation Events in GEO and HEO'. In: *First Int'l Orbital Debris Conference, Houston, Texas, U.S.A.*

Schneider, M. D. (2012). 'Bayesian linking of geosynchronous orbital debris tracks as seen by the Large Synoptic Survey Telescope'. In: *Advances in Space Research* 49.4, pp. 655–666. ISSN: 0273-1177. DOI: `https://doi.org/10.1016/j.asr.2011.11.011`.

Schumacher, P., Wilkins, M. and Roscoe, C. (2013). 'Parallel Algorithm for Track Initiation for Optical Space Surveillance'. In: *ESA, 6th European Conference on Space Debris, Darmstadt, Germany.*

Setty, S., Cefola, P., Montenbruck, O. and Fiedler, H. (2016). 'Application of Semi-analytical Satellite Theory Orbit Propagator to Orbit Determination for Space Object Catalog Maintenance'. In: *Advances in Space Research* 57 (Mar. 2016), pp. 2218–2233. DOI: `10.1016/j.asr.2016.02.028`.

Shen, H. and Tsiotras, P. (2003). 'Optimal Two-Impulse Rendezvous Using Multiple-Revolution Lambert Solutions'. In: *Journal of Guidance, Control and Dynamics* 26.1, pp. 50–61. DOI: `10.2514/2.5014`.

Siminski, J., Fiedler, H. and Schildknecht, T. (2013a). 'Track association performance of the best hypothesis search method'. In: *6th European Conference on Space Debris, Darmstadt, Germany.*

Siminski, J., Montenbruck, O., Fiedler, H. and Schildknecht, T. (2014). 'Short-arc tracklet association for geostationary objects'. In: *Advances in Space Research* 53.8, pp. 1184–1194. ISSN: 0273-1177. DOI: `https://doi.org/10.1016/j.asr.2014.01.017`.

Siminski, J., Montenbruck, O., Fiedler, H. and Weigel, M. (2013b). 'Best hypotheses search on iso-energy-grid for initial orbit determination and track association'. In: *AAS/AIAA Spaceflight Mechanics Meeting, Kauai, Hawaii, U.S.A.*

Singh, N., Horwood, J. T., Aristoff, J. M., Poore, A. B., Sheaff, C. and Jah, M. K. (2013). 'Multiple hypothesis tracking (MHT) for space surveillance: Results and simulation studies'. In: *Air Force Research Lab Kirtland AFB NM Space Vehicles Directorate.*

SPACE-TRACK (2019). *TLE data.* URL: `https://www.space-track.org/`.

Spoto, F., Vigna, A. D., Milani, A., Tommei, G., Tanga, P., Mignard, F. et al. (2018). 'Short arc orbit determination and imminent impactors in the Gaia era'. In: *Astronomy and Astrophysics* 614. DOI: `https://doi.org/10.1051/0004-6361/201732104`.

Stansbery, E. G. and Johnson, N. L. (2007). 'Space Surveillance network for a more complete catalog'. In: *US and Russian Space Surveillance Workshop Proceedings, California, U.S.A.*

Sun, F. T., Vinh, N. H. and Chern, T. (1987). 'Analytic study of the solution families of the extended Godal's time equation for Lambert problem'. In: *Journal of Astronautical Sciences* 35.2.

Thorne, J. (2014). 'Convergence Behavior of Series Solutions of the Lambert Problem'. In: *Journal of Guidance, Control, and Dynamics* 38.8 (Oct. 2014), pp. 1–6. DOI: `10.2514/1.G000701`.

Tommei, G., Milani, A. and Rossi, A. (2007). 'Orbit determination of space debris: admissible regions'. In: *Celestial Mechanics and Dynamical Astronomy* 97.4. DOI: `10.1007/s10569-007-9065-x`.

Torre Sangrà, D. de la and Fantino, E. (2015). 'Review of Lambert's problem'. In: *25th International Symposium on Space Flight Dynamics, Munich, Germany.*

Vallado, D. (2007). *Fundamentals of astrodynamics and applications.* Microcosm press, third edition. ISBN: 978-1881883227. DOI: `10.1017/S0001924000064757`.

Virtanen, J., Muinonen, K. and Bowell, E. (2001). 'Statistical Ranging of Asteroid Orbits'. In: *Icarus* 2.154. ISSN: 0019-1035. DOI: `https://doi.org/10.1006/icar.2001.6592`.

Zhang, G., Mortari, D. and Zhou, D. (2010). 'Constrained Multiple-Revolution Lambert's Problem'. In: *Journal of Guidance, Control and Dynamics* 33.6, pp. 1779–1786. DOI: `10.2514/1.49683`.

Zittersteijn, M. (2017). 'Space debris cataloging of GEO objects by using Meta-Heuristic methods'. PhD thesis. University of Bern.

Declaration of consent

on the basis of Article 18 of the PromR Phil.-nat. 19

Name/First Name: Mann, Harleen Kaur

Registration Number: 16-109-308

Study program: Doctorate: Physics with a focus on Astronomy

Bachelor ☐   Master ☐   Dissertation ✔

Title of the thesis: Initial Orbit Determination with Angles-Only Observations of Space Debris

Supervisor: Prof. Dr. Thomas Schildknecht

I declare herewith that this thesis is my own work and that I have not used any sources other than those stated. I have indicated the adoption of quotations as well as thoughts taken from other authors as such in the thesis. I am aware that the Senate pursuant to Article 36 paragraph 1 litera r of the University Act of September 5th, 1996 and Article 69 of the University Statute of June 7th, 2011 is authorized to revoke the doctoral degree awarded on the basis of this thesis.

For the purposes of evaluation and verification of compliance with the declaration of originality and the regulations governing plagiarism, I hereby grant the University of Bern the right to process my personal data and to perform the acts of use this requires, in particular, to reproduce the written thesis and to store it permanently in a database, and to use said database, or to make said database available, to enable comparison with theses submitted by others.

Darmstadt, 16 April 2025

Place/Date

Harleen Kaur Mann

Signature

Digitally signed by Harleen Kaur Mann
Date: 2025.04.16 12:11:09 +02'00'